UNIVERSIDADE FEDERAL DO PARANÁ

FREDERICO ALVES JAHNERT

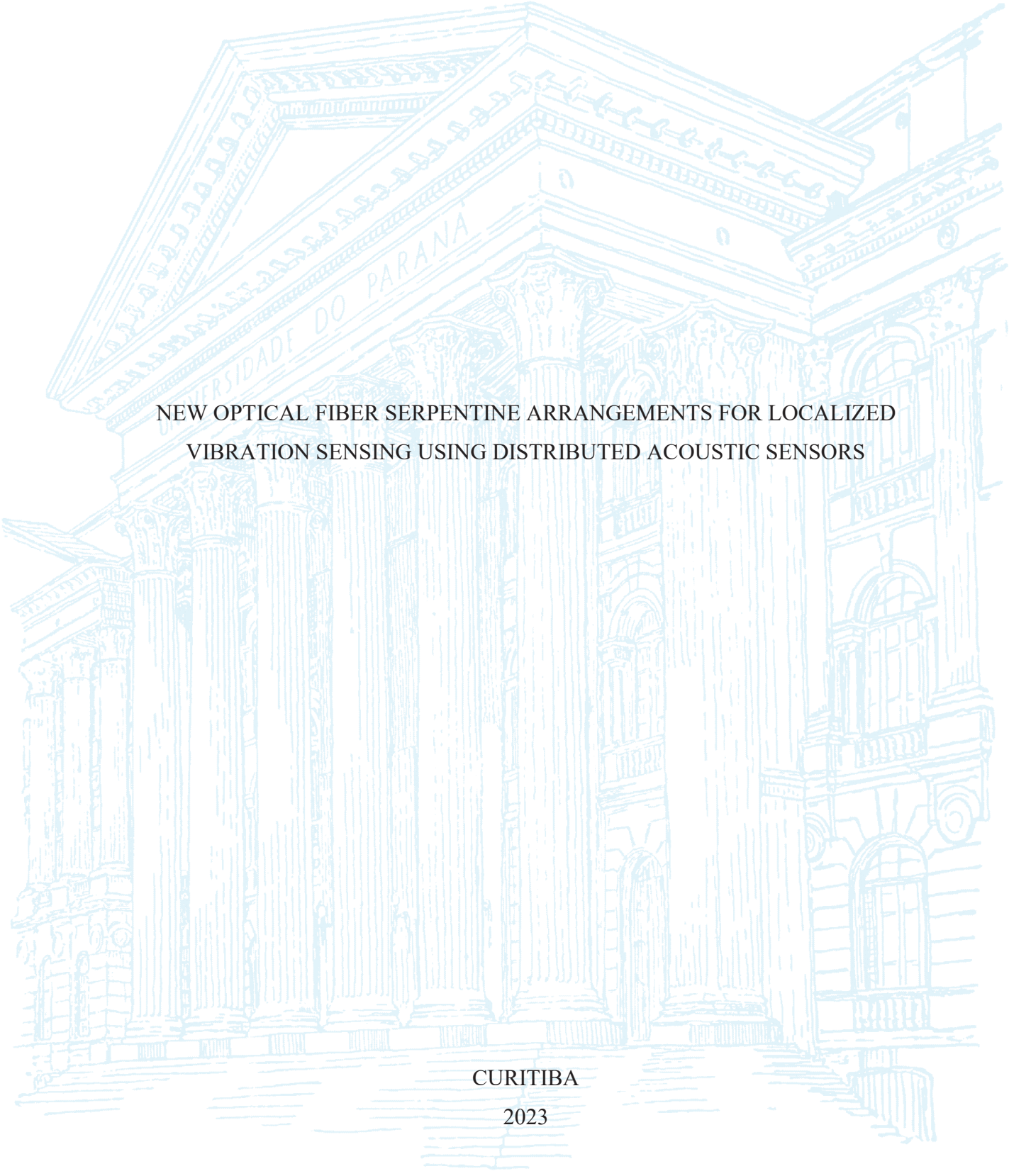

NEW OPTICAL FIBER SERPENTINE ARRANGEMENTS FOR LOCALIZED VIBRATION SENSING USING DISTRIBUTED ACOUSTIC SENSORS

CURITIBA

2023

FREDERICO ALVES JAHNERT

NOVO ARRANJO DE FIBRAS ÓPTICAS PARA SENSORIAMENTO DE VIBRAÇÕES LOCALIZADAS UTILIZANDO SENSORES ACÚSTICOS DISTRIBUIDOS

NEW OPTICAL FIBER SERPENTINE ARRANGEMENTS FOR LOCALIZED VIBRATION SENSING USING DISTRIBUTED ACOUSTIC SENSORS

Tese apresentada ao curso de Pós-Graduação em Engenharia Mecânica, linha de pesquisa de Mecânica dos Sólidos e Vibrações, Setor de Tecnologia, da Universidade Federal do Paraná, como requisito parcial à obtenção do grau de Doutor em Engenharia Mecânica.

Orientador: Prof. Dr. Carlos Alberto Bavastri.
Co-orientador: Prof. Dr. Jucélio Tomás Pereira.

Thesis submitted to the Post-Graduate Program in Mechanical Engineering of the Federal University of Paraná, Area of Research in Solid Mechanics and Vibrations, as partial fulfillment of the requirements for the degree Doctor of Philosophy in Mechanical Engineering.

Supervisor: Prof. Dr. Carlos Alberto Bavastri.
Co-supervisor: Prof. Dr. Jucélio Tomás Pereira.

CURITIBA

2023

DADOS INTERNACIONAIS DE CATALOGAÇÃO NA PUBLICAÇÃO (CIP)
UNIVERSIDADE FEDERAL DO PARANÁ
SISTEMA DE BIBLIOTECAS – BIBLIOTECA DE CIÊNCIA E TECNOLOGIA

Jahnert, Frederico Alves
New optical fiber serpentine arrangements for localized vibration sensing using distributed acoustic sensors / Frederico Alves Jahnert. – Curitiba, 2023.
1 recurso on-line : PDF.

Tese (Doutorado) - Universidade Federal do Paraná, Setor de Tecnologia, Programa de Pós-Graduação em Engenharia Mecânica.

Orientador: Carlos Alberto Bavastri
Coorientador: Jucélio Tomás Pereira

1. Fibras ópticas. 2. Poços – Monitoramento. 3. Vibração – Medição. 4. Dispositivos óptico-acústicos. 5. Análise modal. 6. Método dos Elementos Finitos. I. Universidade Federal do Paraná. II. Programa de Pós-Graduação em Engenharia Mecânica. III. Bavastri, Carlos Alberto. IV. Pereira, Jucélio Tomás. V. Título.

Bibliotecário: Elias Barbosa da Silva CRB-9/1894

MINISTÉRIO DA EDUCAÇÃO
SETOR DE TECNOLOGIA
UNIVERSIDADE FEDERAL DO PARANÁ
PRÓ-REITORIA DE PESQUISA E PÓS-GRADUAÇÃO
PROGRAMA DE PÓS-GRADUAÇÃO ENGENHARIA MECÂNICA - 40001016040P5

TERMO DE APROVAÇÃO

Os membros da Banca Examinadora designada pelo Colegiado do Programa de Pós-Graduação ENGENHARIA MECÂNICA da Universidade Federal do Paraná foram convocados para realizar a arguição da tese de Doutorado de **FREDERICO ALVES JAHNERT** intitulada: **NEW OPTICAL FIBER SERPENTINE ARRANGEMENTS FOR LOCALIZED VIBRATION SENSING USING DISTRIBUTED ACOUSTIC SENSORS**, sob orientação do Prof. Dr. CARLOS ALBERTO BAVASTRI, que após terem inquirido o aluno e realizada a avaliação do trabalho, são de parecer pela sua APROVAÇÃO no rito de defesa.
A outorga do título de doutor está sujeita à homologação pelo colegiado, ao atendimento de todas as indicações e correções solicitadas pela banca e ao pleno atendimento das demandas regimentais do Programa de Pós-Graduação.

CURITIBA, 16 de Junho de 2023.

Assinatura Eletrônica
19/06/2023 11:41:04.0
CARLOS ALBERTO BAVASTRI
Presidente da Banca Examinadora

Assinatura Eletrônica
19/06/2023 05:36:45.0
FLAVIO AUGUSTO PRESEZNIAK
Avaliador Externo (SEM VÍNCULO)

Assinatura Eletrônica
18/06/2023 19:18:04.0
JEAN CARLOS CARDOZO DA SILVA
Avaliador Externo (UNIVERSIDADE TECNOLÓGICA FEDERAL DO PARANÁ)

Assinatura Eletrônica
20/06/2023 11:16:25.0
DANIEL RODRIGUES PIPA
Avaliador Externo (UNIVERSIDADE TECNOLÓGICA FEDERAL DO PARANÁ)

Assinatura Eletrônica
19/06/2023 16:18:03.0
JUCÉLIO TOMÁS PEREIRA
Coorientador(a) (UNIVERSIDADE FEDERAL DO PARANÁ)

ACKNOWLEDGEMENTS

I would like to express my sincere gratitude to my caring supervisors Prof. Dr. Carlos Alberto Bavastri for his guidance, patience and encouragements and my co-supervisor Prof. Dr. Jucélio Tomás Pereira for his advices and brilliant ideas that helped forge this thesis. Their trust in my work greatly motivated me to succeed and, as friends, their guidance helped me in my career and life. In addition, I would like to thank Prof. Dr. Jean Carlos Cardozo da Silva, Prof. Dr. Daniel Rodrigues Pipa, Prof. Dr. Marco Jose da Silva, Prof. Dr. Cicero Martelli, Prof. Dr. Uilian Dreyer and all the academic body at the *Laboratório de Tecnologia em Sistemas Sensores* (LTSS) that provided me with a healthy environment to learn and supplied opportunities to develop my knowledge in the field of Photonics, Electronics and Sensor Systems. Being a member of the research project for Petrobras at LTSS, within UTFPR, provided me with a constant feeling of belonging. I want to express my sincere gratitude to my colleagues Danilo, Weber, Talita, Beatriz, Wanderson, Marcão, and others, whose presence brought both lightheartedness during funny moments and strength during arduous times when we had to develop resilience and overcome difficult challenges. Their unwavering support throughout the challenging period of the Covid-19 pandemic while working on the project will always be remembered.

I would like to thank: my parents Ricardo and Rosimeri, and my family for their unconditional support; my partner, Mariana Lampe, who assisted me through this thesis, even helping with experiments in the weekends and at late nights at the laboratory; and my Australian friend Hamish McKenzie.

Finally, I am grateful for the time and effort invested in reviewing my work by the thesis committee: Professors Dr. Jean Carlos Cardozo da Silva, Dr. Daniel Rodrigues Pipa and Dr. Flavio Augusto Presezniak.

This study was financed in part by the *Conselho Nacional de Desenvolvimento Cientifico e Tecnológico* (CNPq), *Coordenação de Aperfeiçoamento de Pessoal de Nível Superior* (CAPES) and Petrobras R&D project under grant 5850.0107231.18.9

RESUMO

Atualmente, Sensores Acústicos Distribuídos (DAS) utilizando fibras ópticas baseados no método de Reflectometria Óptica no Domínio do Tempo (OTDR) reconstruída por fase são considerados como alternativas promissoras para monitoramento de ativos. Esses sensores possuem a capacidade de monitorar continuamente e em tempo real ondas acústicas, vibração mecânica e temperatura do ambiente externo por dezenas de quilômetros ao longo do comprimento da fibra óptica. O sensor tem despertado grande interesse científico, pois pode ser aplicado em ambientes hostis, onde são necessárias imunidade eletromagnética e/ou medições ao longo de grandes comprimentos. As aplicações industriais incluem monitoramento ferroviário, levantamento sísmico e monitoramento de poços de petróleo como alternativas a sensores clássicos ou introduzidos como novos métodos de medição. O DAS utiliza atributos da luz retroespalhada para inferir as quantidades físicas a serem medidas. Um pulso óptico é lançado no guia de onda, caracterizado pelo núcleo da fibra óptica, e excitações externas causam mudanças no índice de refração em regiões discretas ao longo da fibra. Técnicas de processamento de sinal convertem a deformação longitudinal e a mudança de temperatura em mudanças de fase medidas no interrogador. Uma desvantagem do DAS é que a menor resolução de detecção é de cerca de 1 metro de comprimento de fibra. Embora muitos estudos no campo do DAS abordem métodos para melhorar o desempenho de sensoriamento, a maioria não leva em consideração a interação entre ondas de pressão e ondas mecânicas nas estruturas medidas pelo sistema. O corrente trabalho tem como objetivo o estudo da aplicação do sensor baseado em fibras óticas para análise de vibrações estruturais com medições localizadas para aplicação em pequenas estruturas e dispositivos, incluindo métodos de aplicação do sensor que promovem o aumento da sensibilidade, e melhorias da qualidade da resposta à vibração medida e da resolução espacial. Um novo método de medição da deformação dinâmica local de estruturas usando DAS é proposto e analisado. O método utiliza configurações da fibra ótica em forma de serpentina para medir o espectro de frequência dos sinais de deformação em fase em regiões limitadas da estrutura, permitindo que o DAS determine, entre outros parâmetros de vibração, a função resposta em frequência de deformação (FRFD). Estudos experimentais da aplicação do sensor com diferentes arranjos em pequenas estruturas são realizados. Um modelo que converte o sinal de fase óptica medido em deformação é desenvolvido utilizando os coeficientes elasto-ópticos de Pockel. A resposta do arranjo de fibras óticas em serpentina é calculada utilizando o Método de Elementos Finitos (MEF). Resultados experimentais apresentam boa concordância com resultados numéricos utilizando MEF e usando sensores de referência, demonstrando uma melhoria significativa na precisão do FRFD do DAS usando a configuração em serpentina e um aumento de até 12,9 dB na relação Pico-Ruído (PNR) para baixas forças de excitação no caso de vibração em vigas. A resposta recuperada permitiu a reconstrução dos modos de vibração. Além disso, neste trabalho uma câmara anecóica foi desenvolvida para experimentos acústicos e um estudo de vibrações medidas por fibras óticas em serpentina em uma placa de aço sendo excitada por fontes acústicas foi realizado. Os resultados demonstram que o arranjo em serpentina permite a medição da FRFD com um nível de pressão acústica de 54dB. O estudo apresentado pode ser aplicado para avanços no campo de monitoramento estrutural, identificação de sinais acústicos, e demonstra que o sensor pode ser aplicado em estruturas em escalas inferiores em comparação com as escalas utilizadas atualmente.

Palavras-chave: Sensor Acústico Distribuído, Sensores de Fibra Ótica Distribuído, Monitoramento de Poço, Análise modal, Método dos Elementos Finitos, Multifísica.

ABSTRACT

Distributed Acoustic Sensors (DAS) using optical fibers based on phase sensitive Optical Time Domain Reflectometry are seen as one of the most promising alternatives for monitoring assets today, with the ability to continuously monitor in real-time acoustic waves, mechanical vibration and temperature of the external environment for many kilometers along the length of the optical fiber. The sensor has attracted widespread scientific interest as it can be applied where electromagnetic immunity or spatially continuous measurements are required. Industrial applications include rail monitoring, seismic surveying and well monitoring as alternatives to classic sensors and as potential sensors for completely new applications. DAS uses attributes of the backscattered light to infer the physical quantities to be measured. An optical pulse is launched into the optical fiber waveguide and external excitation causes changes in the refractive index at discrete regions of the optical fiber. Signal processing techniques convert longitudinal strain and temperature change into phase changes measured in the interrogator. A drawback of DAS is that the lowest sensing resolution is around 1 to 3 meters long. Although many studies in the field of DAS are concerned with improving acoustic performance, most do not take into consideration the interaction between pressure waves and mechanical waves in the structures being measured. The scope of this thesis comprises of analyzing methods of application of the sensor that grant improved sensibility, enhanced vibration response and improved spatial resolution for distributed sensing of mechanical vibrations and acoustic excitation. A novel method of measuring local dynamic strain of structures using DAS is analyzed. The method uses serpentine configurations to measure the frequency spectrum of the in-phase strain signals at discrete regions of the structure, enabling DAS to determine, among other vibration parameters, the strain frequency response function (SFRF). Experimental studies of the sensor application with different arrangements in small structures are performed. A method of converting the measured optical phase signal into strain using the Pockel elasto-optic coefficients is developed considering the arrangement and implemented Finite Element Analysis. Experimental results show agreement with numerical results developed by the Finite Element Method (FEM) and using reference sensors, demonstrating a significant improvement of the DAS SFRF accuracy using the serpentine configuration and up to 12.9 dB increase in Peak-to-Noise Ratio (PNR) for low excitation forces in the case of beam vibration. The recovered response enabled the reconstruction of mode shapes. In addition, this work presents the development of an anechoic chamber for acoustic experiments using optical fiber sensors and a study in the characterization of structures using optical fibers with acoustic sources. The results demonstrate that the serpentine optical fiber system arrangement is able to measure the SFRF with a 54 dB sound source sweep for flexural modes. The methodology presented here can be the basis for advances in the field of structural health monitoring, signal identification and acoustics by demonstrating that the sensor system can be applied to small and large structures alike.

Keywords: Distributed Acoustic Sensors, Distributed Optical fiber sensors, Well monitoring, Modal Analysis, Finite Element Method, Multiphysics.

LIST OF FIGURES

FIGURE 1 – FLOW CHART OF OPTICAL FIBER SENSORS'S CONCEPT. 26
FIGURE 2 – OPTICAL CONCEPT OF FBG MEASUREMENT. 27
FIGURE 3 – VIRTUAL STATES AND ELECTRONIC STATES FOR RAYLEIGH AND RAMAN VIBRATION SCATTERING 29
FIGURE 4 – LIGHT SCATTERING FREQUENCIES SPECTRUM 30
FIGURE 5 – PHASE SENSITIVE DAS OPTICAL SIGNAL 32
FIGURE 6 – DEVELOPMENT OF DAS 33
FIGURE 7 – SIGNAL REPRESENTATION OF A COILED OPTICAL FIBER DIVIDED INTO STRAINED AND UNSTRAINED REGIONS 35
FIGURE 8 – UNWRAPPING ALGORITHM REPRESENTATION USED FOR PHASE RECONSTRUCTION 36
FIGURE 9 – GAUGE LENGTH EFFECTS IN (a) SNR FOR A GIVEN SPATIAL WAVELENGHT EXCITATION AND (b) RESULTING WAVELENGTH 37
FIGURE 10 – DISTRIBUTED OPTICAL FIBER SENSOR IN WING SPAR 39
FIGURE 11 – DISTRIBUTED OPTICAL FIBER SENSOS INSTALLATION IN STIFFINED PLATE 39
FIGURE 12 – ACOUSTIC EXPERIMENT USING DAS OPTICAL FIBER AND SPEAKER 40
FIGURE 13 – PSD OF MUSIC SIGNAL MEASURED BY DAS SYSTEM WITH AND WITHOUT SIGNAL PROCESSING 40
FIGURE 14 – FEM MODEL OF ACUSTO-OPTICAL DEVICE 41
FIGURE 15 – FEM MODAL ANALYSIS OF ACUSTO-OPTICAL MODULATOR 41
FIGURE 16 – MAIN ELEMENTS OF SMART WELLS INSTALLATION. 42
FIGURE 17 – MODELS OF CABLES USED IN WELLS. 43
FIGURE 18 – CABLE SUPPORT COMPONENTS IN PRODUCTION WELLS. 43
FIGURE 19 – INSTALLATION OF OPTICAL FIBER MONITORING SYSTEM IN ON LAND WELL. 44
FIGURE 20 – A) CABLE USED TO SECURE OPTIC FIBER IN DAS SENSING; B) ILLUSTRATION OF THE CABLE'S CROSS-SECTION; C) CABLE INSTALLATION IN A LAND WELL. 45
FIGURE 21 – SIZING AND COMPOSITION OF PRIMARY COATED OPTICAL FIBER (PCOF). 46

FIGURE 22 – FIMT PATENT FOR ENHANCED ACOUSTIC COUPLING FOR DAS (EP 2 418 466 A2). 47
FIGURE 23 –PATENT FOR INCREASED ACOUSTIC COUPLING USING WATER ACOUSTIC IMPENDANCE (EP 2 418 466 A2). 47
FIGURE 24 – DAS CABLE PATENT WITH MEMBRANE FOR ACOUSTIC AMPLIFICATION 48
FIGURE 25 – DAS CABLE PATENT WITH INERTIA MEMBER FOR ACOUSTIC AMPLIFICATION 48
FIGURE 26 – COMPARISON CHART OF THE AMPLITUDE CAPTURED BY DIFFERENT CABLES. 49
FIGURE 27 – RESPONSE OF HELEICOIDAL WOUNDED OPTICAL FIBER FOR SEISMIC SIGNALS 50
FIGURE 28 – PROTOTYPE OF CABLE WITH 7 FILAMENTS OF COATED OPTICAL FIBERS 50
FIGURE 29 – ARRANGEMENT OF HELICAL FIBER FOR 2,44 CENTIMETER TUBE AND HELICAL ANGLE OF 20º. 50
FIGURE 30 – COMPARISON BETWEEN MICROPHONE TRANSFER FUNCTION AND DAS TRANSFER FUNCTION. 52
FIGURE 31 – FREE BODY DIAGRAM OF STRING MODE DYNAMIC MOTION 58
FIGURE 32 – FREE BODY DIAGRAM OF BAR MODE DYNAMIC MOTION. 59
FIGURE 33 – FREE BODY DIAGRAM OF BEAM MODE DYNAMIC MOTION 60
FIGURE 34 – DISPLACEMENT, VELOCITY AND ACCELERATION SENSIBILITY FOR CONSTANT VIBRATION ENERGY 61
FIGURE 35 – SOUND TRANMISSION AND REFLECTION 64
FIGURE 36 – ACOUSTIC COUPLING OF INCIDENT ACOUSTIC WAVE. 66
FIGURE 37 – TRACE SPEED OF INCIDENT ACOUSTIC WAVE. A) ACUTE INCIDENT ANGLE, B) 45 DEGREES AND C) OBTUSE INCIDENT ANGLE. 66
FIGURE 38 – COMPARISON CHART OF SENSING SENSITIVITY BY OPTICAL FIBER BASED ON WAVE ANGLE. 70
FIGURE 39 – ARBITRARY DEFORMATION WITHIN THE OPTICAL FIBER SENSING RESOLUTION 72
FIGURE 40 – SERPENTINE ARRANGEMENT 74
FIGURE 41 – MODEL UPDATING ALGORITHM 75

FIGURE 42 – PROCESS FLOWCHART OF PHOTO-ELASTIC SIMULATION USING FEM. 76
FIGURE 43 – OPTICAL FIBER SERPENTINE ARRANGEMENT FOR BEAM VIBRATION EXPERIMENT. 78
FIGURE 44 – ALUMINIUM BEAM VIBRATION EXPERIMENT SETUP 80
FIGURE 45 – DIAGRAM OF COMPLETE OPTICAL FIBER ARRENGEMENT IN ALUMINIUM BEAM EXPERIMENT 80
FIGURE 46 – SIMULTANEOUS MEASUREMENTS OF VIBRATION EXPERIMENTS 81
FIGURE 47 – FINITE ELEMENT MESH OF ALUMINIUM BEAM STRUCTURE 81
FIGURE 48 – A) DAS PHASE-DIFFERENTIAL SIGNAL IN THE TIME DOMAIN ACQUIRED DURING MODAL TESTING FOR A SINGLE ARRANGEMENT AND B) THE FREQUENCY RESPONSE SPECTRUM OF THE SIGNAL. 82
FIGURE 49 – TRANSPORTABLE ANECHOIC CHAMBER DESIGN. 84
FIGURE 50 – ANECHOIC CHAMBER DESIGN 85
FIGURE 51 – ANECHOIC CHAMBER'S FINAL CONSTRUCTION. 85
FIGURE 52 – TRANSMISSIBILITY DAMPED SPRING-MASS SYSTEM 86
FIGURE 53 – TRANSMISSIBILITY OF ANECHOIC CHAMBER AND FLOOR. 86
FIGURE 54 – VALIDATION OF ANECHOIC CHAMBER. 88
FIGURE 55 – SOUND SOURCE STABILITY USING REFERENCE MICROPHONE. 89
FIGURE 56 – SPL MEASURED IN ANECHOIC CHAMBER EXPERIMENTAL VALIDATION 89
FIGURE 57 – SPL DEVIATION FROM THE ISL ANALYTICAL CURVE IN ANECHOIC CHAMBER EXPERIMENTAL RESULTS 90
FIGURE 58 – SPL DEVIATION FROM THE ISL ANALYTICAL CURVE IN ANECHOIC CHAMBER EXPERIMENTAL RESULTS 90
FIGURE 59 – ACOUSTIC EXPERIMENT CONFIGURATION IDENTIFICATION OF VIBRATION IN PLATE USING DAS: A) ARRANGEMENT OF OPTICAL FIBERS AND B) DIAGRAM OF EXPERIMENT 92
FIGURE 60 – ACOUSTIC EXPERIMENT FOR ACOUSTICALLY INDUCED PLATE VIBRATION 92
FIGURE 61 – ACOUSTIC EQUIPMENT FOR EXPERIMENT: A) ACOUSTIC SOURCE; B) FUNCTION GENERATOR AND SIGNAL ANALYZER; C) MICROPHONE 1; D) MICROPHONE 2 93

FIGURE 62 – MESH OF PLATE MODEL 93
FIGURE 63 – NUMERICAL FLEXURAL MODES OF VIBRATION OF ALUMINIUM BEAM STRUCTURE 94
FIGURE 64 – FEM MODEL CALIBRATION USING INERTANCE MEASURED BY ACCELEROMETERS FOR BEAM EXPERIMENT 95
FIGURE 65 –TIME DOMAIN SIGNAL OF THE THREE ARRANGEMENTS USED OT INSTRUMENT THE BEAM MODAL EXPERIMENT: SINGLE PASS, 3 PASSES AND 9 PASSES SERPENTINES 96
FIGURE 66 – A) TIME DOMAIN SIGNAL OF DAS SYSTEM; B) STFFT OF SIGNAL IN THE FREQUENCY DOMAIN 97
FIGURE 67 – PSD OF DAS SIGNALS ACQUIRED AT POINTS ALONG EACH SECTION OF THE BEAM 98
FIGURE 68 – AVERAGE PSD RESPONSE OF THE OPTICAL FIBER AT EACH SECTION OF THE BEAM 99
FIGURE 69 – NORMALIZED STRAIN MODE SHAPES OF THE BEAM MEASURED BY DAS IN THE 9 PASSES SERPENTINE ARRANGEMENT AND NUMERICALLY 100
FIGURE 70 – RESPONSE OF THE OPTICAL FIBER AT EACH SECTION OF THE BEAM 101
FIGURE 71 – PEAK SIGNAL VALUE ON THE FIFTH MODE RESONANT FREQUENCY AT MAXIMUM STRAIN POSITION FOR IMPACT HAMMER TESTS 101
FIGURE 72 – COMPARISON BETWEEN THE AVERAGE PSD RESPONSE OBTAINED USING THE 9-PASSES SERPENTINE SECTIONS AND THE STRAIGHT-LINE FIBER 102
FIGURE 73 – COMPARISON BETWEEN CALIBRATED SFRF OBTAINED OPTICAL FIBER ARRANGEMENTS WITH DAS AND FEA SIMULATION 104
FIGURE 74 – PARAMETRIC SRFR CURVE BASED ON DAS RESULTS COMPARED TO NUMERICAL SFRF 105
FIGURE 75 – MODES OF VIBRATION OF STAINLESS STEEL PLATE 106
FIGURE 76 – SPEAKER FREQUENCY SPECTRUM SOUND POWER LEVEL NEAR PLATE FOR CHIRP EXPERIMENT 107
FIGURE 77 – DAS SIGNAL FOR ACOUSTIC EXPERIMENTS WITH FREE-FREE PLATE 108

FIGURE 78 – DAS STRAIN SIGNALS FOR EACH SERPENTINE ARRANGEMENT AT DIFFERENT POINTS IN TIME 108
FIGURE 79 – 0.5 VPP ACOUSTIC SIGNAL RESPONSE FOR EACH SECTION OF THE PLATE EXPERIMENT 109
FIGURE 80 – 1 VPP ACOUSTIC SIGNAL RESPONSE FOR EACH SECTION OF THE PLATE EXPERIMENT 110
FIGURE 81 – 2 VPP ACOUSTIC SIGNAL RESPONSE FOR EACH SECTION OF THE PLATE EXPERIMENT 110
FIGURE 83 – MODE DECOMPOSITION OF FREQUENCY RESPONSE OBTAINED USING DAS FOR PLATE EXPERIMENT 112
FIGURE 84 – HYDROSTATIC AND TRANSVER PRESSURE IN OPTICAL FIBER..... 122
FIGURE 85 – A) BENT AND STRETCHED FIBER; B) FIBER'S STRAIN DISTRIBUTION. 123

LIST OF TABLES

TABLE 1 – DEVELOPMENTS AND SPATIAL RESOLUTIONS 34
TABLE 2 – MECHANICAL PROPERTIES OF GENERIC OPTICAL FIBERS. 46
TABLE 3 – VIBRATION FEATURES BASED ON STRUCTURE TYPE FOR FREE-FREE BOUNDARY CONDITIONS 60
TABLE 4 – ACOUSTIC PERFORMANCE OF ABSORPTION WEDGES AND NOISE REDUCTION COEFFICIENT (NRC) 85
TABLE 5 – MAXIMUM ALLOWABLE DEVIATIONS OF MEASURED SOUND PRESSURE LEVEL (SPL) FROM ANALYTICAL VALUES USING THE INVERSE SQUARE LAW. 87
TABLE 6 – IDENTIFICATION OF FLEXURAL NATURAL FREQUENCIES 103

LIST OF ABREVIATIONS

AOM	Acusto-Optical Modulator
APDL	Ansys Parametric Design Language
AT-BOTDA	Amplitude Transfer-Brillouin Optical Time Domain Analysis
BFS	Brillouin Frequency Shift
BLI	Bending Loss Insensitive
BOTDA	Brillouin Optical Time Domain Analysis
BOTDR	Brillouin Time Domain Reflectometry
CAD	Computer Aided Design
C-OTDR	Amplitude based OTDR
DAQ	Data acquisition board
DAS	Distributed Acoustic Sensors
DFOS	Distributed Fiber Optical Sensors
DIN	Deutsches Institut für Normung
DTS	Distributed Temperature Sensors
DVS	Distributed vibration sensor
FBG	Fiber Bragg Grating sensor
FE	Finite Element
FEM	Finite Element Method
FIMT	Fiber in Metal Tube
FRF	Frequency Response Function
FUT	Fiber Under Test
GVIBS	*Grupo de Pesquisa de Vibrações e Som em Sistemas Mecânicos*
HPU	Hydraulic Power Unit
I	In-phase
ICV	Inflow Control Valves
IEEE	Institute of Electrical and Electronics Engineers
IoT	Internet of Things
IQ	In-phase and Quadrature
ISL	Inverse Square Law
ISO	Organization for Standization
LO	Local Oscillator

LTSS	*Laboratório de Tecnologia em Sistemas Sensores*
NRC	Noise Reduction Coefficients
OFDR	Optical Frequency Domain Reflectometry
OTDR	Optical Time Domain Reflectometry
PCOF	Primary Coated Optical Fiber
PNR	Peak to Noise Ratio
PSD	Power Spectrum Density
Q	Quadrature
R&D	Research and Development
SBS	Stimulated Brillouin Scattering
SFRF	Strain Frequency Response Function
SHM	Structure Health Monitoring
SMF	Single Mode Fiber
SNR	Signal to Noise Ratio
SPL	Sound Pressure Level
SRS	Stimulated Raman Scattering
STFFT	Short Time Fast Fourier Transform
ToA	Time of Arrival
UFPR	Federal University of Paraná
UTFPR	Federal Technological University of Paraná
UV	Ultra-violet
VSP	Vertical Seismic Profiling
ϕ-OTDR	Phase sensitive Optical Time Domain Reflectometry

LIST OF SYMBOLS

A_i	Arbitrary constants.
b	Adjustment parameter.
B	Bulk modulus.
B_{ij}	Polarization constants.
d	Principal experiment dimension.
c	Modal damping.
$c_{1,2}$	Speed of sound.
c_0	Reference speed of sound.
c_t	Trace wave speed.
C	Arbitrary constant.
$[C]$	Viscous damping matrix.
d	Diameter of the fiber.
E	Young's modulus of the material.
E_S	Error related to spread of backscattered signal.
E_w	Error related to unwrapping algorithm.
E_p	Error related to the position of the signal.
E_r	Light intensity related to the backscattered light.
E_{LO}	Light intensity related to the local oscillator.
E_{FRF}	Frequency Response Function error.
fs	Repetition rate of acquisition.
f_{cutoff}	Cutoff frequency.
$F(t)$	Force function.
G_L	Gauge length.
$H(\omega)$	Frequency Response Function.
$[H_\varepsilon]$	Strain Frequency Response Function matrix.

$H_a(\omega)$	Acceleration Frequency Response Function (Inertance).
H^{FEA}	Numerical Frequency Response Function.
H^{Exp}	Frequency Response Function obtained via experiment.
$I(t)$	In-phase component.
k_e	Free-space wavenumber.
K_{ij}	Impermeability tensor or the reciprocal of the dielectric tensor.
$[K]$	Stiffness matrices.
k	Wave number, Modal stiffness.
L	Length.
$[M]$	Mass matrix.
$M(x,t)$	Bending moment.
m	Modal mass.
n	Refractive index.
n_0	Reference refractive index.
p_i	Incoming acoustic wave.
p_r	Reflected acoustic wave.
p_t	Transmitted acoustic wave.
p_{ijkl}	Elasto-optic coefficients.
$Q(t)$	Quadrature component.
R	Bending radius.
$\{U\}$	Modal shape eigenvector.
w	Coordinate.
x	Coordinate.
z	Coordinate.
q_i	Generalized modal coordinate.
$V(x,t)$	Shear load.
I	Second moment of area.

P	Optimization problem.
t	Time.
k	Wave number.
T	Pulse width in seconds.
L_r	Ratio of strained and unstrained fiber in the arrangement.
$L_{Strained}$	Length of strained fiber.
$L_{Unstrained}$	Length of unstrained fiber.
r_{xx}	Autocorrelation function.
S	Sensing length.
S_L	Length of the straight part of the optical fiber serpentine arrangement.
S_{DL}	Length of the longer curved part of the optical fiber serpentine arrangement.
S_{DS}	Length of the longer shorter part of the optical fiber serpentine arrangement.
S_{xx}	power spectral density.
T	Transmissibility.
l_w	Length of the anechoic wedges.
r_0	Reference distance.
r_i	Distance of the *i*-th measured point.
L_{pi}	Corrected Sound Power Level.
$u(t)$	Displacement.
$\dot{u}(t)$	Velocity.
$\ddot{u}(t)$	Acceleration.
V_{pp}	Peak-to-peak voltage.
X_{trace}	Fourier transform of trace signal.
Z	Acoustic Impedance.
θ	Angle.
θ_i	Incoming wave angle.
θ_r	Reflected wave angle.
ω_s	AOM shifted frequency.
$\varphi(t)$	Phase change from the refraction index variations.

φ	Phase related to a point along the optical fiber path.
$\bar{\varphi}$	Phase related to a point along the optical fiber path.
ω	Circular frequency.
ω_c	Critical frequency.
ρ	Material density.
ω_n	Natural frequency.
υ	Poisson ratio.
φ	Propagation phase.
λ	Wavelength, solution of eigenvalue problem.
ε_{kl}	Components of elastic strain.
γ	Effective photo-elastic coefficient.
$\Delta\phi$	Phase difference.
$\hat{\varepsilon}_0$	Relaxation strain.
$\hat{\varepsilon}_x$	Structure induced strain.
ε_{ave}	Average strain.
ξ	Photo-elastic scale factor.
ϕ_i	Vibration mode related.
ψ	Damping coefficient of the suspension mechanism.
$L_p(r_i)$	Sound Power Level at a distance r_i.
δ_{uncert}	Uncertainty value.

SUMMARY

1 INTRODUCTION 22
1.1 THESIS STRUCTURE 23
1.2 LIST OF PUBLICATIONS 25

2 LITERATURE REVIEW 26
2.1 DISTRIBUTED OPTICAL FIBER SENSORS 26
2.1.1 Distributed Optical Fiber Sensors based on Scattering: Photons and Phonons 28
2.2 COHERENT RAYLEIGH BACKSCATTERING FOR DISTRIBUTED ACOUSTIC SENSORS 31
2.2.1 Spatial Resolution and Sensing Length 34
2.2.2 Gauge length and Phase Unwrapping 35
2.2.3 Sensibility and Signal-to-Noise Ratio 36
2.3 DISTRIBUTED ACOUSTIC SENSOR FOR MECHANICAL VIBRATIONS 38
2.4 WELL MONITORING WITH DAS 42
2.5 DAS CABLE DESIGN IN MONITORING APPLICATIONS 46
2.6 THESIS OBJECTIVES 51
2.7 THESIS CONTRIBUTION 52

3 THEORETICAL BACKGROUND 54
3.1 PHOTO-ELASTIC EFFECT THEORY ON OPTICAL FIBERS 54
3.2 MECHANICAL VIBRATIONS OF CONTINUOUS SYSTEMS 58
3.3 FINITE ELEMENT MODEL FOR VIBRATION ANALYSIS 61
3.3.1 Strain frequency response function 62
3.4 SOUND INDUCED VIBRATION OF STRUCTURES 64
3.4.1 Properties of incident acoustic waves in the optical fiber and sensed structures 65

4 METHODS AND MATERIALS 68
4.1 PHOTO-ELASTIC MODEL 69
4.1.1 Sensor Design and Arrangement 73
4.1.2 Signal Processing and Phase Model 74
4.2 FREE-FREE BEAM VIBRATION EXPERIMENT WITH OPTICAL FIBER IN SERPENTINE ARRENGEMENT 77
4.2.1 Sensor Design and Arrangement 78
4.2.2 Experimental Modal Analysis Setup 79
4.2.3 Digital Processing of DAS 82
4.3 ANECHOIC CHAMBER FOR ACOUSTIC EXPERIMENTS WITH OPTICAL FIBERS 83
4.3.1 Validation of Anechoic Chamber 87
4.4 IDENTIFICATION OF ACOUSTIC-INDUCED VIBRATION IN PLATES USING DAS 91

5 RESULTS AND DISCUSSION 94
5.1 FREE-FREE BEAM VIBRATION EXPERIMENT WITH OPTICAL FIBER IN SERPENTINE ARRANGEMENT 94
5.1.1 Strain Frequency Response Function 103

5.2 ACOUSTIC INDUCED VIBRATION IN PLATE USING DAS 105

6 CONCLUSIONS 113
6.1 FUTURE WORKS 115

7 APPENDIX A – BENDING AND RADIAL PRESSURE EFFECTS ON OPTICAL FIBERS 122

1 INTRODUCTION

In recent years, the amount of data gathered and processed each day has increased vastly. Advances in computing power, processing techniques, and data applications such as big data, machine learning, Internet of Things (IoT), “smart” technology and others, have introduced new engineering solutions which rely on high amounts of information. Innovations in sensor technology are essential to increase the data acquisition capabilities, increase the quality of the data gathered and perform effectively in extreme environments. In this context, distributed optical fiber sensors are considered promising technologies (HARTOG, 2017). In particular, fiber optic sensors based on phase sensitive Optical Time Domain Reflectometry (ϕ-OTDR) provides continuous strain sensing up to several kilometers in real-time through optical fiber cables. Most commonly referred to as Distributed Acoustic Sensors (DAS), the sensor uses a highly coherent laser source to interrogate the optical fiber and the returning Rayleigh backscattered light is measured to obtain the strain at several sections along the optical fiber for several kilometers. Other advantages of DAS include high sensitivity, compactness, ability to integrate multiple sensors, ability to perform under extreme environment using conduits and immunity to electromagnetic interference.

Recent advances in DAS are motivated by the oil and gas industry due to the necessity of well monitoring and acquiring seismic data (HARTOG, 2017), . The term “smart wells” was introduced in 1990 and describes the continuous monitoring of well properties in real time through the use of well sensors. The high costs and complexity of employing underground well sensors require innovative solutions due to the extreme downhole environment of high pressure (6000-8000 psi), high temperatures over 150º C and depths of more than 6000 meters in the case of pre-salt ultra-deep water oil fields (COSTA FRAGA et al., 2014). The DAS technology has other industrial applications such as monitoring railroad systems, leak detection in pipelines, Structural Health Monitoring (SHM) of civil structures, intrusion detection and others (HE; LIU, 2021; JUAREZ et al., 2005; LIEHR; MÜNZENBERGER; KREBBER, 2019; MUGGLETON et al., 2020; WIESMEYR et al., 2020). More recently, DAS has been developed for applications in smart cities for monitoring traffic, as one example, with a growing field of applications (CORERA et al., 2023).

Most uses of DAS sensors are related to the monitoring of large structures as result of the spatial resolution limitations inherent to the technology. The spatial resolution indicates the minimum distinguishable spatial scale along the sensing fiber. In recent studies, the minimum

pulse time can be as low as a few nanoseconds, which relates to a pulse that occupies less than one meter of optical fiber (WANG et al., 2020a). The resulting strain measurement is given by the average cumulative phase change within the fiber section occupied by the pulse (LIU et al., 2018). Thus, recent studies in SHM with DAS, for example, comprise of identifying vibration, wave propagation velocity and the use of statistical methods to develop indirect vibration information of large structures (LIEHR; MÜNZENBERGER; KREBBER, 2019; REN et al., 2016; WESTBROOK et al., 2020). Conversely, other distributed optical fiber sensors, such as those based on Optical Frequency Domain Reflectometry (OFDR), with a considerably lower sensing length, are able to detect material irregularities or perform SHM of relatively small structures due to the spatial resolution of a few millimeters (CHENG et al., 2017; CIMINELLO, 2019; FANG; SU; ANSARI, 2021; PELLONE et al., 2020). Several new DAS topologies and methods have been studied to improve spatial resolution, in a trade-off between cost, complexity, sampling rates and sensing length (CHEN; LIU; HE, 2019; CHEN et al., 2019; FENG et al., 2018; LU et al., 2017; MARTINS et al., 2016; WANG et al., 2020b). Thus, DAS has become a consolidated technology for vibration sensing due to advances in optoelectronics, however, there are few studies aiming at the mechanical vibrational behavior of the optical fiber installation, especially in localized measurements in small scale structures, and the resulting optical signal. Thus, this study analyses new applications of optical fibers as vibration and acoustic sensors using the DAS system for localized measurements in small or large structures.

1.1 THESIS STRUCTURE

In the current Chapter, the relevance and outcomes of the study are introduced. The importance of distributed acoustic sensors in the monitoring of vibration and its relevance in the industry are briefly outlined and the main conclusions of the thesis are pointed out.

In Chapter 2, a literature review of the ideas presented in this thesis are discussed, taking into consideration recent developments. The physical concept behind distributed acoustic sensors is discussed and an overview of sensor applications are cited. The acoustic and mechanical behavior of the DAS optical fiber is also introduced and correlated to performance in monitoring applications. Finally, the objectives of the thesis are listed and the novel contributions of the thesis are described.

In Chapter 3, the mathematical principles and numerical formulations considered in the thesis are described. The photo-elastic effect of the dynamic behavior of optical fiber is introduced, relating mechanical strain to optical response. Further, modeling of the optical fiber

structure response to direct mechanical vibration and acoustic excitation are described. In this chapter, FEM theory of vibrations in structures is also studied as background to the methods introduced in this thesis.

Chapter 4 illustrates the methodology and materials used to develop the study proposed in this thesis. The equations developed in Chapter 3 are implemented as a discretized model to analyze the dynamic optical fiber response with FEM software Ansys© and a signal processing method to convert experimental DAS phase data into strain response is implemented in Matlab©. A methodology of acquiring the strain frequency response function of a beam structure using DAS and the proposed optical fiber arrangements is introduced and the corresponding experiments are described. The design, construction and validation of an anechoic chamber for acoustic experiments in view of the ISO 26101 standard describing the qualification of free-field environments is also shown.

In Chapter 5, the results and discussion of each experiment described in Chapter 4 are presented. The calibrated solution of the FEM numerical model for the experiments are compared to the experimental frequency spectrum response measured by reference sensors, *viz.* accelerometers and microphones. For the first experiment, the vibration signal response performance of four different optical fiber arrangements with 1, 3, 6 and 9 coils are compared. The elasto-optical phase change conversion algorithm converts the obtained backscattered signals measured by DAS and the corresponding strain Power Spectrum Density (PSD) are analyzed, comparing performance indicators for each configuration, such as the Peak-to-Noise Ratio (PNR), gain and the reconstructed SFRF. Furthermore, the experimental results for the experiment of the free-free plate instrumented with a high-coil count serpentine arrangement under acoustic excitation is demonstrated.

The 6th Chapter discusses the conclusions and final considerations of this thesis, including suggestions of future works.

1.2 LIST OF PUBLICATIONS

JAHNERT, F. A.; WEBER, G. H.; GOMES, D. F.; et al. Optical Fiber Serpentine Arrangements for Vibration Analysis Using Distributed Acoustic Sensing. **IEEE Sensors Journal.** v. 22, n. 23, p. 22691 – 22699, 2022.

JAHNERT, F. A.; GOMES, D. F.; BRUSAMARELLO, B.; et al. Identification of Vibration in Plates using Optical Fiber Distributed Acoustic Sensors and Acoustic Source. **Conference: 27th COBEM – International Congress of Mechanical Engineering**, Florianópolis, Santa Catarina, Brazil, 4th - 8th December 2023. (***Accepted)***

JAHNERT, F. A.; GOMES, D. F.; WEBER, G. H.; et al. Initial Study on Structural Damage Detection using an Optical Fiber Serpentine Arrangement with Phase Sensitive Distributed Acoustic Sensor. **Conference: 27th COBEM – International Congress of Mechanical Engineering**, Florianópolis, Santa Catarina, Brazil, 4th - 8th December 2023. (***Accepted)***

WEBER, G. H.; **JAHNERT, F. A.**; GOMES, D. F.; et al. Optical Fiber Gauge Length Optimization of DAS using Fiber Bragg Grating Strain Measurements. **Conference: Bragg Gratings, Photosensitivity and Poling in Glass Waveguides and Materials 2022**, Maastricht,Limburg Netherlands, 24–28 July 2022.

VENDRUSCOLO, R.; GOMES, D. F.; **JAHNERT, F. A.**; et al. Using Fiber Bragg Grating Sensors for Partial Discharge (PD) Detection on Power Cables. **Conference: Bragg Gratings, Photosensitivity and Poling in Glass Waveguides and Materials 2022**, Maastricht,Limburg Netherlands, 24–28 July 2022

2 LITERATURE REVIEW

In this Chapter, the literature review is presented with relevant studies pertaining to the current work. The necessary concepts involving distributed acoustic sensors are discussed.

2.1 DISTRIBUTED OPTICAL FIBER SENSORS

Sensors based on optical fibers use the change in the properties of light to measure a certain physical quantity. Generally, a laser source interrogates the optical fiber with a light pulse. The light wave travels through the optical fiber, also considered as the waveguide, it undergoes change by the physical system to be measured. Attributes of the returning light wave such as intensity, propagation time, polarization, phase, optical spectrum and coherence are sampled at the interrogator opto-electronic device and correlated to the physical quantities being monitored (HARTOG, 2017). Thus, optical fiber sensors offer the advantage of carrying sensed data for long distances through its optical path to be processed in a less hostile and more suitable environments. FIGURE 1 illustrates the concept behind fiber optical sensors. Other advantages include high sensitivity, compactness, ability to integrate multiple sensors, and immunity to electromagnetic interference (HERNÁNDEZ-SERRANO et al., 2013).

FIGURE 1 – FLOW CHART OF OPTICAL FIBER SENSORS'S CONCEPT.

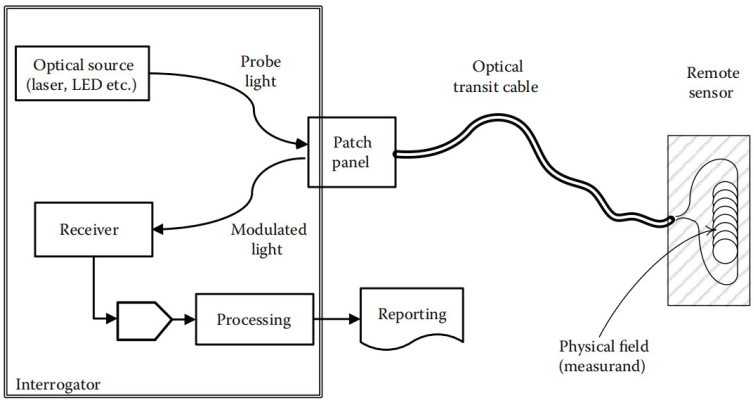

SOURCE: Hartog (2017).

There are several types of sensors based on optical fibers, each offering specific characteristics in the measuring process. Recently, optical fibers sensors have been developed such that the optical waveguide serves not only as mean to transit information, but as the sensor itself, called intrinsic optical fiber sensors. A commonly used intrinsic fiber optical sensor for

strain and temperature measurements is the fiber Bragg grating sensor (FBG). FBGs use longitudinal periodic variation in the refractive index in the optical core in specific positions of the optical fiber to filter certain wavelengths of light, thus reflecting the spectrum of light related to those wavelengths. FIGURE 2 demonstrates the optical concept of FBG measurements. Equispaced gratings are introduced in the optical fiber by exposing the core to a periodic pattern of intense laser light. The exposure introduces a change in refractive index at these positions of the fiber, which, in turn, reflects certain wavelengths of light that matches the distance between gratings. As a wide-band laser is pulsed through the optical fiber, the backscattered wavelength can change as strain excitation on the fiber causes the distances between gratings to increase or decrease.

FIGURE 2 – OPTICAL CONCEPT OF FBG MEASUREMENT.

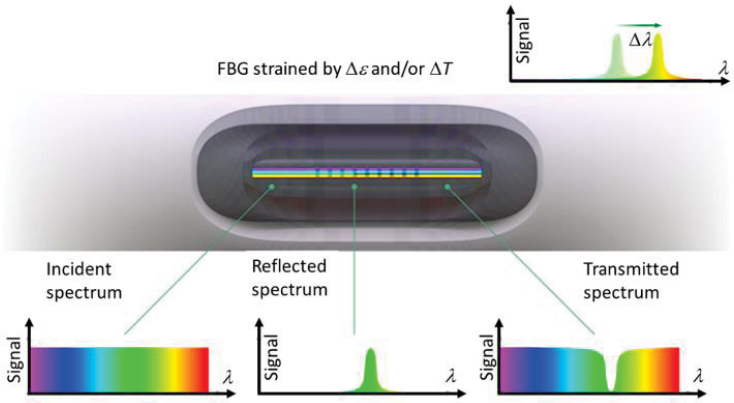

SOURCE: BAKAIC et al (2020).

FBGs have been used in many industries ranging from nuclear medicine to failure prediction in rotors and generators (BAKAIC et al., 2020). In 2020, the market size of FBG sensors corresponded to 1,332 billion USD with a projected growth to 4,913 billion USD in 2026 (MILLER; MENDEZ, 2011). This growth is explained by the solidification of this technology for the past 20 years (MILLER; MENDEZ, 2011). In the use of FBG sensors, multiple markings can be recorded in the optical fiber to measure the local strain or temperature at several points. However, the limitation in the number of markings and the complex marking inscription process hinders its commercial use (MILLER; MENDEZ, 2011).

In recent years, Distributed Fiber Optical Sensors (DFOS) have become an essential sensing technology with vast potential market applications (WANG et al., 2020a). In contrast to FBG and common electronic sensors such as accelerometers, geophones, temperature transducers and others, DFOS measures the external physical quantities at each region of the

whole length of the optical fiber. Hence, a DFOS system is capable of continuously measuring the temperature or strain distribution over extensive lengths of the optical fiber, similar to thousands of in-line sensors. Thus, in recent developments, these types of sensors are referred to as Distributed Temperature Sensors (DTS), Distributed vibration sensors (DVS) and Distributed Acoustic Sensors (DAS) (HARTOG, 2017).

2.1.1 Distributed Optical Fiber Sensors based on Scattering: Photons and Phonons

The propagation of light can be modelled in 4 different ways: using ray optics, wave optics, electromagnetic optics, and quantum optics (SALEH AND CARL, 2007). The behavior of light in certain circumstances is better described as a particle, emitted and absorbed discontinuously as discrete packets of energy, called photons (OKAMOTO, 2006). Photons differ from material particles as an individual photon cannot be located within a light beam, and have zero mass. Also, photons are not conserved, in other words, they are created and destroyed in encounters with material particles. Thus, the propagation of light through a medium is caused by a phenomenon called scattering of photons.

As light propagates through a medium, three forms of interaction occur between photons and matter: spontaneous or stimulated absorption and spontaneous emission of photons (HARTOG, 2017). The spontaneous absorption of the photon causes in the molecule an upward transition in energy level to a higher virtual state, while the spontaneous emission causes a downward transition decaying back to the lower state releasing a photon and conserving energy in the process, as shown in FIGURE 3. Stimulated absorption occurs when the molecule absorbs the energy of an incoming photon and resides in a higher state (SMITH, 2007). A new incoming photon can excite the high energy atom and drop the energy state back to ground level, while emitting a new photon. The frequency at which the spontaneous absorption and emission of photons occurs mostly match the frequency of light injected in the waveguide, called elastic scattering without a permanent exchange of energy between light and matter (VILLAR; MATIAS, 2020).

FIGURE 3 – VIRTUAL STATES AND ELECTRONIC STATES FOR RAYLEIGH AND RAMAN VIBRATION SCATTERING

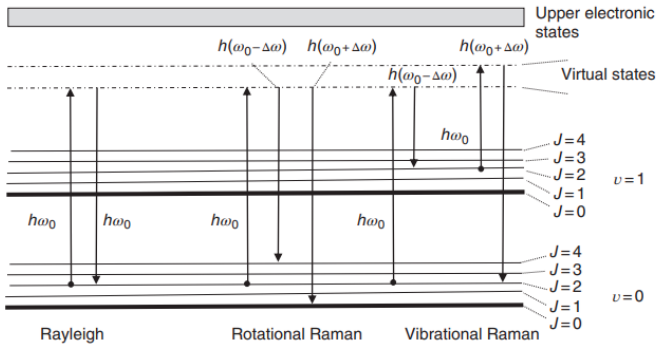

SOURCE: Villar and Matias (2020).

If the optical property of the medium related to its molecular arrangement, characterized by the refractive index, remains constant and homogeneous, the light passes through in a forward propagating manner, as the molecular vibration cancels out the backwards propagation vector as shown by the solution of Huygens's wave propagation principle (MILLER, 1991; SALEH; CARL, 2007). The variation of refractive index between molecular interfaces or small-scale fluctuations in the medium causes the molecular vibration to scatter photons in different directions and a part of the energy (less than 1%) is scattered the backwards direction (SIMMONS; POTTER, 1999). In a macroscopic scale, the amorphous glass present in the optical fiber cores gives rise to several backscattering centers due to the randomly arranged SiO_2 molecules and the presence of voids.

Other types of scattering can occur when photons and phonons interfere as they are absorbed and emitted by molecular vibration. When this occurs, frequency of vibration differs from the incident light frequency, and the phenomenon is called inelastic scattering. Inelastic scattering can be caused by the Brillouin or Raman effect. If sufficient energy is pumped into the optical fiber, or transparent medium, a small part of the energy (less than 0.01%) can cause the molecular virtual energy transition in the emission process to differ from its initial state due to interaction with optical phonons. The change in energy level causes the molecule to vibrate in a different mode and the scattering to occur at a different optical frequency than the incident photon, phenomenon called Raman effect. The Brillouin effect happens when the frequency of vibration of the molecules is changed due to the interaction of photons and thermally driven vibrations, called acoustic phonons, propagating though the fiber (OKAMOTO, 2006). The Brillouin Frequency Shift (BFS) is proportional to the vibration energy and temperature at that

region of the optical fiber. Stimulated Raman Scattering (SRS) and Stimulated Brillouin Scattering (SBS) are stimulated emissions which occur at higher levels of optical power input, as it is required to change the quantized vibrational or rotational energy levels of the molecule (IPPEN; STOLEN, 1972).

FIGURE 4 – LIGHT SCATTERING FREQUENCIES SPECTRUM

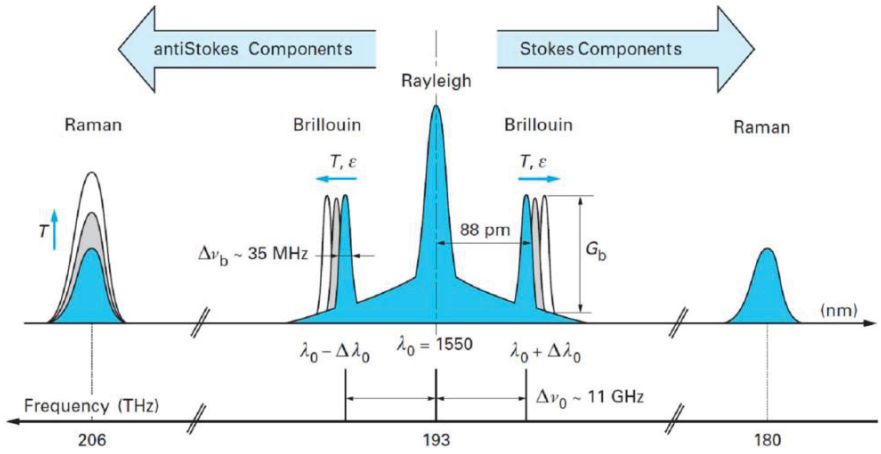

SOURCE: Hsu, Lee and Kuan (2021).

The properties of light scattering are used as methods of distributed fiber sensing and can be categorized depending on which scattering property is being related to the physical process. A type of DFOS that uses SBS is called Brillouin Optical Time Domain Analysis (BOTDA) based on the effects of two counter-propagating light waves in an optical fiber (IPPEN; STOLEN, 1972). BOTDA measures the Brillouin Frequency Shift occurring due to the change in strain and temperature at regions of the optical fiber (BAO; WEBB; JACKSON, 1996). The frequency shift is related to the optical and acoustic velocities in the medium. Another technique using Brillouin scattering is based on the backscattering of the light, called Brillouin Time Domain Reflectometry (BOTDR). In Fang; Su and Ansari (2021), a type of BOTDA sensor called AT-BOTDA (Amplitude Transfer-Brillouin Optical Time Domain Analysis) was used to determine the dynamic strains of a beam with a spatial resolution of only a few millimeters. Raman OTDR distributed sensors have been extensively used for temperature monitoring and differently than BOTDR the system is not sensitive to strain, avoiding cross-sensitivity between strain and deformation (LI; ZHANG, 2022).

2.2 COHERENT RAYLEIGH BACKSCATTERING FOR DISTRIBUTED ACOUSTIC SENSORS

In Taylor *et al.* (1993), the first version of a Rayleigh scattering based DAS system based was introduced. Today, the sensor has gained notoriety when compared to Brillouin and Raman based sensors (HARTOG, 2017). One of the advantages is that the sensor is able to measure dynamic strain and temperature signals in a quantitative linear manner and along many kilometers of optical fiber using a single interrogator. FIGURE 5.a and FIGURE 5.b demonstrate the physical concept behind DAS. As a light pulse travels through the optical path, the interaction between light and matter causes scattering of light in all directions caused by micro-inhomogeneities throughout the length of the path. This physical phenomenon takes place when the effective diameter of the matter, associated with non-homogeneities in the optical fiber core, is often less than the length of the incident wave (TSUJIKAWA; TAJIMA; ZHOU, 2005). Some of the scattering travels in the opposite traveling direction of the light pulse, thus, called backscattering (FIGURE 5.a). One way to implement a DAS system is to combine the Optical Time Domain Reflectometer (OTDR) principle with a coherent light source. Thus, a coherent optical pulse of short duration is launched in the optical fiber and, when reaching non-homogeneous regions, part of the light is backscattered. Due to the high coherence of the light, regions of the same dimension in the spatial length of the incident pulse have close phase relationships, and therefore the backscattering of each one causes interference in the receiver. When measured by a duration corresponding to the time of propagation and backscattering of light over the entire length of the optical fiber, the signal results in a coherent and distributed pattern of points of which the location, phase and intensity are sensitive to local disturbances. As vibration causes mechanical strain in the optical fiber, the backscattered light suffers changes in its amplitude and phase (FIGURE 5.b). Each subsequent light pulse is used to measure the backscattering property at a given instant in time.

FIGURE 5 – PHASE SENSITIVE DAS OPTICAL SIGNAL

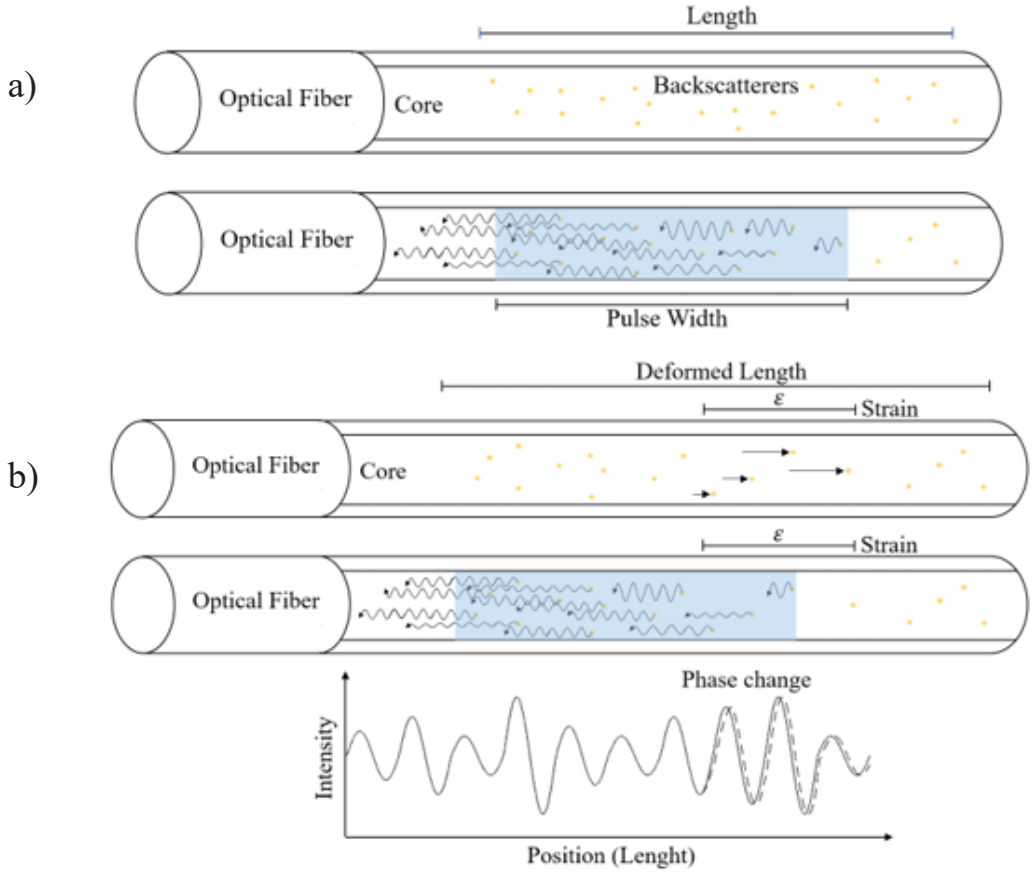

SOURCE: The author (2023).

LEGEND: a) The randomly positioned backscatterers in the optical fiber reflect part of the propagating light back into the interrogator as the light pulse, with a fixed width, excites them. b) Strain causes change in the position, spacing of backscatterers and relative density of the optical fiber resulting in a change of phase of the backscattered signal.

This technique presents spatial resolution directly proportional to the optical pulse width. However, there is a compromise between spatial resolution and signal-to-noise ratio (SNR), since shorter pulses result in lower energy scattering (CHEN; LIU; HE, 2018). Axial and radial strain within the fiber results in changes in the phase and amplitude of the backscattered signal due to the interaction of light in each scattered region, explained by the Pockels elasto-optic coefficients.

There are several types of Distributed acoustic sensors based on Rayleigh backscattering. Some of them are based on phase of the backscattered pulse, called theta-DAS or ϕ-OTDR, and others based on light power amplitude. In amplitude-based DAS, the optical signal is post-processed to correlate the optical intensity of the signal to strain. In this arrangement, the mechanical load causes changes in the density of scatterers. Compression

causes the back scatterers to come closer and the optical backscattered signal intensity is increased, whereas a decrease in the density of scatterers cause a lower signal intensity. This method of vibration sensing has a significant disadvantage caused by the non-linearity of the strain measurements. Conversely, phase sensitive DAS measures the phase change attributed to the modulated light wave as consequence of mechanical load. As the fiber elongates or shortens, two physical phenomena occur: the position of the backscatterers move linearly with strain and the refractive index changes proportionally to strain causing a variation in the infinitesimal speed of light at the vibration position. Both effects show a linear relationship between strain and phase-change. Thus, phase sensitive DAS can derive the expected dynamic strain or deformation value linearly using the Time of Arrival (ToA) developed with OTDR. In Chapter 3, the photo-elastic effect which describe the association between phase change of the optical signal and strain is described. In Shang *et al.* (2022), a revision of the recent developments of this technology is described, as depicted in FIGURE 6.

FIGURE 6 – DEVELOPMENT OF DAS

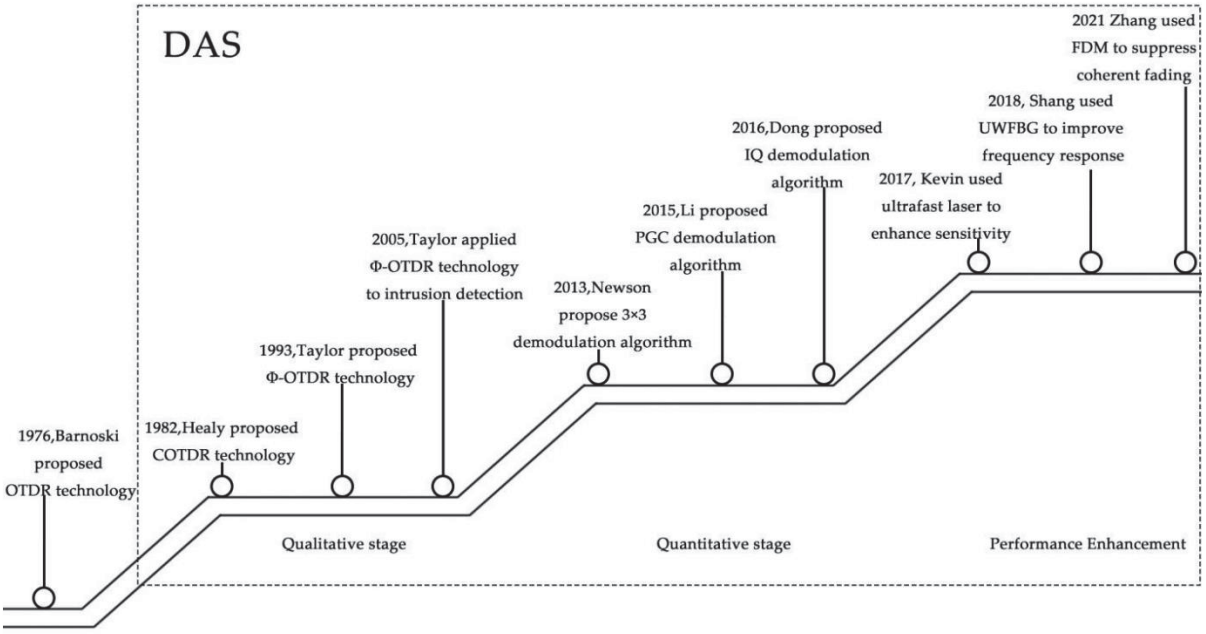

SOURCE: Shang *et al.* (2022).

Several new DAS topologies and methods have been studied to improve the performance of the sensor system in a trade-off between cost, complexity, sensibility, sampling rates and sensing length (CHEN; LIU; HE, 2019; CHEN et al., 2019; FENG et al., 2018; LU et al., 2017; MARTINS et al., 2016; WANG et al., 2020b). The sensor surpassed the qualitative

stage with the invention of phase sensitive detection and most of the recent studies are aimed at improving the performance parameters of the interrogator as discussed in the next sections.

2.2.1 Spatial Resolution and Sensing Length

The spatial resolution indicates the minimum distinguishable spatial scale along the sensing fiber (WANG et al., 2020a). Due to the mechanism of measurement, the pulse of light is modulated through an Acusto-Optical Modulator (AOM) which creates pulses of light with a fixed finite width. As a consequence, the measurand often becomes a convolution between the physical quantity along the optical fiber and light pulse time-domain characteristics. In recent studies, the minimum pulse time can as short as a few nanoseconds, which relates to a pulse that occupies less than one meter of the optical fiber. TABLE 1 demonstrates recent developments of DAS with the acquired spatial resolutions and sensing length.

TABLE 1 – DEVELOPMENTS AND SPATIAL RESOLUTIONS

Method	Pulse Width	Spatial resolution	Sensing Length	Reference
Conventional ϕ-OTDR	10 μs	1 km	14 km	Juarez et al., 2005
Conventional ϕ-OTDR with distributed application	250 μs	25 m	175 km	Wang et al., 2014
Live phase-shift keying	-	2.5 cm	500 m	Martins et al., 2016
Frequency sweep pulse and pulse compression	2 μs	30 cm	19.8 km	Lu et al., 2017
Double interferometers with bilateral filtering	50 μs	0.8 m	2 km	Feng et al., 2018
Time-gated digital OFDR with matched filtering	20 μs	0.8 m	9.8 km	Chen et al., 2018
Time-gated digital OFDR with bi-directional Raman amplification	20 μs	5 m	105 km	Chen et al., 2019

SOURCE: Chen et al, 2019; Feng et al., 2018; Juarez et al., 2005; Chen et al, 2018; LU et al., 2017; Martins et al., 2016; Wang et al., 2014.

The mechanical strain suffered by the optical fiber is measured as a smoothed quantity over a resolution length. FIGURE 7 demonstrates the resulting strain of coiled optical fibers undergoing positive strain with regions left in rest. The resulting signal measured by DAS considering a spatial resolution encompassing the region described is given by the average strain.

FIGURE 7 – SIGNAL REPRESENTATION OF A COILED OPTICAL FIBER DIVIDED INTO STRAINED AND UNSTRAINED REGIONS

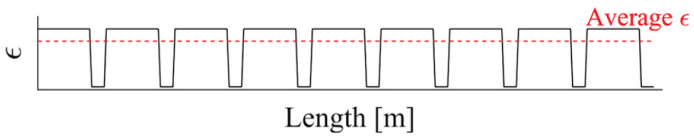

SOURCE: The author (2023).

Thus, if the optical fiber is in compression and tension states within the spatial resolution, the sensitivity of the system degrades rapidly as the integral of such strain state is close to zero. This might occur when the optical fiber is vibrating in flexural or string modes.

2.2.2 Gauge length and Phase Unwrapping

As mentioned, the spatial resolution is a parameter often influenced by the size of the propagating pulse of light in the optical fiber. Considering phase sensitive DAS, the sampling rate, however, of the measured backscattered light phase change is determined by the DAQ. As the acquisition rate of commercially available DAQ has increased along the years, the sampling resolution is substantially smaller than the spatial resolution. DAS phase demodulation procedures can be based on coherent detection or direct detection. Coherent detection uses digital demodulation to extract phase data based on the beat signal of the local oscillator and the backscattered light at different frequencies. In heterodyne detection, a type of coherent detection, the gauge length is a signal processing parameter that defines the spatial length through which phase differentiation is performed. In other words, the differentiating interval between two measured phase signals is deemed the gauge length. As mentioned by Hartog (2017), the gauge length is required to be higher than the spatial resolution occupied by the pulse width in order to properly differentiate between excitation signals along the optical fiber. In coherent detection the gauge length differentiation is done digitally which enables the

reprocessing of data acquired considering different gauge lengths. In direct detection, the differentiation is carried out in the optical domain. A consequence of the selected gauge length is related to the sensibility of the sensor. Higher gauge lengths compare values of strain induced phase change spatially distant from each other causing an increase in measured phase change. Since the measured phase is interferometric, *i.e.* periodic, this phase signal is obtained by using IQ demodulation followed by phase unwrapping along spatial dimension to ensure the proper counting of integer 2π cycles regarding the wavelength of the light beam. FIGURE 8 describes the phase unwrapping algorithm used in DAS, where the red function represents the backscattered light and the blue dots the unwrapped measured signal.

FIGURE 8 – UNWRAPPING ALGORITHM REPRESENTATION USED FOR PHASE RECONSTRUCTION

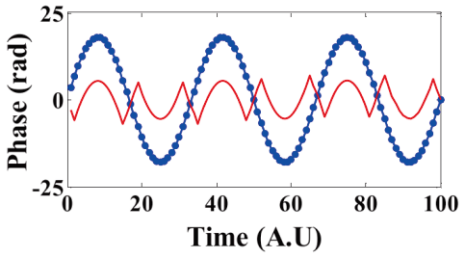

SOURCE: (HE et al., 2020a)

The phase difference between two neighboring regions will be the sum of phase changes due to random local strain between those two locations, plus a linear component due to their difference in distance. Thus, such physical behavior implies a trade-off between the spatial resolution and linearity response that can effectively be achieved by DAS (CHEN; MASOUDI; BRAMBILLA, 2019). The differentiating interval through which the DAS resulting phase changes signal $\delta\phi$ is obtained, so-called gauge length assures the compromise between the spatial resolution and response linearity of the sensed strain (CHEN; MASOUDI; BRAMBILLA, 2019).

2.2.3 Sensibility and Signal-to-Noise Ratio

As mentioned above, the gauge length is an important parameter that determines the distance between two spatial points along the fiber that are compared to reconstruct the strain signal measured. A longer gauge length causes the DAS system to detect smaller changes in optical phase, increasing the sensibility on the system. On the other hand, higher sensibility of

the system is also known to introduce unwrapping distortions if the phase signal surpasses a change of $[-\pi,\pi]$ (DEAN; CUNY; HARTOG, 2017). FIGURE 9 demonstrates the results of a study by Dean, Cuny and Hartog (2017) that analyses the effects of gauge length on axially incident P-waves. This study shows that an optimal gauge length can be selected, highlighted by the green region ($\mathrm{SNR} \geq 90\%$) on FIGURE 9(a). The selection of a highly sensitive gauge length parameter causes phase jumps in the demodulated signal if the strain surpasses the wavelength of the light pulse. As mentioned before, an unwrapping algorithm is used to reconstruct the continuous phase measurement. However, as shown in FIGURE 9(b) in the red region, if the ratio between strain or the spatial wavelength caused by mechanical excitation and gauge length is exceedingly high, the unwrapping algorithm fails to reconstruct the signal, and the SNR diminishes considerably.

FIGURE 9 – GAUGE LENGTH EFFECTS IN (a) SNR FOR A GIVEN SPATIAL WAVELENGHT EXCITATION AND (b) RESULTING WAVELENGTH

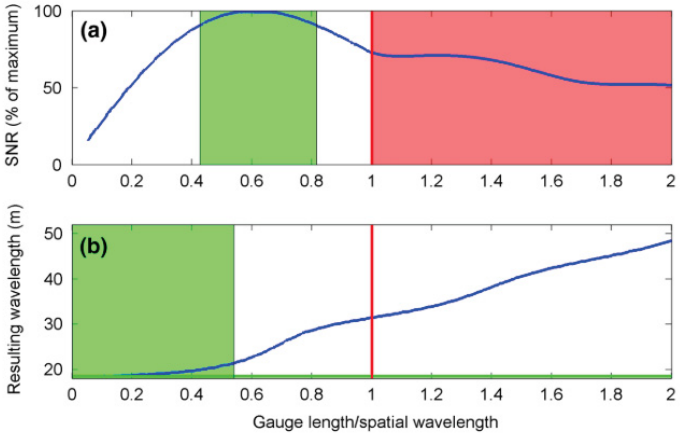

SOURCE: Dean, Cuny and Hartog (2017).

The inability to process the phase unwrapping consistently for high strain distribution in the optical fiber leads to a signal with higher noise and distortion. Another source of noise discussed in the literature is called signal fading, caused by the random distribution of Rayleigh scatters along the fiber (HE et al., 2018).

In (Ono et al., 2018), the authors demonstrate that significant suppression of Rayleigh scattering in glasses is achieved when a compression method is applied during the melted phase of the manufacturing of the glass. In contrast, in Westbrook *et al.* (2020), the authors propose

a method of increasing the Rayleigh scattering by exposing the core to UV induced refractive index perturbations providing increased sensibility in fiber sensing applications such as DAS.

2.3 DISTRIBUTED ACOUSTIC SENSOR FOR MECHANICAL VIBRATIONS

The types of mechanical vibration detected by distributed optical fiber sensors can be divided into two categories: direct mechanical vibrations and acousto-mechanical vibrations. Direct mechanical vibrations are measured if the optical fiber is in "bonded" contact with a structure. Usually, the rigidity and mass of the structure is considerably higher than the optical fiber and the optical fiber deforms according to the deformation of the structure. The technology has industrial applications such as monitoring railroad systems, leak detection in pipelines, Structural Health Monitoring (SHM) of civil structures, intrusion detection and others (HE; LIU, 2021; JUAREZ et al., 2005; LIEHR; MÜNZENBERGER; KREBBER, 2019; MUGGLETON et al., 2020; WIESMEYR et al., 2020). Recent Structure Health Monitoring (SHM) studies claim that distributed optical fibers present enormous advantages in sensing SHM systems of civil structures using distributed acoustic sensors (BARRIAS; CASAS; VILLALBA, 2016).

As a way to overcome the distributed nature of DFOS, some studies use a small section of the fiber as measurable instrument. In Chen et al. (2017), the authors used an Optical Frequency Domain Reflectometry (OFDR) based distributed optical fiber sensor to detect damage in a beam-like structure. This study developed a model for the strain transmissibility function to infer the damage on the structure. In SHM, changes in the dynamical characteristics of the modelled structure can be used to detect damage or failure. Thus, SHM systems require continuous real-time monitoring of several points in the studies structure. Structural identification is facilitated using DAS, as several positions of the structure can be measured simultaneously and continuously. For example, in Pellone et al., (2020), the author utilized another OFDR to detect bonding defects in typical wing spar, as shown in FIGURE 10. The distributed optical fiber sensor used in this experiment possesses a spatial resolution of only 2.6 mm and the fiber under test is 2 meters long. Differently than DAS, this type of sensor is able to detect the dynamic strain with spatial resolutions as low as a few millimeters, in expense of effective measurable length. Similarly to Pellone et al. (2020), Ciminello (2019) also uses a OFDR sensor with spatial of 5 millimeters and optical fiber deployed in a serpentine format to perform SHM of a small stiffened plate, as described in FIGURE 11.

FIGURE 10 – DISTRIBUTED OPTICAL FIBER SENSOR IN WING SPAR

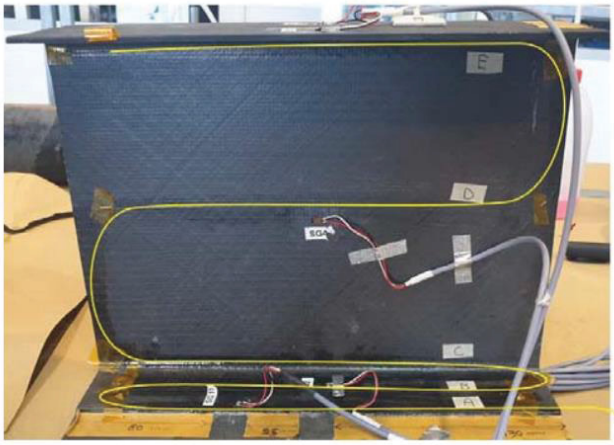

SOURCE: Pellone et al. (2020)

FIGURE 11 – DISTRIBUTED OPTICAL FIBER SENSOS INSTALLATION IN STIFFINED PLATE

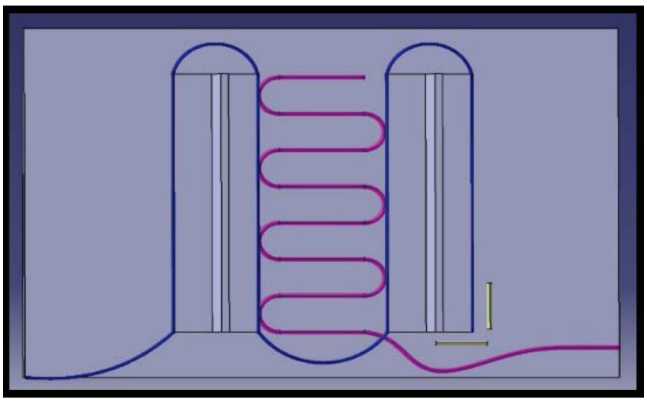

SOURCE: Ciminello (2019).
LEGEND: In blue lines, a conventional optical fiber arrangement is shown and in purple a serpentine optical fiber arrangement is demonstrated.

In contrast to OFDR and FBG sensors which measure localized signals, many recent studies with DAS comprises of detecting vibration, wave propagation velocity identification and usage of statical methods to develop indirect vibration information of large structures due to the lower spatial resolution (LIEHR et al., 2019; BAO; CHEN, 2016; WU et al., 2020).

Another area of interest related to DAS sensing regards the acoustic coupling between the optical fiber and acoustic wave. In He et al. (2020b), a modified version of DAS is developed to improve acoustic signal reconstruction. In the article, a speaker is used to play music while the DAS optical fiber reconstructs the sound signal (FIGURE 12). The Power Spectrum Density (PSD) of the played music and DAS signal are compared (FIGURE 13). Although the article demonstrates a new method of enhancing DAS acoustic measurements, the

authors did not consider the natural frequencies of fixed-fixed arrangement of the optical fiber which would have an important impact in the system PSD response.

FIGURE 12 – ACOUSTIC EXPERIMENT USING DAS OPTICAL FIBER AND SPEAKER

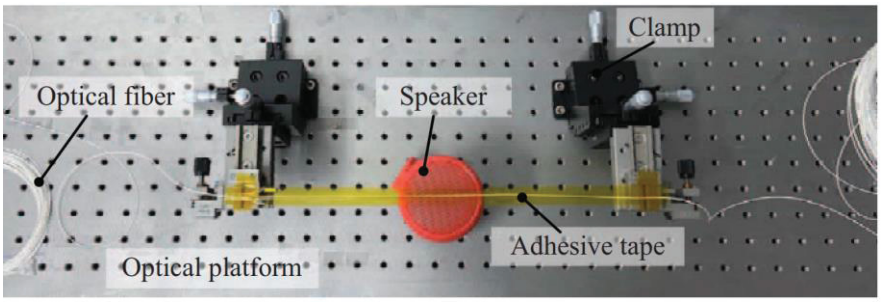

SOURCE: He et al. (2020b)

FIGURE 13 – PSD OF MUSIC SIGNAL MEASURED BY DAS SYSTEM WITH AND WITHOUT SIGNAL PROCESSING

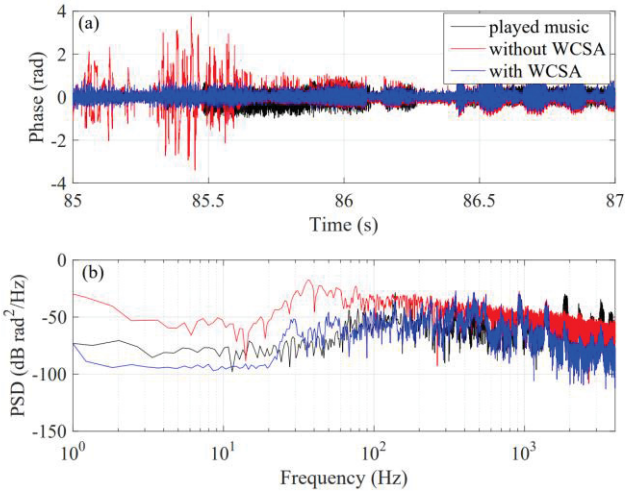

SOURCE: He et al. (2020)

Similarly, in Zhang et al. (2020), the authors placed the optical fiber of a DAS system in an anechoic chamber and in a reverberant chamber. An acoustic source is placed under the 1 meter fixed-fixed length of the optical fiber and the response of the system is measured. This paper claims that authors improve the experimental environment by using an anechoic chamber and propose a new methodology for DAS signal processing. However, once again, the vibration characteristics of the fixed-fixed length of the fiber are not taken in consideration.

In contrast, earlier, Oliveira et al. (2010) and Pohl et al. (2013) discuss the interaction of acoustic waves, mechanical waves and the characteristics of light propagation in an optical device structure. The authors simulate the flexural, torsional and longitudinal first vibration

modes of an acousto-optic modulator device using FEM (FIGURE 14). The simulation shows agreement with experimental results.

FIGURE 14 – FEM MODEL OF ACUSTO-OPTICAL DEVICE

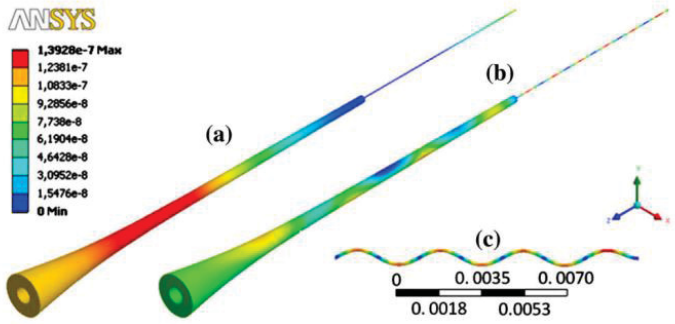

SOURCE: Oliveira et al. (2010)

Silva et al. (2016) continued the work of Pohl et al. (2013) and numerically modelled the mechanical behavior of an optical fiber under longitudinal excitation. In this paper, a sinusoidal longitudinal load with random amplitudes is applied to a 5mm optical fiber and to an AOM composed of an optical fiber, a horn and a piezoelectric diaphragm. The results demonstrate that the flexural vibration modes are not measured by the sensor system as the bending strain is almost null in the centerline of the optical fiber

FIGURE 15.

FIGURE 15 – FEM MODAL ANALYSIS OF ACUSTO-OPTICAL MODULATOR

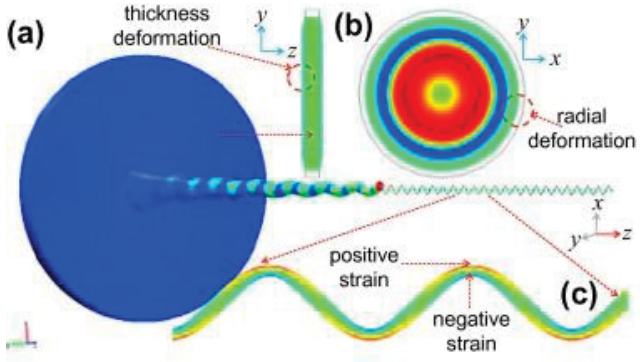

SOURCE: Silva et al. (2016)

Although many studies in the field of distributed acoustic sensors are concerned with improving acoustic performance, the optical fiber and the vibro-acoustic interaction between pressure waves and mechanical waves is not taken in consideration.

2.4 WELL MONITORING WITH DAS

Recent industrial advances and population growth have increased the global demand of energy sources. The oil and gas industry plays a central role in meeting the global energy demand and presents great economic importance. The process of hydrocarbon production involves installing multiple extraction wells to drain the contents of the underground reservoir. In the production phase of oil and gas extraction, the well can be described as an underground factory and the efficiency of production depends upon the employment of cost-effective technologies (SMITH; MAITLAND, 1998). The optimization of well productivity offers a significant reduction in investment risks and a substantial increase in profitability. Also, production optimization can lead to higher recoverable amounts of reservoir content, the ratio between recoverable amount and total amount of hydrocarbon in the reservoir is called recovery rate. With the need of higher recovery rates and less investment risks, the idea of "smart wells" was introduced.

In the 1990s, the term smart well was introduced based on the concept of using downhole sensors and remotely operated process control that enable continuous real-time well monitoring and an efficient production control (VALVATNE et al., 2003). Many studies of smart wells can be found in the literature: Tubel e Hopmann, (1996); Robinson (1997); Bosworth et al. (1998); Holmes et al. (1998); Greenberg (1999); Hamer and Freeman (1999), Yeten and Jalali, (2001); Sinha et al. (2001).

The added value due to the use of smart wells in oil fields, as mentioned by Konopczynski and Ajayi (2008), can reach 9% for each well and a 25% addition in recovery rates. As pointed out by Carvajal, et al. (2017), some of the elements of smart wells consist of discrete, distributed or quasi-distributed permanent sensors, packers that provide the seal between regions of the wellbore wall and Inflow Control Valves (ICV) controlled by a Hydraulic Power Unit (HPU), as Illustrated in FIGURE 16. All these elements are required to be monitored and controlled individually in real time in each control zone of the wellbore.

FIGURE 16 – MAIN ELEMENTS OF SMART WELLS INSTALLATION.

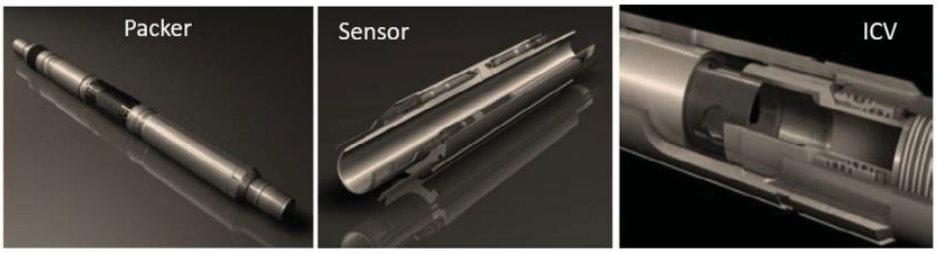

SOURCE: Carvajal et al. (2017)

In addition, the monitoring of well productivity and control require means to transfer information between wellhead and wellbore. The main component that carries out this function are the cables. The cables are used to transfer data, carry electrical energy and assist in the employment of sensors, as described in FIGURE 17. Due to the high salinity and acidity present in the wellbore as well as high probability of mechanical shock, the cables are protected with metal shielding and a polymer coating (BAKER et al., 1995).

FIGURE 17 – MODELS OF CABLES USED IN WELLS.

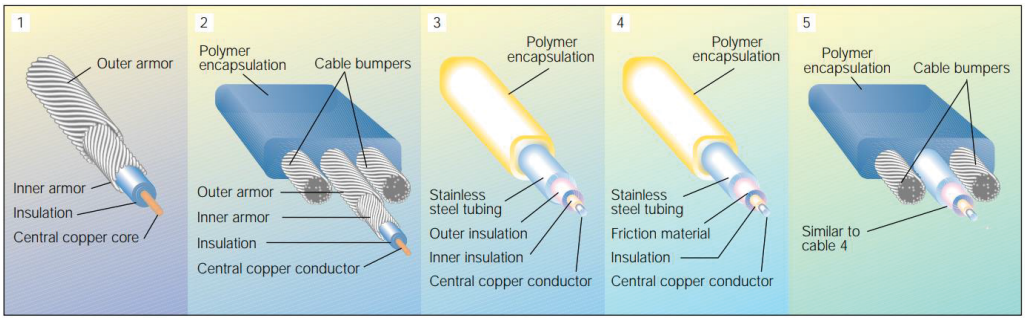

SOURCE: Baker et al. (1995)

The optical cables also use polymeric coatings and is comprised of either monomode or multimode optical fibers (JUNIOR et al., 2006). Externally, a Kevlar element is used to protect against longitudinal traction and to sustain the cable structure without losing mobility; The cables are fixed to the production column via metallic clamps, as shown in FIGURE 18.

FIGURE 18 – CABLE SUPPORT COMPONENTS IN PRODUCTION WELLS.

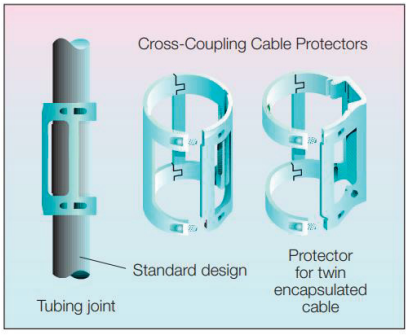

SOURCE: Baker et al. (1995).

Since the year 2000, a substantial growth in the number of wells with permanent optical fiber sensors has occurred due to the development of more robust optical fiber sensors, cables and interrogators in the market. Wells with optical fibers are present today in many different oil and gas fields such as in the North Sea, Alaska, Gulf of Mexico, Middle East and South America. The first wellbore optical fiber sensor installed was in a Shell well in 1993 by Optoplan S.A. (KRAGAS et al., 2002). In this well, the optical fiber sensor was used to measure temperature and pressure changes. The sensor system used is constructed by micro manufactured silicon resonators coupled to the optical fiber. In the 2000s, permanent optical fibers are used to obtain pressure, temperature, flow identification, flow phase fraction and seismic activity, amongst other information (KRAGAS et al., 2002). FIGURE 19 shows the installation of an optical fiber cable in a well using a Swagelok connector.

FIGURE 19 – INSTALLATION OF OPTICAL FIBER MONITORING SYSTEM IN ON LAND WELL.

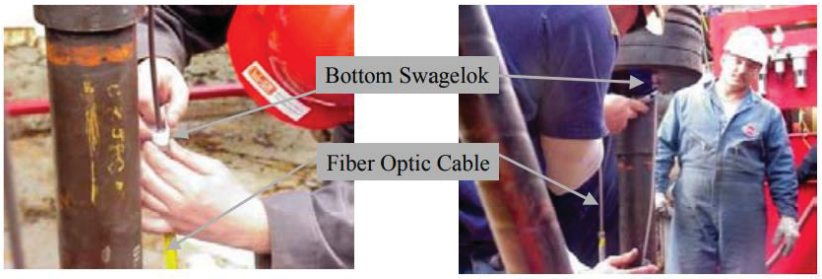

SOURCE: KRAGAS et al. (2002)

Williams (2012) introduced the use of DAS to monitor the structural health of pipelines. Since then, many studies of DAS in wellbore applications have been developed and the quality of measurements have increased rapidly due to investments from the oil and gas industry (PANHUIS et. al, 2014). Some studies of this application include: Boone et al (2014); Johanessen et al (2012); Molenaar et al (2011, 2012); Ugueto et al (2014); (Mateeva et al (2012). DAS systems offer specific advantages in well monitoring compared to classic monitoring sensors, such as geophones or accelerometers. Wells can reach up to many kilometers of depth, distributed optical fiber sensors excel due to the ability to measure along the whole length of the well in real-time. In addition, distributed optical fiber sensors can be used for both acoustics and temperature measurements by using a combination of DAS and DTS. According to the literature, DAS and DTS systems can achieve a minimal spatial resolution of 1 meter and sampling rates up to 20kHz in wellbore applications, presenting vital

contributions to the monitoring of oil extraction as high quality and high frequency monitoring are required (PANHUIS et al., 2014).

As described above, several studies concerning the application of DAS and DTS sensors have been developed in the past years. Improvements in the quality of the DAS measurements are vital to improve recovery rates and risk management in oil and gas production.

Today, DAS optical fiber sensors are used as a viable alternative to obtain seismic data, pressure distribution, fluid flow identification, and other physical information of hydrocarbon wells. The characteristic of DAS in measuring acoustic signals permits applications in seismic surveying. Vertical seismic profiling (VSP) is a process of acquiring the seismic profile around a wellbore using vertically placed seismic wave sensors. Mateeva et al. (2014) indicates that DAS incurs lower costs as an alternative to geophones for VSP in wells.

Daley et al. (2013) demonstrates the use of DAS to carry out vertical seismic profiling of deep wells. Results showed that the optical fiber sensor delivered a vertical seismic profile with high quality signals up to 3 km, whereas geophones were able to effectively monitor p-waves up to 1600 meters. The cable used in this breakthrough study is described in FIGURE 20. The cable in protected by capillary tube and a metallic casing as described in FIGURE 20.a and FIGURE 20.b and is coupled to a rigid structure. This method of cable construction is called Fiber in Metal Tube (FIMT) and is coated by a polymer layer called flatpack, as described in yellow in Figure 15.a. In another study mentioned in this article, DAS sensors were employed in CO_2 injection wells with up to 2 km in depth. The results showed that DAS produced higher quality vertical seismic profiles, for P-waves, when the cable employed did not use the external polymer layer and solely the exterior metallic protection.

FIGURE 20 – A) CABLE USED TO SECURE OPTIC FIBER IN DAS SENSING; B) ILLUSTRATION OF THE CABLE'S CROSS-SECTION; C) CABLE INSTALLATION IN A LAND WELL.

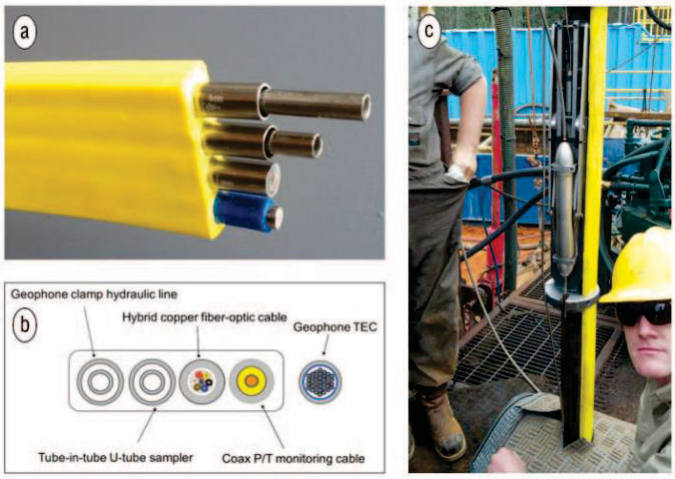

SOURCE: Daley et al (2013)

This study showed that the coupling between optical fiber, cable and external environment affects the performance of DAS sensors. The cable and coupling mechanism are discussed in the next section.

2.5 DAS CABLE DESIGN IN MONITORING APPLICATIONS

As aforementioned, the mechanical behavior of the mechanical system of the optical fiber dictates the performance of DAS measurements. Thus, the interface between optical fiber, cable and external environment affects the applicability of the sensor. A generic multimode Primary Coated Optical Fiber (PCOF), contains three concentric layers, as shown in FIGURE 21. In the case of a monomode optical fiber center, the 8 μm diameter core is made from silica. The propagation of light occurs in the core. A cladding is drawn around the core with a different refraction index. Externally, a primary coating provides mechanical resistance to the optical fiber. The mechanical properties of generic optical fibers, from manufactures Corning© and FiberCore© with and without coating are listed in TABLE 2.

FIGURE 21 – SIZING AND COMPOSITION OF PRIMARY COATED OPTICAL FIBER (PCOF).

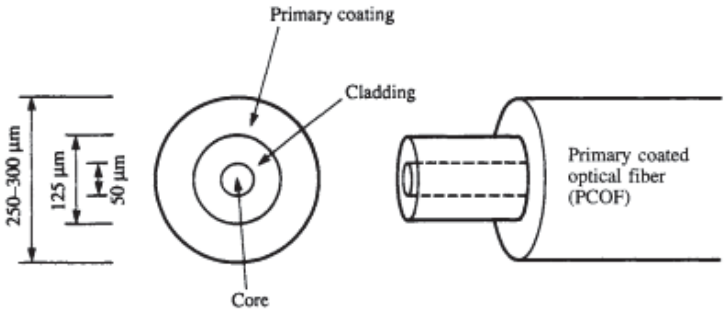

SOURCE: Elliott e Gilmore (2002)

TABLE 2 – MECHANICAL PROPERTIES OF GENERIC OPTICAL FIBERS.

Fiber	***E_g (GPa)***
Standard Fiber with Coating	16.56±0.39
Standard Fiber without Coating	69.22±0.42
Photosensitive fiber without Coating	68.56±1.47

SOURCE: Antunes et al. (2012)

In the patent EP 2 418 466 A2 from Taverner et. al (2012), a DAS system with FIMT cabling and external layers is proposed for applications in oil wells. The cross-section of the cable is shown in FIGURE 22, where the optical fiber is encapsulated by an external tube (303) which is involved by another stainless-steel tube (302). The author indicates a cable filling of toxitropic gel material, grease composites or foams for permeabilization and lubrication of the optical fiber. The filling is used to limit the movement of the optical fiber and reduce the strain induced by the natural frequencies of the optical fiber. The last layer of material used to involve the FIMT is a polymer or composite material (304) with high elasticity and low bulk modulus in order to improve acoustic coupling. Furthermore, holes (502) are proposed in the design of the external layer. These provisions are made to allow for better acoustic coupling between cable and environment, as well as cable and optical fiber.

FIGURE 22 – FIMT PATENT FOR ENHANCED ACOUSTIC COUPLING FOR DAS (EP 2 418 466 A2).

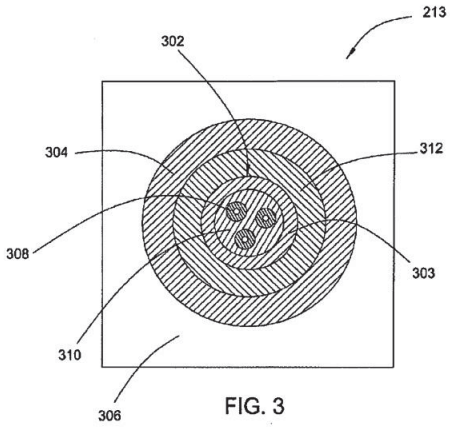

SOURCE: den Boer et al. (2012)

FIGURE 23 –PATENT FOR INCREASED ACOUSTIC COUPLING USING WATER ACOUSTIC IMPENDANCE (EP 2 418 466 A2).

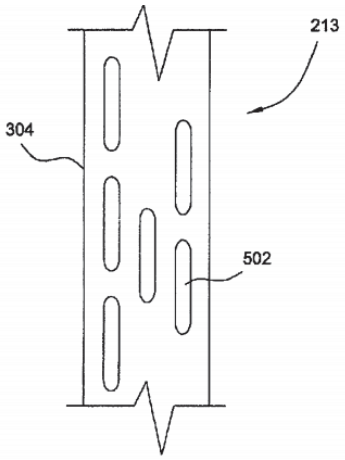

SOURCE: den Boer et al. (2012)

An example of a cable with improved broadside acoustic wave sensing is shown in den Boer et al. (2012), as shown in FIGURE 23. The cable is designed with a thin membrane where the optical fiber is coupled. The low elasticity of the thin membrane increases the vibration due to perpendicular acoustic waves. In this patent, the optical fiber can also be attached to an inertia member which would amplify mechanical vibrations. The cable designs are shown in FIGURE 24 and FIGURE 25.

FIGURE 24 – DAS CABLE PATENT WITH MEMBRANE FOR ACOUSTIC AMPLIFICATION

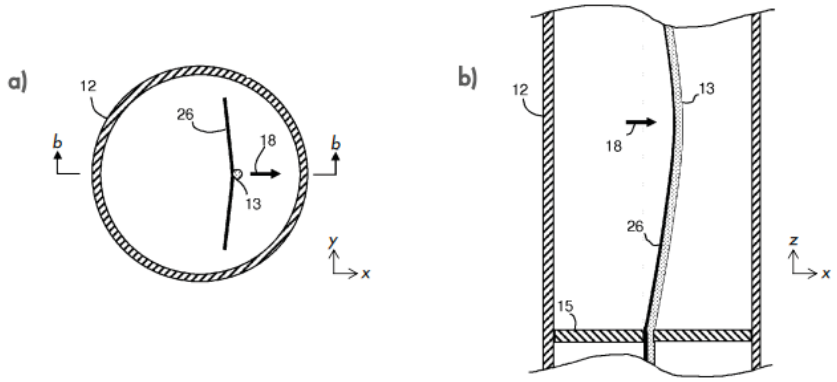

SOURCE: den Boer et al. (2012)

FIGURE 25 – DAS CABLE PATENT WITH INERTIA MEMBER FOR ACOUSTIC AMPLIFICATION

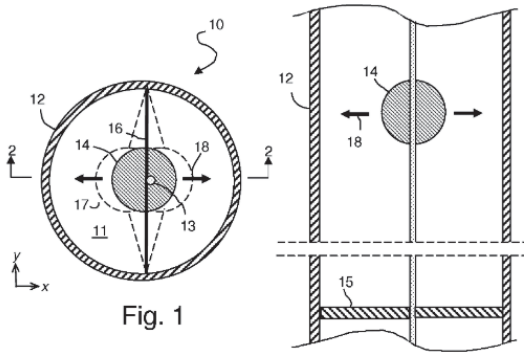

SOURCE: den Boer et al. (2012)

In Follet et al. (2014), various commercially available optical fiber cables for sensing using DAS are investigated. In this article, Fiber in Metal Tube (FIMT) cable, an air filled FIMT cable, called AirFIMT, a gel filled FIMT cable, called Gel-FIMT, a fiberglass matrix cable, called FiberMT and other several cabling designs were tested. FIGURE 26 The results show that AirFIMT and FiberMT show higher sensibility to external excitation when compared to the other types of cabling. Furthermore, the article concludes that direct coupling between cabling and well walls produce a higher signal to noise ratio (SNR).

FIGURE 26 – COMPARISON CHART OF THE AMPLITUDE CAPTURED BY DIFFERENT CABLES.

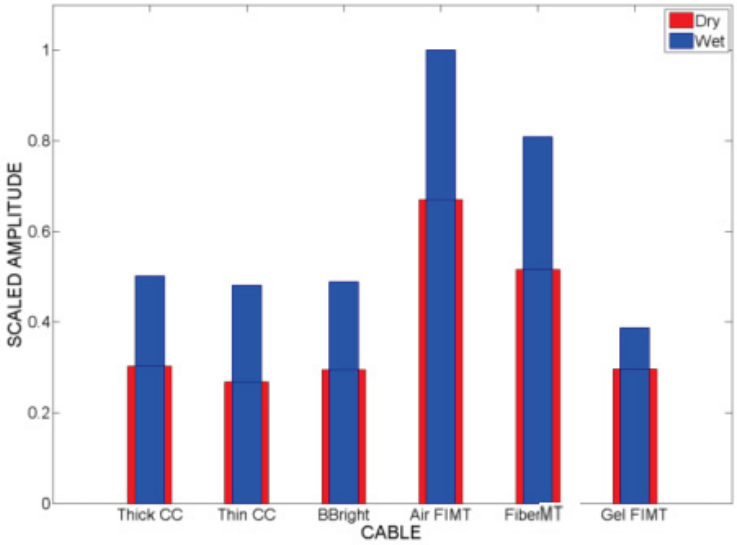

SOURCE: Follett et al. (2014)

Kuvshinov, 2016, investigated the use of helicoidal wounded optical fibers for DAS applications. Increased sensibility to broadside waves was found as helicoidal angle is decreased, as shown in the graph of FIGURE 27. Numerical results obtained an optimum helicoidal angle as function of Poisson's ratio to be 30 degrees for plastic cables. Other studies using helicoidal wounded optical fiber cables can be found in Hornman et al. (2013), Lumens et al. (2013) and Mateeva et al. (2014).

Frignet and Hartog (2014) used a removable distributed optical fiber sensor for inland Vertical Seismic Profiling (VSP) analysis. In this study, several cable types are compared in the experiments. The results show once again that the mechanical coupling between cable and external environment can reduce drastically the quality of the measured signal. Also, the author pointed out that using pre-tensioned cables can hinder mechanical coupling. FIGURE 28 shows a cable prototype with 7 helically wounded optical fibers protected by steel armor and external layers.

Ning and Sava (2018) suggest the use of 5 parallel helicoidal wounded optical fibers to completely reconstruct the 3-dimensional strain tensor state as result of an arbitrary angled acoustic wave, as shown in FIGURE 29

FIGURE 27 – RESPONSE OF HELEICOIDAL WOUNDED OPTICAL FIBER FOR SEISMIC SIGNALS

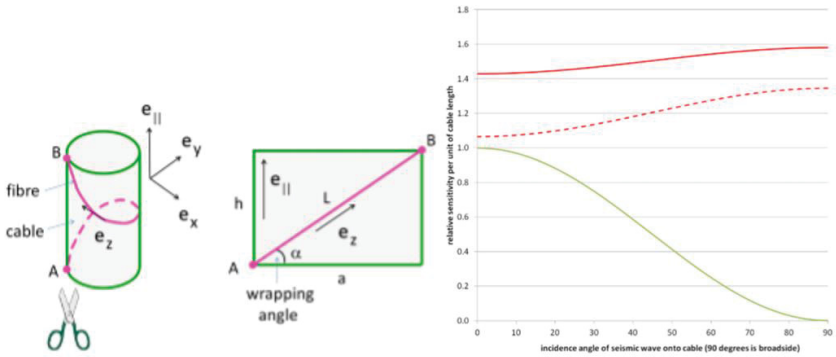

SOURCE: Kuvshinov (2016)

LEGEND: in the graph, the red line is the response for 30 degrees wrapping angle, while in green, the response for a straight fiber.

FIGURE 28 – PROTOTYPE OF CABLE WITH 7 FILAMENTS OF COATED OPTICAL FIBERS

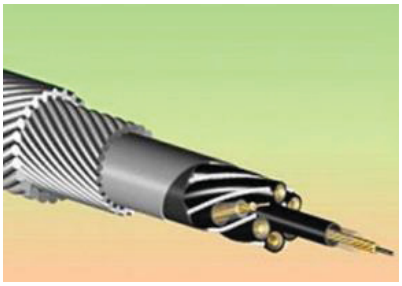

SOURCE: Frignet and Hartog (2014)

FIGURE 29 – ARRANGEMENT OF HELICAL FIBER FOR 2,44 CENTIMETER TUBE AND HELICAL ANGLE OF 20º.

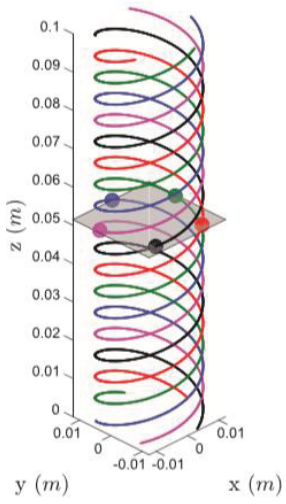

SOURCE: Ning and Sava (2018)

The cited studies give an overview of the importance of modeling the mechanical behavior of the vibroacoustic interaction between optical fiber and environment to increase sensibility and current limitations of DAS sensors.

2.6 THESIS OBJECTIVES

This thesis aims at analyzing applications of the distributed optical fiber sensor DAS as a vibration and acoustic continuous local sensor and enhance the quality of the acquired data through modeling of the mechanical dynamic system and its resulting optical effects. A new method of monitoring local dynamic strain of structures using DAS is proposed. The method uses a serpentine configuration to measure strain locally at discrete regions of the structure and with higher sensibility enabling DAS to determine, among other vibration information, the strain frequency response function (SFRF) of the structure and vibration modes. In the field of acoustics, initially, the design, construction and validation of an anechoic chamber is presented. Subsequently, acoustic experiments are developed to investigate improvements in gain, signal to noise ratio, and enhancing the quality of the acoustic signal response by the selected arrangement. In order to achieve these objectives, an elastic-optical mathematical model is developed and experimental results are compared to numerical results obtained with the Finite Element Method (FEM) software. The main objectives can be divided into the following specific objectives:

- Develop a methodology of employing mathematical models that relate dynamic strain response of the optical fiber to the backscattered light signal interrogated by the sensor.
- Implement numerical models with FEM software to validate the proposed mathematical relationship between mechanical excitation and optical signal comparing it with experimental results.
- Analyze and implement methods of enhancing DAS sensor in measurements of the vibration response of known structures.
- Design, commission and validate an anechoic chamber for experiments with the DAS sensor in a noise free environment.
- Analyze methods of measuring acoustic excitations in structures using coupled optical fibers and implement methods to enhance DAS as an acoustic sensor with improvements on sensibility, signal to noise ratio and source location.

2.7 THESIS CONTRIBUTION

In comparison to the response of classical sensors, such as accelerometers and microphones, the transfer function between input and output signal is known, and are mostly constant for the specified frequency range. The equivalent dynamic system of classical sensors can be modeled as single-degree-of-freedom systems. However, due to the spatial resolution and optical interference of the DAS sensor, the response of optical fibers to vibration is dependent on the installation, coupling and static mechanical state of the optical fiber, as shown in FIGURE 30. Thus, in view of the literature review presented in this chapter, this thesis' main contributions are:

- The development a methodology of employing an elasto-optic mathematical model that calculates the expected dynamic strain response of the optical fiber arrangement to the backscattered light signal interrogated by the sensor

FIGURE 30 – COMPARISON BETWEEN MICROPHONE TRANSFER FUNCTION AND DAS TRANSFER FUNCTION.

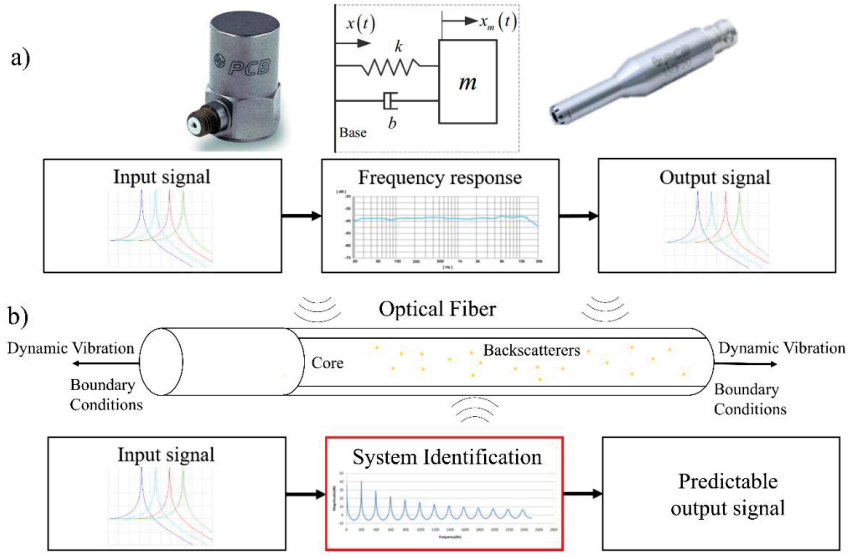

SOURCE: The author (2023).

- Implementation of numerical models with FEM software that calculates the SFRF of the optical fiber arrangements in order to compare the proposed mathematical relationship between mechanical excitation and optical signal in physical experiments.
- Introduction of a new optical fiber arrangement analyzed by the methodologies mentioned above. The arrangement is able to enhance the signal response of the sensor by up to 12.9 dB and allows more than 10 times improvement in the sensing resolution of the system enabling the acquisition of the modes of vibration and SFRF of small structures and devices.
- Development of experiments using the mentioned arrangements to reconstruct SFRF of acoustic induced excitations in structures using coupled optical fibers and the DAS system.

3 THEORETICAL BACKGROUND

In this section, the Photo-elastic model relating optical signal and dynamic strain is introduced using the theory proposed by Friedrich Pockels (POCKELS, 1890). Also, the constitutive models based on theory of vibration of continuous systems and the solution for the generalized coordinate system problem are described in view of the calculation of the SFRFs. Finally, the theory of acoustic coupling in structures by oblique propagating waves is shown.

3.1 PHOTO-ELASTIC EFFECT THEORY ON OPTICAL FIBERS

The following section obeys the rules of Einstein's notation, where a free index, in a monomial, indicates an implicit summation along the validity of this index (LAI; RUBIN; KREMPL, 2010).

The strain-optic coefficients relate the change in refractive index to the strain state of the optical continuum (BERTHOLDS; DANDLIKER,1988). The change in refractive index of the material is related to the change in phase and amplitude of the light wave. Thus, the dynamic signal measured by DAS can be predicted by the photo-elastic effect. Pockels phenomenological theory of photo-elasticity of crystals relate the polarization constants, B_{ij}, and the components of elastic strain, ε_{kl}, by the Pockels' strain-optic constants, p_{ijkl}. Considering the polarization constants of the undeformed crystal medium as B_{ij}^{0}, the change of polarization can be expressed as (NARASIMHAMURTY, 1981)

$$B_{ij} - B_{ij}^{0} = p_{ijkl}\varepsilon_{kl}, \tag{1}$$

where B_{ij} can also be defined as the impermeability tensor or the reciprocal of the dielectric tensor, K_{ij}. In Eq. (1), Pockel's equations assume that the polarization changes linearly in relationship with strain. Due to the symmetry in the B_{ij} and ε_{kl} tensors, the indexes can be simplified as

$$B_{1} - B_{1}^{0} = p_{11}\varepsilon_{1} + p_{12}\varepsilon_{2} + p_{13}\varepsilon_{3} + p_{14}\varepsilon_{4} + p_{15}\varepsilon_{5} + p_{16}\varepsilon_{6}, \tag{2}$$

$$B_2 - B_2^0 = p_{21}\varepsilon_1 + p_{22}\varepsilon_2 + p_{23}\varepsilon_3 + p_{24}\varepsilon_4 + p_{25}\varepsilon_5 + p_{26}\varepsilon_6\,, \tag{3}$$

$$B_3 - B_3^0 = p_{31}\varepsilon_1 + p_{32}\varepsilon_2 + p_{33}\varepsilon_3 + p_{34}\varepsilon_4 + p_{35}\varepsilon_5 + p_{36}\varepsilon_6\,, \tag{4}$$

$$B_4 - B_4^0 = p_{41}\varepsilon_1 + p_{42}\varepsilon_2 + p_{43}\varepsilon_3 + p_{44}\varepsilon_4 + p_{45}\varepsilon_5 + p_{46}\varepsilon_6\,, \tag{5}$$

$$B_5 - B_5^0 = p_{51}\varepsilon_1 + p_{52}\varepsilon_2 + p_{53}\varepsilon_3 + p_{54}\varepsilon_4 + p_{55}\varepsilon_5 + p_{56}\varepsilon_6\,, \tag{6}$$

$$B_6 - B_6^0 = p_{61}\varepsilon_1 + p_{62}\varepsilon_2 + p_{63}\varepsilon_3 + p_{64}\varepsilon_4 + p_{65}\varepsilon_5 + p_{66}\varepsilon_6\,, \tag{7}$$

or in index notation as

$$\left(B_i - B_i^0\right) = \Delta B_i = \sum_{i,j} p_{ij}\varepsilon_j\,. \tag{8}$$

The impermeability tensor describes how easily the light propagates in a certain polarization direction in the media. The refractive index, n, is a dimensionless number that describes the ratio between speed of light in a medium and speed of light in vacuum. This parameter relates the phase retardation caused by strain. The relation between refractive index, dielectric tensor, K, and impermeability tensor, B, can be described as

$$B_i = \frac{1}{K_i} = \frac{1}{n_i^2}\,, \quad i = 1, 2, 3, 4, 5, 6. \tag{9}$$

Thus, the effect of strain in the change of refractive index in the optical fiber is given by

$$\Delta\left(\frac{1}{n^2}\right)_i = \sum_j p_{ij}\varepsilon_j\,. \tag{10}$$

Considering an isotropic crystal medium, several p_{ij} coefficients are cancelled. For fused silica which optical fibers are composed of, the change in refractive index can be assumed to be $\Delta\left(1/n^2\right)_i = -2\Delta n_i / n_0^3$, where n_0 denotes the unstrained refractive index parameter of the medium. Thus,

$$\begin{pmatrix}\Delta n_1\\ \Delta n_2\\ \Delta n_3\\ \Delta n_4\\ \Delta n_5\\ \Delta n_6\end{pmatrix}=\frac{-n_0^3}{2}\begin{bmatrix} p_{11} & p_{12} & p_{12} & 0 & 0 & 0\\ p_{12} & p_{11} & p_{12} & 0 & 0 & 0\\ p_{12} & p_{12} & p_{11} & 0 & 0 & 0\\ 0 & 0 & 0 & \frac{(p_{11}-p_{12})}{2} & 0 & 0\\ 0 & 0 & 0 & 0 & \frac{(p_{11}-p_{12})}{2} & 0\\ 0 & 0 & 0 & 0 & 0 & \frac{(p_{11}-p_{12})}{2}\end{bmatrix}\begin{pmatrix}\varepsilon_1\\ \varepsilon_2\\ \varepsilon_3\\ \varepsilon_4\\ \varepsilon_5\\ \varepsilon_6\end{pmatrix}. \quad (11)$$

In this equation, j = 1, 2, 3 relates to the longitudinal directions of strain (*x, y, z*), while indices j = 4, 5, 6 are related to shear strain (*xy, xz, yz*). Considering a load being applied longitudinally, along the *x* direction, in the optical fiber, and that the effective refractive index is transversal to the strain direction, the dynamic strain causes a change in refraction index given by

$$\Delta n_{eff}^{(y,z)}=\frac{-n_0^3}{2}\left[\varepsilon_1(1-\upsilon)p_{12}-\upsilon\varepsilon_1 p_{11}\right], \quad (12)$$

where υ is the Poisson's ratio and $n_{eff}^{(y,z)}$ is the effective refractive index related to the direction of light propagation. In single mode fibers and in the case of strain in the *x* direction, the effective index can be assumed to be Δn_y or Δn_z for example. The photo-elastic coefficients for typical glasses (silica) are given as $p_{11}=0.113$ and $p_{12}=0.252$ for a wavelength of 632.8 nm (BERTHOLDS; DANDLIKER, 1988). These authors also measured a Poisson's ratio of $\upsilon=0.15$. Recently, Roselló-mechó *et al*. (2016) measured the Pockels' coefficients and Poisson's ratio of optical fibers under axial strain as $p_{11}=0.116\pm0.017$ and $p_{12}=0.255\pm0.021$ at 1531 nm, and $\upsilon=0.17\pm0.01$, respectively. The total phase change measured by DAS is composed of two effects: the first is related to the change in refractive index, and consequent phase retardation caused by change in speed of propagation, and the second is related to the actual change in length of the optical fiber. Thus, the resulting change in phase due to dynamic strain longitudinally exciting the optical fiber is given by two terms, $\Delta\phi=L\Delta\beta+\Delta L\beta$, where $\beta\cong n_0k_0$ is the propagation constant of the mode in the fiber, which is proportional to the free-space wavenumber, k_0. Butter and Hocker (1978) describes the summations of both terms as

$$\Delta\phi = k_0 n_0 \Delta L \left(1 - \frac{n_0^2}{2} \left(p_{12} - \upsilon (p_{11} + p_{12}) \right) \right). \tag{13}$$

A simplified version of Eq. (13) is found in Fang et al. (2012) and reproduced in Wang et al. (2020) as the sensing principle of DAS. The equation considers an effective photo-elastic coefficient, γ, as

$$\gamma = \frac{-n_0^2}{2} \left[(1 - \upsilon) p_{12} - \upsilon p_{11} \right], \tag{14}$$

and the change of fiber length, $\Delta L = \varepsilon_1 L$. Finally, the phase difference, $\Delta\phi$, due to longitudinal strain in the optical fiber can be expressed as

$$\Delta\phi = (1 + \gamma) n_0 k_0 L \varepsilon_1 . \tag{15}$$

The external vibration acting longitudinally on the optical fiber creates a 1-dimensional distribution of phase differences, $\Delta\phi$. On the case of DAS, the width of the probe pulse creates backscatters as it passes through the region and is overlapped causing an internal pulse modulation. The pattern of the interference of the backscattered signal is demodulated and used to obtain the vibration, which is linearly proportional to the additional laser phase, as demonstrated in Eq. (15). In DAS, a local oscillator modulates the backscattered signal.

It is important to consider that the effects of a dynamic point strain acting longitudinally on the optical fiber causes a phase change at all location beyond that length of fiber. The differentiating interval through which the DAS resulting phase changes signal $\delta\phi$ is obtained, so-called gauge length, assures the compromise between the spatial resolution and response linearity of the sensed strain (CHEN; MASOUDI; BRAMBILLA, 2019). Thus, the resulting phase change function is described as

$$\delta\phi(x,t) = \frac{4\pi n_0 G_L \xi \varepsilon_1 (x,t)}{\lambda} , \tag{16}$$

being G_L the gauge length, λ the wavelength of the probe pulse, and ξ the photo-elastic scale factor, calculated as $\xi = 1 + \gamma$, which for silica is assumed to be 0.78 (KOYAMADA et al., 2006; MASOUDI; NEWSON, 2017; SEAFOM, 2018). The formulation presented in this section was developed for axial strain. In the cases of bending and radial pressure, Appendix A discusses these effects and the resulting phase change.

3.2 MECHANICAL VIBRATIONS OF CONTINUOUS SYSTEMS

The optical fiber is a cylindrical solid with an extremely small diameter when compared to the length dimension. According to vibration theory, a continuous mechanical system vibrates depending upon the types of loads it can support. It is assumed that an optical fiber can support tension, thus, behaving as a string. FIGURE 31 demonstrates the corresponding free body diagram.

FIGURE 31 – FREE BODY DIAGRAM OF STRING MODE DYNAMIC MOTION

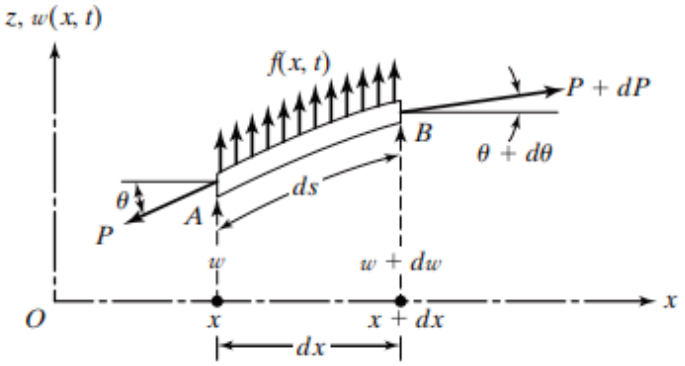

SOURCE: Rao (2011)

In the diagram, $f(x,t)$ is the loading function in the transversal direction, w, along the optical fiber position, x. P is the tension exercised by the structure, θ is the angle between the undeformed fiber direction and tension load direction and ρ is the material density per length. The dynamic behavior of the system can be described as (RAO, 2017)

$$P\frac{\partial^2 w(x,t)}{\partial x^2} + f(x,t) = \rho\frac{\partial^2 w(x,t)}{\partial t^2}. \tag{17}$$

In addition, the optical fiber structure is also able to vibrate in longitudinal modes, as described by a bar model. This type of vibration is the basis for some acousto-optic devices such as the AOM. In FIGURE 28, the illustration of the dynamical motion of the longitudinal vibration modes for a uniform cross-section bar is derived and illustrated, deriving the following expression

FIGURE 32 – FREE BODY DIAGRAM OF BAR MODE DYNAMIC MOTION.

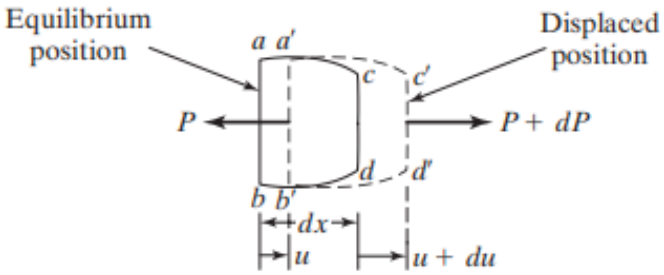

SOURCE: Rao (2011)

$$EA\frac{\partial^2 u(x,t)}{\partial x^2} + f(x,t) = \rho A\frac{\partial^2 u(x,t)}{\partial t^2}, \tag{18}$$

where u is the longitudinal displacement, E is the elastic modulus, A is the area and ρ is the density of the material. Finally, considering the structures that the optical fiber might be in contact with, the continuous mechanical system can support shearing forces, $V(x,t)$ and flexural moments, $M(x,t)$, as displayed in FIGURE 33. The optical fiber and structure surrounding the optical fiber, *i.e.* the optical fiber cable, can be modelled using a beam model, considering higher order modes or large diameter cables (TREYSSÈDE, 2010). The uniform beam cross-section problem is described as

FIGURE 33 – FREE BODY DIAGRAM OF BEAM MODE DYNAMIC MOTION

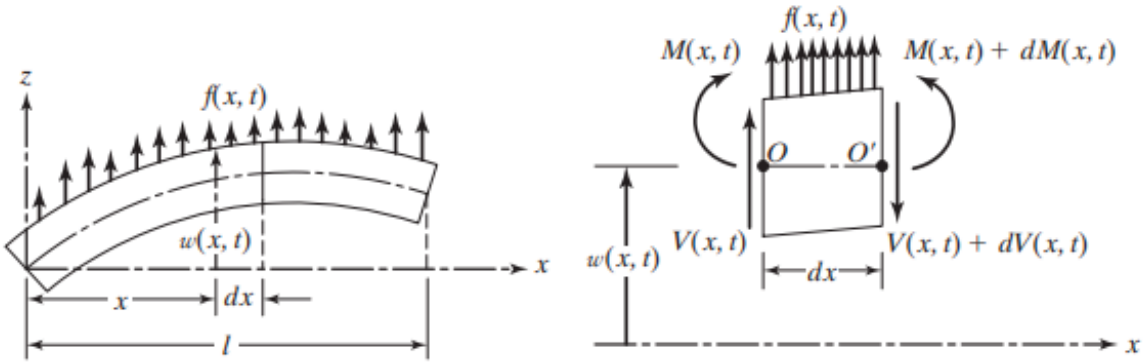

SOURCE: Rao (2011)

$$EI\frac{\partial^4 w(x,t)}{\partial x^4}+\rho A\frac{\partial^2 w(x,t)}{\partial t^2}=f(x,t)\,, \tag{19}$$

where E is the Young's modulus of the material and I the second moment of area. The optical fiber arrangements tested in thesis are attached to structures that present beam mode vibration. TABLE 3 compares the natural frequencies and velocity of wave propagation of each vibration type for the *n*-th mode. The velocity of wave propagation differs for each definition and, considering that the optical fiber can vibrate simultaneously in several modes of vibration, an analysis of the structural behavior of the optical fiber structure is required. Further, the wave speed of flexural modes is proportional to frequency, whereas in the other cases these frequencies are constants.

TABLE 3 – VIBRATION FEATURES BASED ON STRUCTURE TYPE FOR FREE-FREE BOUNDARY CONDITIONS

	String Vibration	**Bar Vibration**	**Beam Vibration**
Natural Frequency	$\omega_n=\frac{n\pi}{L}\sqrt{\frac{P}{\rho}}$	$\omega_n=\frac{n\pi c}{L}$	$\omega_n=\beta_n^{\,2}\sqrt{\frac{EI}{\rho A}}$ $\beta_1 L=4.7300$ $\beta_2 L=7.8532$ $\beta_3 L=10.9956$ $\beta_4 L=14.1371$ ...
Wave Speed	$c=\sqrt{\frac{P}{\rho}}$	$c=\sqrt{\frac{E}{\rho}}$	$c=\left(\frac{EI}{\rho A}\right)^{\frac{1}{4}}\sqrt{\omega}$

SOURCE: (RAO, 2017).

Considering the kinetic energy and potential energy in vibratory systems, the amplitude of vibration is a function of frequency, as shown in FIGURE 34. In the graph, for a constant velocity of vibration, the amplitude of displacement of the particles decreases as the frequency of vibration is higher, whereas the acceleration increases. Thus, for a given vibrating system, the amplitude of displacement decreases as frequency increases. DAS sensors measure strain, the differential of displacement, thus, for a given amplitude of vibration the signal the sensor measures also decrease as a function of frequency.

FIGURE 34 – DISPLACEMENT, VELOCITY AND ACCELERATION SENSIBILITY FOR CONSTANT VIBRATION ENERGY.

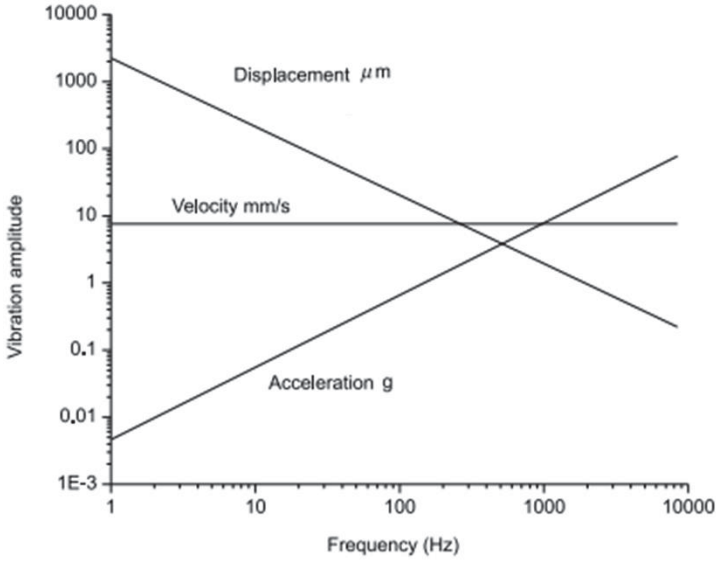

SOURCE: Sujatha (2010)

3.3 FINITE ELEMENT MODEL FOR VIBRATION ANALYSIS

The finite element method (FEM) is a numerical approach that solves the partial differential equations of several mechanical engineering problems through element approximations. FEM is capable of modeling complex boundary conditions and complex geometries through the Galerkin formulation of weighted residuals method. The solution of FEM is based on a system discretized in nodes and elements. In addition, FEM can be used to solve multiphysics interaction between fluids and solid structures. In FEM, the equations of motion of a structure under a dynamic excitation is given by

$$[M]\{\ddot{q}(t)\}+[C]\{\dot{q}(t)\}+[K]\{q(t)\}=\{f(t)\}, \tag{20}$$

where $[M]$, $[C]$ and $[K]$ denote the mass, viscous damping and stiffness matrices, whereas $q(t)$, $\dot{q}(t)$ and $\ddot{q}(t)$ represent displacement, velocity and acceleration vectors of the generalized coordinate of the *i*-th degree of freedom of the mechanical system, and $f(t)$ is the vector of external force.

The homogeneous solution of the Eq. (21) allows the calculation of the natural frequencies and the corresponding modes of vibration. Considering the homogenous solution, $q(t)=\{\phi\}e^{j\omega t}$, and no damping, $[C]=[0]$, the natural frequencies and mode shapes are found by the classic eigenvalue-eigenvector problem, described as

$$[K]\{\phi\}=\lambda[M]\{\phi\}, \tag{21}$$

where $\{\phi\}$ is the eigenvector, describing the mode shape, related to the $\lambda=\omega^2$ eigenvalue, describing the natural frequency. The Frequency Response Function (FRF), $H(\omega)$, is defined by the ratio between structural output response and input force excitation in the frequency domain. The finite element problem can be decoupled in the modal domain using the modal matrix obtained by the eigen solution, and the orthonormalized mass, damping and stiffness matrices. The displacement FRF can be described as

$$[H(\omega)]=\sum_{i=1}^{n}\frac{\{\phi_i\}\{\phi_i\}^T}{-\omega^2 m_i+\mathrm{j}\omega c_i+k_i}, \tag{22}$$

where m_i, c_i, k_i and ϕ_i are the modal mass, modal damping, modal stiffness and vibration mode related to the *i*-th mode, respectively, n is the total number of modes and j is the imaginary number.

3.3.1 Strain frequency response function

The DAS system measures the structural induced strain vibration in the optical fiber, thus, it differs from usual experimental modal analysis sensors, such as accelerometers. Based

on the theory of elasticity for small deflections, a relationship between longitudinal strain, ε_x, and displacement *u* can be obtained as (ALQAM; DHINGRA, 2019)

$$\varepsilon_x = \frac{\partial}{\partial x} u \,. \tag{23}$$

Similarly, the strain modes can be written as a function of the displacement modes:

$$\psi_i = \frac{\partial}{\partial x} \phi_i \,. \tag{24}$$

Strain can be described, using modal theory, as a summation of *n* number of modes:

$$\varepsilon(t) = \sum_{i=1}^{n} \psi_i q_i(t), \tag{25}$$

where q_i is the generalized modal coordinate at time *t*. The equation of motion can describe the system dynamics for a given input force F:

$$q_i = \frac{\phi_i \phi_i{}^T F}{-\omega^2 m_i + j\omega c_i + k_i} \,. \tag{26}$$

Thus, the relation between strain output and force input is described as

$$\varepsilon_i = \sum_{i=1}^{n} \frac{\psi_i \phi_i \phi_i{}^T F}{-\omega^2 m_i + j\omega c_i + k_i}, \tag{27}$$

and the SFRF can be described as (YAM et al., 1996)

$$\left[H^{\varepsilon}(\omega) \right] = \sum_{i=1}^{n} \frac{\left\{ \psi_i^{\varepsilon} \right\} \left\{ \phi_i \right\} \left\{ \phi_i \right\}^T}{-\omega^2 m_i + \mathrm{j}\omega c_i + k_i} \,, \tag{28}$$

where $\{\psi_i^\varepsilon\}$ is the *i*-th strain vibration mode, obtained by calculating numerically the derivative of the deformation mode shape with respect to the generalized coordinate.

3.4 SOUND INDUCED VIBRATION OF STRUCTURES

The mechanical problem involving the vibration of structures induced by free field acoustic sources is discussed in this section. As a propagating acoustic wave encounters the boundary of a second medium, the generation of reflected and transmitted waves occur (KINSLER et al., 1983). FIGURE 35 illustrates the problem. Considering the acoustic wave theory, the incident wave, p_i, reflected wave, p_r, and transmitted waves, p_t, can be described as

$$p_i = P_i e^{i(\omega t - k_1 x\cos\theta_i - k_1 y\sin\theta_i)}, \tag{29}$$

$$p_r = P_r e^{i(\omega t + k_1 x\cos\theta_r - k_1 y\sin\theta_i)}, \tag{30}$$

$$p_t = P_t e^{i(\omega t - k_2 x\cos\theta_t - k_2 y\sin\theta_t)}, \tag{31}$$

FIGURE 35 – SOUND TRANMISSION AND REFLECTION

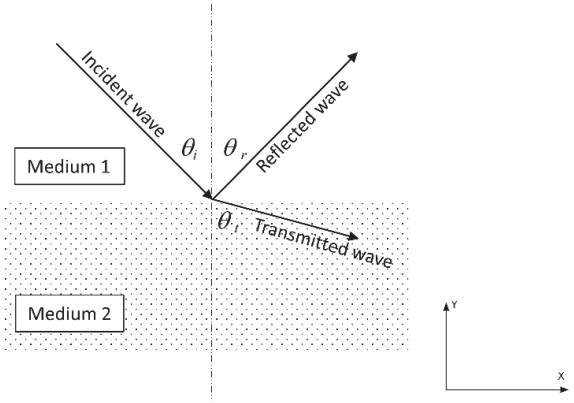

SOURCE: The author (2023)

where P_r, P_t and P_i are the amplitudes of the reflected, transmitted and incident waves, and k_1 is the wave number of medium 1 and k_2 is the wave number of medium 2. According to Snell's law for reflection and refraction, the incident wave angle, θ_i, and the reflected wave angle, θ_t, are related by

$$\frac{\sin\theta_i}{\sin\theta_t} = \frac{c_1}{c_2}\ , \tag{32}$$

where c_1 is the speed of propagation in the first medium and c_2 is the speed of propagation in the second medium. Considering the relation between pressure and particle velocity as the acoustic impedance, Z, given as

$$Z = -B\frac{\frac{\partial u}{\partial x}}{\frac{\partial u}{\partial t}}, \tag{33}$$

where *B* defines the bulk modulus of the material. For an isotropic medium, the acoustic impedance can be represented as

$$Z = \rho c\ , \tag{34}$$

where ρ denotes the density of the material and c the speed of sound.

The transmitted wave into the structure causes vibration with an intensity related to the incoming wave Sound Pressure Level (SPL) and the difference of impedance between media, given by

$$\frac{P_t}{P_i} = \frac{2Z_2\cos\theta_i}{Z_2\cos\theta_i + Z_1\cos\theta_t}\ , \tag{35}$$

considering a normal wave, the equation simplifies to

$$\frac{P_t}{P_i} = \frac{2Z_2}{Z_2 + Z_1}. \tag{36}$$

3.4.1 Properties of incident acoustic waves in the optical fiber and sensed structures

The optical fiber, cable or structure the optical fiber is attached to can be modelled as a uniform beam in a fixed-fixed boundary condition. An acoustic harmonic plane wave with

wavelength λ is incident upon the structure at angle θ, as shown in FIGURE 36. The trace wave speed, c_t , in the beam is given as

$$c_t = \frac{c_0}{\sin\theta} \tag{37}$$

FIGURE 36 – ACOUSTIC COUPLING OF INCIDENT ACOUSTIC WAVE.

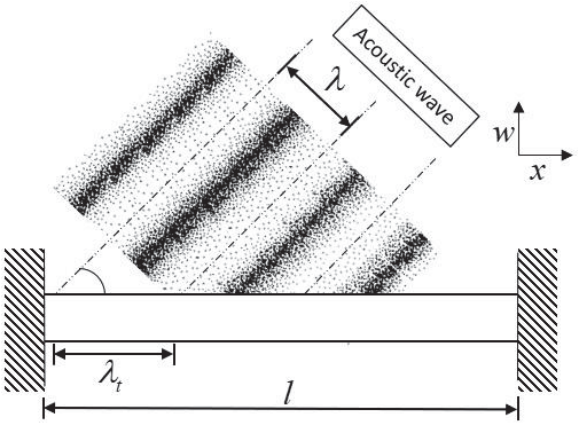

SOURCE: The author (2023)

In theory of continuum mechanics, the wave propagation in elastic solids is a function of the modulus of elasticity and density of the medium. However, in the problem posed, the harmonic acoustic excitation can affect the speed and wavelengths of the strain wave due to the direction of the incident wave, as shown in FIGURE 37.

FIGURE 37 – TRACE SPEED OF INCIDENT ACOUSTIC WAVE. A) ACUTE INCIDENT ANGLE, B) 45 DEGREES AND C) OBTUSE INCIDENT ANGLE.

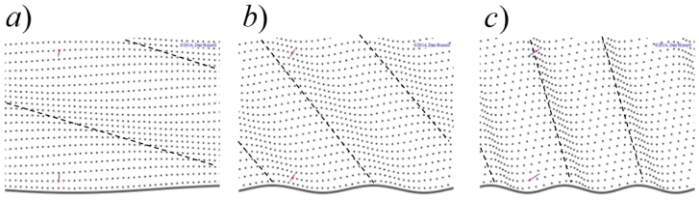

SOURCE: Adapted from Russel (2014).

According to Fahy and Walker (2018), The pressure distribution in the beam is given by

$$p(x,t) = Pe^{i(\omega t - k_t x)} \tag{38}$$

where k_t is the trace wavenumber, defined as $k_t = \frac{2\pi}{\lambda_t}$ and ω is the circular frequency. The Euler-Bernoulli beam theory can be used to describe the equation of motion of the system. The solution considering an incident acoustic wave is found using the sum of the complementary function and particular integral, where the complementary function is the solution of the free wave equation. Assuming fixed-fixed boundary conditions, the solution can be found (FAHY; WALKER, 2018)

$$y(x,t) = \frac{Pe^{j(\omega t - k_t x)}}{EIk_t^4 - \rho A\omega^2} + \left(A_1 e^{-jk_b x} + A_2 e^{jk_b x} + A_3 e^{-k_b x} + A_4 e^{k_b x} \right) \tag{39}$$

where I is the second moment of area, A is the area, the flexural wavenumber of the beam is given as $k_b = \left(\frac{\omega^2 \rho A}{EI} \right)^{\frac{1}{4}}$ while A_1, A_2, A_3 and A_4 are arbitrary constants. Equating the denominator to zero, gives a condition where the displacement goes to infinity. This is called a coincident condition, where the free flexural wavelength in the beam is equal to trace wavelength. Coincidence occurs similarly to a resonance condition and the coincidence frequency is dependent on the angle of the incident acoustic wave, θ, given as (FAHY; WALKER, 2018)

$$\omega_c = \left(\frac{\rho A}{EI} \right)^{\frac{1}{2}} c_0^2 \sin^2 \theta \tag{40}$$

Thus, the vibration response of the optical fiber or structure to acoustic waves is based on the relationship between its mechanical behavior, given by string theory or beam theory, and the complex loading condition defined by the incident acoustic wave, as described above. Furthermore, as mentioned by Dakin and Brown (2017), the sensibility of the optical fiber is given as function of incident angle of the acoustic wave ($\sin^2 \theta$).

4 METHODS AND MATERIALS

In this Chapter the materials and methods required for the results produced in this thesis are presented. The infrastructure required for the development of the apparatus presented in this section was assisted by the Petrobras Research and Development (R&D) project in a partnership between the Laboratory of Sensor Systems Technology (*Laboratório de Tecnologia em Sistemas Sensores* - LTSS) at the Federal University of Technology - Parana (UTFPR) and the Research Group of Vibrations and Sound in Mechanical Systems (*Grupo de Pesquisa de Vibrações e Som em Sistemas Mecânicos* - GVIBS) at Federal University of Paraná (UFPR) integrating fields of Mechanical Vibrations, Sensor Technology and Photonics. The section demonstrates the following topics:

- Development of a photo-elastic mathematical relationship based on the Pockel's elasto-optic coefficients used to calibrate the optical signals received by the DAS interrogator to the proposed optical fiber arrangements considering localized strain measurements;
- Description of an experiment using the proposed serpentine configurations to measure the frequency spectrum of the in-phase strain signals at discrete regions of a free-free aluminum beam of approximately 2.7 meters, enabling DAS to determine, among other vibration parameters, the strain frequency response function (SFRF). The experiment analyses the vibration signal response performance of five different optical fiber arrangements: with 1, 3, 6 and 9 coils and a straight long fiber arrangement. The beam was modelled using FEM with a model updating algorithm based on validated reference sensors;
- Description of the design, construction and validation of an anechoic chamber for acoustic experiments in view of the ISO 26101 standard describing the qualification of free-field environments is demonstrated.
- Description of an experiment using DAS with serpentine optical fibers as a sensor of acoustic-induced vibrations for a thin plate structure, representing a small device. The experiment compares normal (90°) incoming waves and 45° oblique incidence waves.

4.1 PHOTO-ELASTIC MODEL

The detected signal in the DAS system is divided into two beat signals, the backscattered signal incoming from the Fiber Under Test (FUT) and the beat signal from the local oscillator. The backscattered signal electromagnetic wave can be described as

$$E(t) = E_R(t)e^{i\left[(\omega+\omega_s)t+\varphi(t)\right]}, \tag{41}$$

where ω is the angular frequency of the light source, ω_S is the AOM shifted frequency and $\varphi(t)$ is the phase change from the refraction index variations. Due to the coherent light source, the interfered signal, $I(t)$, measured in the balanced detector is given by the beat signal passing through the Local Oscillator, resulting in

$$I(t) = |E_R|^2 + 2E_R(t)E_{LO}\cos(\theta)\cos\left(\omega_s t + \varphi(t)\right) + |E_{LO}|^2, \tag{42}$$

where θ is the angle between polarization states, E_r is the light intensity related to the backscattered light, E_{LO} is the light intensity related to the local oscillator. The second term of the equation carries the phase information of the optical fiber and the squared terms are filtered out using a band-pass filter as they present different beat frequencies in heterodyne detection. External excitation in the optical fiber causes changes in this phase as a result of varying refractive index. The decomposition of the beat signal into an In-phase (I) and Quadrature (Q) component separated by 90 degrees, called IQ demodulation, can be expressed as

$$\begin{aligned} I(t) &= E_R(t)E_{LO}\cos\left(2\pi(\omega_s-\omega_l)t+\varphi(t)\right), \\ Q(t) &= E_R(t)E_{LO}\sin\left(2\pi(\omega_s-\omega_l)t+\varphi(t)\right), \end{aligned} \tag{43}$$

where $(\omega_s - \omega_l)$ is the frequency difference between modulated signal and the local oscillator frequency. The amplitude and phase of the Rayleigh backscattered light wave is given by

$$\begin{aligned} Amplitude(t) &= \sqrt{I^2(t) + Q^2(t)}, \\ Phase(t) &= \arctan\left[\frac{Q(t)}{I(t)}\right] - 2\pi f_b t. \end{aligned} \tag{44}$$

The above equations describe briefly the demodulation method for a single Phase sensitive OTDR trace measured by DAS. The detection of change in refractive index is carried out by comparing two different positions on the optical fiber, as shown in FIGURE 38.

FIGURE 38 – ILLUSTRATION OF PHASE MEASUREMENT USING DAS.

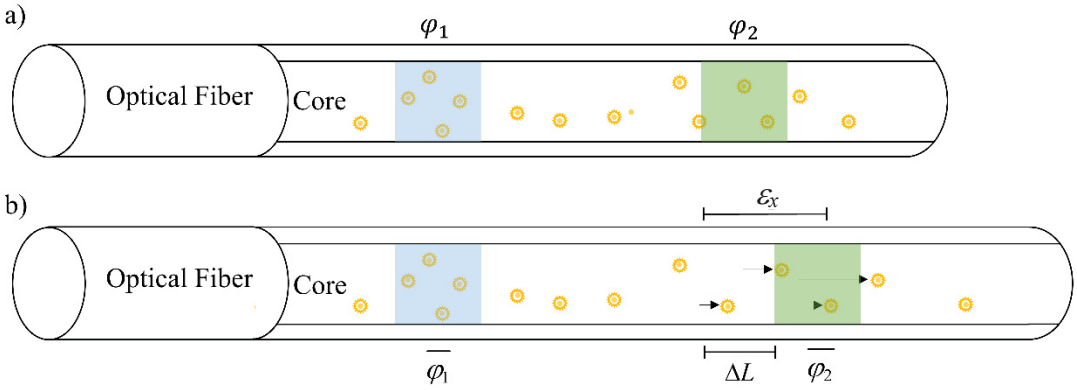

SOURCE: The author (2023).

Thus, the difference between phase in two positions in the optical fiber can be described as

$$\Delta\varphi = \varphi_1 - \varphi_2 = C\frac{2\pi n}{\lambda}2L \tag{45}$$

where C is an arbitrary constant defined for this example. After elongation of the optical fiber, the new phase difference, $\overline{\Delta\varphi}$, can be described as

$$\overline{\Delta\varphi} = \overline{\varphi_1} - \overline{\varphi_2} = C\frac{2\pi n}{\lambda}2\left(L + \Delta L\right). \tag{46}$$

Rearranging Eq. (45) and (46)

$$\overline{\Delta\varphi} - \Delta\varphi = C\frac{4\pi n}{\lambda}\Delta L, \tag{47}$$

The phase unwrapping algorithm is then used in the following manner

$$\Delta\phi(t) = \text{unwrap}\left[\arctan\left[\frac{Q(t)}{I(t)}\right]_{x=L} - \arctan\left[\frac{Q(t)}{I(t)}\right]_{x=L+G_L}\right]. \tag{48}$$

In order to achieve this comparison a distance between the positions of the fiber is selected, referred to as the gauge length, G_L. The measured discretized phase signal can be described, based on Pockel's Elastooptic Theory, as (SEAFOM, 2018)

$$\Delta\phi = \frac{4\pi n_0 G_L \xi}{\lambda}\varepsilon_x\,, \tag{49}$$

where ξ is given by rearranging Eq.(14). Considering multiple "frames" of ϕ OTDR traces, corresponding to the response between light pulses, the phase change can be described as

$$\begin{bmatrix} \Delta\phi_{x_1}^{t_1} & \Delta\phi_{x_2}^{t_1} & \cdots & \Delta\phi_{x_m}^{t_1} \\ \Delta\phi_{x_1}^{t_2} & & & \\ \vdots & & \ddots & \\ \Delta\phi_{x_1}^{t_n} & & & \Delta\phi_{x_m}^{t_n} \end{bmatrix} = \frac{4\pi n_0 G_L}{\lambda}\left(1 - \frac{n_0^2}{2}\left(p_{12} - \upsilon(p_{11}+p_{12})\right)\right)\begin{bmatrix} \boldsymbol{\varepsilon}_{x_1}^{t_1} & \boldsymbol{\varepsilon}_{x_2}^{t_1} & \cdots & \boldsymbol{\varepsilon}_{x_m}^{t_1} \\ \boldsymbol{\varepsilon}_{x_1}^{t_2} & & & \\ \vdots & & \ddots & \\ \boldsymbol{\varepsilon}_{x_1}^{t_n} & & & \boldsymbol{\varepsilon}_{x_m}^{t_n} \end{bmatrix} \tag{50}$$

or in index notation,

$$\Delta\phi_{x_j}^{t_i} = \frac{4\pi n_0 G_L}{\lambda}\left(1 - \frac{n_0^2}{2}\left(p_{12} - \upsilon(p_{11}+p_{12})\right)\right)\boldsymbol{\varepsilon}_{x_j}^{t_i}\,, \tag{51}$$

As demonstrated in Eq. 51, the measured strain is given by the comparison between the cumulative phase at points separated by G_L. Thus, the strain over a unit of spatial resolution is described as the integral of strain divided by the gauge length (BAKKU, 2015)

$$\left[\boldsymbol{\varepsilon}_{x_j}^{t_i}\right]_{DAS} = \int_{x_j-\frac{G_L}{2}}^{x_j+\frac{G_L}{2}} \frac{\varepsilon^{t_i}(x)}{G_L}\,dx\,, \tag{52}$$

In this thesis, optical fiber arrangements with lengths smaller than the spatial resolution of the system are developed. Considering a certain arrangement of an optical fiber where the structure induced strain, $\hat{\varepsilon}_x$, causes a deformation in the regions of the fiber coupled to the structure and the uncoupled fiber suffers significantly smaller strain, $\hat{\varepsilon}_0$, which is close to 0, the total strain measured by DAS can be calculated by comparing the length of strained and unstrained fiber. This is illustrated in FIGURE 39, for an arbitrary strained fiber.

FIGURE 39 – ARBITRARY DEFORMATION WITHIN THE OPTICAL FIBER SENSING RESOLUTION

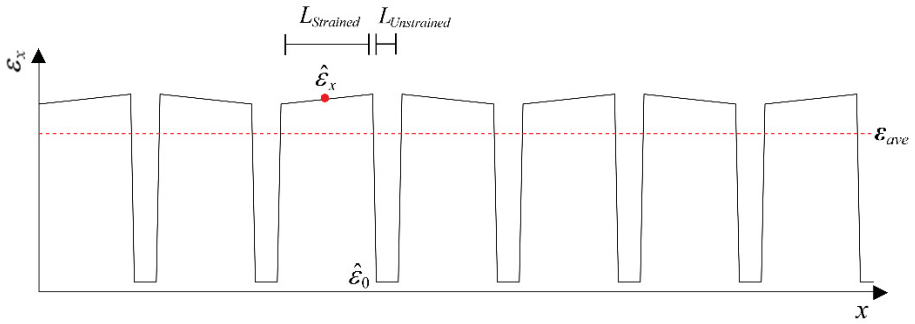

SOURCE: The author (2023).

Thus, the resulting strain seen by DAS, denoted as the average strain (ε_{ave}) is described as

$$\varepsilon_{ave} = \hat{\varepsilon}_{x_j} \frac{L_r S}{G_L} \tag{53}$$

Where S is the length of the sensor the L_r term is described as

$$L_r = \frac{L_{Strained}}{L_{Strained} + L_{Unstrained}} \tag{54}$$

Thus, the resulting strain measured by DAS can be described as

$$\left[\varepsilon_x \right]_{DAS} = \frac{\Delta\phi}{\frac{4\pi n_0 L_r S}{\lambda}\left(1 - \frac{n_0^2}{2}\left(p_{12} - \upsilon(p_{11} + p_{12})\right)\right)} \tag{55}$$

Considering a “sub-resolution” sensor, a “spread” factor, $E_s\left(L_r\right)$, related to the convolution of the pulse signal and strain can be added to the resulting equation as a calibration parameter. This new term is required when using small portions of fiber being strained within the spatial resolution divided by free fibers, incurring in regions of free fiber detecting small signals influenced from the neighboring strained regions. Eq. (55) and the unwrapping algorithm described by Eq (48) are used to convert the phase signal into measured dynamic strain and reconstruct the measured signal, respectively. Other terms can be added to the equation regarding the demodulation procedure. A term is defined for the efficiency of the unwrapping algorithm, E_w, which commonly decreases with frequency of vibration as a result of the number of phase measurement points per strain wavelength in the time-domain, and a term to account for errors in the positioning of the sensing vector in the spatial-domain, E_p. Eq. (55) becomes

$$\left[\boldsymbol{\varepsilon}_x\right]_{DAS}=\frac{\Delta\boldsymbol{\phi}}{\frac{4\pi n_0\boldsymbol{L_r}\boldsymbol{S}}{\lambda}\left(1-\frac{n_0^2}{2}\left(p_{12}-\upsilon(p_{11}+p_{12}\right)\right)}\boldsymbol{E}_s(L_r)\boldsymbol{E}_w(\omega,\Delta\phi,fs)\boldsymbol{E}_p(\Delta\phi) \tag{56}$$

where *fs* is the repetition rate of acquisition in DAS.

In this thesis, the parameters mentioned in Eq. (56) are not fully analyzed and the equation used for the results is described in Eq. (55). However, the full equation is displayed in this chapter as a proposition for future studies.

4.1.1 Sensor Design and Arrangement

The methodology described in the previous section is a useful tool to calculate the expected strain occurring at a given installation of the fiber in structural or acoustic monitoring. The arrangement and coupling between the strained structure and optical fiber significantly affects the results gathered. Thus, for a given arrangement, the sensibility of the sensor is calculated. FIGURE 40 shows the parameters characterizing a serpentine arrangement developed in this thesis.

FIGURE 40 – SERPENTINE ARRANGEMENT

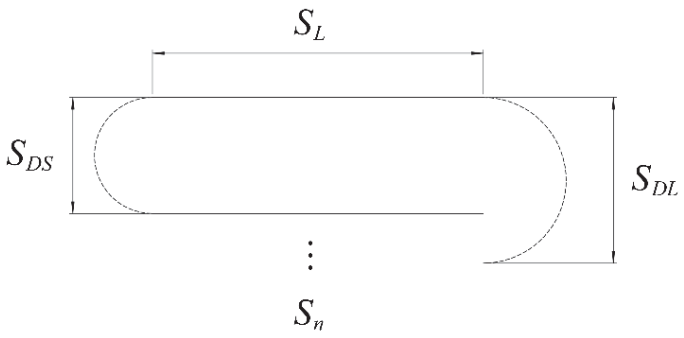

SOURCE: The author (2023).

The L_r term is found by calculating the ratio between strained fiber and unstrained fiber in the principal direction of measurement, as

$$\frac{1}{L_r} = \sum_{n=1}^{S_n} \frac{S_L}{S_L + \frac{\pi}{2}\left(S_{DS} + S_{DL}\right)}, \tag{57}$$

where S_n are the number of coils, S_L is the length of the straight strained fiber part, S_{DL} and S_{DS} are the free fiber curved regions. In cases where the serpentine length occupies a portion lesser than the sensing length, and the remaining fiber is at rest, the total L_r term becomes smaller considering the remaining unstrained fiber. In the opposite case, when the serpentine arrangement encompasses a whole sensing length unit or more, the resulting L_r term is given by the integral of the sum of parts within the sensing length limits. This method of describing the sensing ratio of the arrangement, as demonstrated in this section, is used as means to calibrate and compare between optical fiber installations.

4.1.2 Signal Processing and Model Updating

The photo-elastic mathematical model developed is analysed experimentally and using FEM software (Ansys). The solution of a optical fiber dynamic problem is acquired using transient, modal and harmonic analyses to determine the expected longitudinal strain of the fiber. The models developed are calibrated using accelerometer results obtained during structural identification experiments. The calibration is carried out by an optimization problem

that minimizes the error between FRF obtained numerically and experimentally, while the parameters of the structure, density and elasticity in particular, are problem variables. The optimization problem, P, is described as

$$E_{FRF} = \sum_{i=1}^{n'} \left\| H^{FEA}(\omega_i) - H^{Exp}(\omega_i) \right\|^2 \tag{58}$$

$$P: \begin{cases} \text{Minimize}: & E_{FRF} \\ \text{Constraint}: & \rho, E \geq 0, \rho \leq 1.2\rho_0, E \leq 1.2E_0, \end{cases} \tag{59}$$

where ρ_0 and E_0 are the reference density and Young's modulus of the materail, respectively, n' is the number of frequency sampled points, H^{FEA} is the FRF obtained via FEM, H^{Exp} is the FRF obtained in the experiment and E_{FRF} is the error. The solution of the problem is obtained iteratively using a simple grid search method. This process is shown in FIGURE 41.

FIGURE 41 – MODEL UPDATING ALGORITHM

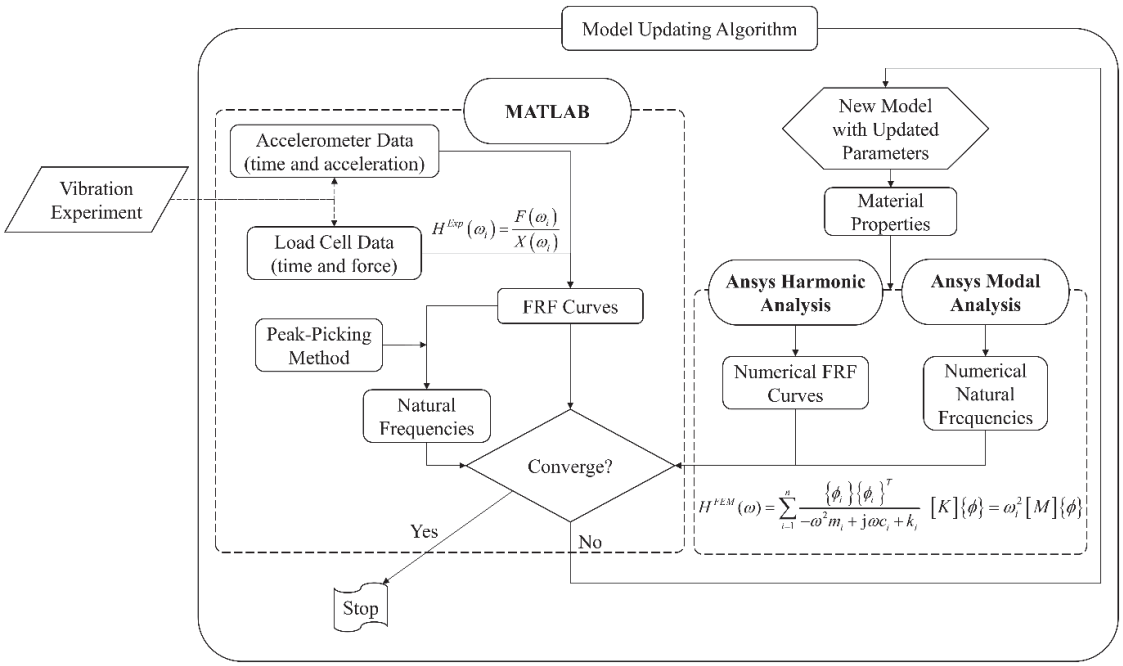

SOURCE: The author (2023).

The calibrated Finite Element (FE) model of the structure provides a way to determine the SFRF of the experiment. Through the strain conversion equations described in Section 4.1.1 (Photo-elastic model) the expected signal measured by the DAS system can be determined in

the frequency domain or time domain. Several model updating techniques are present in the literature. However, the main motivation of this thesis is related to the sensing technique rather than the FE model. Thus, considering the simplicity of the structures analysed, a simple method of model updating is used as described in this section.

The FEM nodal deformation result is analysed using a path function which selects the nodes that comprise the optical fiber arrangement. The strain tensor for each simulated load state is exported by Ansys© using an APDL© command line at the post-processing stage of the solution into MATLAB©, where the comparisons between simulation and experiments are carried out. The arrangement factor calibrates the experimental result and through post-processing techniques, such as PSD average, transfer function estimation and SRN evaluation, the DAS experimental results and FEM results are compared. This process is shown in FIGURE 42.

FIGURE 42 – PROCESS FLOWCHART OF PHOTO-ELASTIC SIMULATION USING FEM.

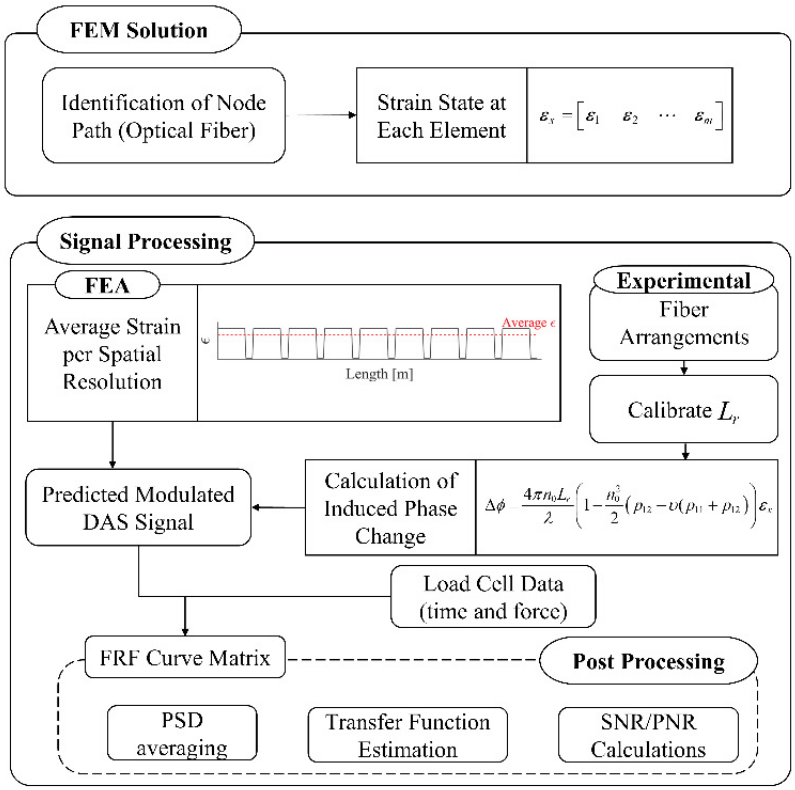

SOURCE: The author (2023).

4.2 FREE-FREE BEAM VIBRATION EXPERIMENT WITH OPTICAL FIBER IN SERPENTINE ARRANGEMENT

Most uses of DAS sensors are related to the monitoring of large structures as result of the spatial resolution limitations inherent to this technology. The spatial resolution indicates the minimum distinguishable spatial scale along the sensing fiber. In recent studies, the minimum pulse time can be as low as a few nanoseconds, which relates to a pulse that occupies less than one meter of optical fiber (WANG et al., 2020a). The resulting strain measurement is given by the average cumulative phase change within the fiber section occupied by the pulse (LIU et al., 2018). Thus, recent studies in SHM with DAS, for example, comprises of identifying vibration, wave propagation velocity and the use of statistical methods to develop indirect vibration information of large structures (LIEHR; MÜNZENBERGER; KREBBER, 2019; REN et al., 2016; WESTBROOK et al., 2020). Conversely, other distributed optical fiber sensors, such as those based on Optical Frequency Domain Reflectometry (OFDR), with a considerably lower sensing length, are able to detect material irregularities or perform SHM of relatively small structures due to the spatial resolution of a few millimeters (CHENG et al., 2017; CIMINELLO, 2019; FANG; SU; ANSARI, 2021; PELLONE et al., 2020). Several new DAS topologies and methods have been studied to improve spatial resolution, in a trade-off between cost, complexity, sampling rates and sensing length (CHEN; LIU; HE, 2019; CHEN et al., 2019; FENG et al., 2018; LU et al., 2017; MARTINS et al., 2016; WANG et al., 2020b).

This study refers to the paper published by the Institute of Electrical and Electronics Engineers (IEEE) Sensors Journal by the Author, which analyses the use of serpentine arrangements of optical fibers that enhances the quality of the acquired vibration data and enables monitoring of local dynamic strain using DAS. The methodology comprises of an arrangement procedure and signal processing that measures strain with higher sensibility enabling DAS to determine, among other vibration information, the frequency response of the structure and its modes of vibration. Experiments with a shaker, modal hammer and a free-free beam structure were carried out using accelerometers as reference sensors. A FE method model of the experiment was developed based on accelerometer data, and the strain results are compared with the results obtained using DAS in serpentine arrangements and a straight fiber optic configuration as a validation method.

4.2.1 Sensor Design and Arrangement

A serpentine method of arranging the optical fiber as a dynamic local strain sensors is proposed, as shown in FIGURE 43. The serpentine arrangement comprises of selecting a number of straight sections, called passes, and attaching these sections to the structure leaving the coiled parts free. The serpentine arrangements are tested for a selected width of 30 centimeters. The optical fibers arrangements are comprised of a single straight section of optical fiber of 30 centimeters, a two-coil optical fiber arrangement with 3 straight sections of 30 centimeters an eight-coil arrangement with 9 straight passes of 30 centimeter straight optical fiber sections. Also, a straight fiber along the centerline of the structure with a length of 2.7 meters was attached to the structure. The coupling was achieved using cyanoacrylate glue. The radius of the curvature of the serpentine arrangements surpassed the minimum of 3 centimeters determined by the maximum curvature without significant signal loss on the OTDR test (Corning SMF-28 fiber). A 10 meter buffer was used to separate each section of coupled fiber and facilitate the identification of the signal corresponding to each section.

FIGURE 43 – OPTICAL FIBER SERPENTINE ARRANGEMENT FOR BEAM VIBRATION EXPERIMENT.

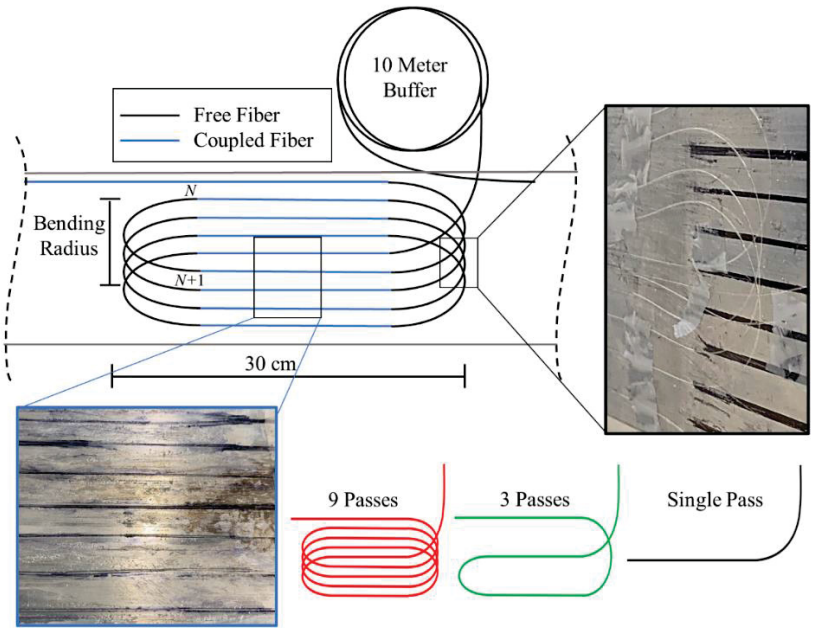

SOURCE: The author (2023).

The DAS sensor was developed following heterodyne based detection topology (PAN et al., 2011). In this topology, phase changes are digitally demodulated from the beat signal

between the backscattered light and local oscillator through IQ demodulation. A continuous wave narrow-linewidth laser source is first divided into two light pulses by a 99:1 optical coupler. 1% of the light is used as local oscillator (LO) to perform coherent detection, and the 99% remainder is launched to a polarization controller and pulse-shape modulated in an acoustic-optical modulator (AOM) with an upshift frequency of 200 MHz, which is controlled by a pulse generator board. The optical pulse is amplified in an erbium-doped fiber amplifier (EDFA) and launched to the FUT through an optical circulator. The backscattered light returned from the sensing fiber interferes with LO light at a 50:50 optical coupler. The resulting beat is transduced to an electric signal in a balanced photodetector, band-pass filtered, and acquired by a 14-bit 500 MS/s DAQ to be digitally processed.

4.2.2 Experimental Modal Analysis Setup

Vibration experiments were carried out to determine the performance of the arrangements in a simple structure. The experimental setup is demonstrated in FIGURE 44. A rectangular aluminum beam was selected with 5 mm width, 65 mm height and 2.7m length. The beam was hung using nylon strings and the boundary conditions are assumed to be free-free. Roving accelerometers from PCB® Piezotronics were installed using bee wax at 10 equidistant positions up to the vertical symmetry line of the beam, perpendicularly to the principal axis. The experiment utilized a Bruel and Kjaer shaker fitted with a PCB® load cell and a PCB® modal hammer for perpendicular dynamic excitations at a position 20 centimeters from the edge of the structure. The PHOTON+ data acquisition board from LDS DRACTON® was used to record the accelerometers and load cell data, while controlling the excitation of the shaker. The function used was a sine chirp from 1 to 250 Hz in 6.4 seconds and a sampling rate of 640 Hz for the shaker test, while the modal hammer test used a 9600Hz sampling rate.

FIGURE 44 – ALUMINIUM BEAM VIBRATION EXPERIMENT SETUP

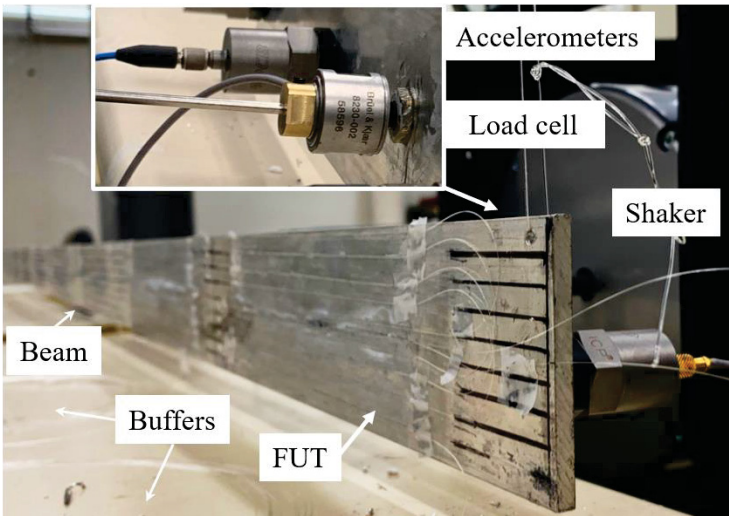

SOURCE: The author (2023).

The beam is divided into 9 sections of 30 centimeters where the three serpentine bare fiber arrangements were installed, as shown in FIGURE 45. A straight-line arrangement of the bare optical fiber was also installed across the whole center-line length of the structure. The shaker excitation was performed 25 times in succession and the hammer test was performed 16 times.

FIGURE 45 – DIAGRAM OF COMPLETE OPTICAL FIBER ARRENGEMENT IN ALUMINIUM BEAM EXPERIMENT

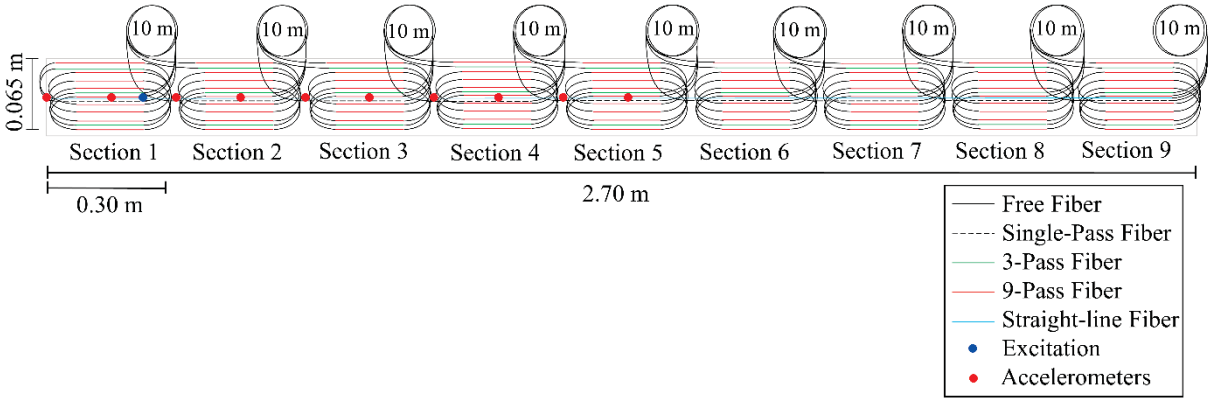

SOURCE: The author (2023).

The results of the accelerometers, load cells and fiber arrangements were measured simultaneously for each vibration excitation on the beam, as shown in FIGURE 46.

FIGURE 46 – SIMULTANEOUS MEASUREMENTS OF VIBRATION EXPERIMENTS

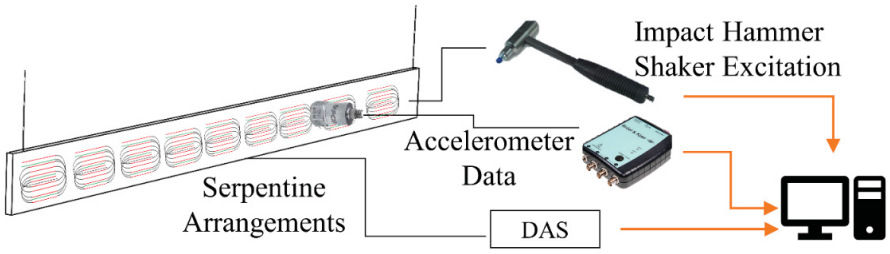

SOURCE: The author (2023).

A finite element numerical simulation of the experiment was developed to analyze the strain vibration response of the structure and compare to the results obtained using the DAS system. The accelerometers results acquired in the modal experiment were used to update the FEM model by changing structure parameters such as material density and Young's modulus. The simulation was developed using Ansys© software where a modal analysis and a harmonic analysis were selected. A convergence test was also carried out to verify possible changes in the results due to the mesh effects. FIGURE 47 illustrates the mesh used for the study, comprised of 282,071 nodes and 56,160 elements.

FIGURE 47 – FINITE ELEMENT MESH OF ALUMINIUM BEAM STRUCTURE

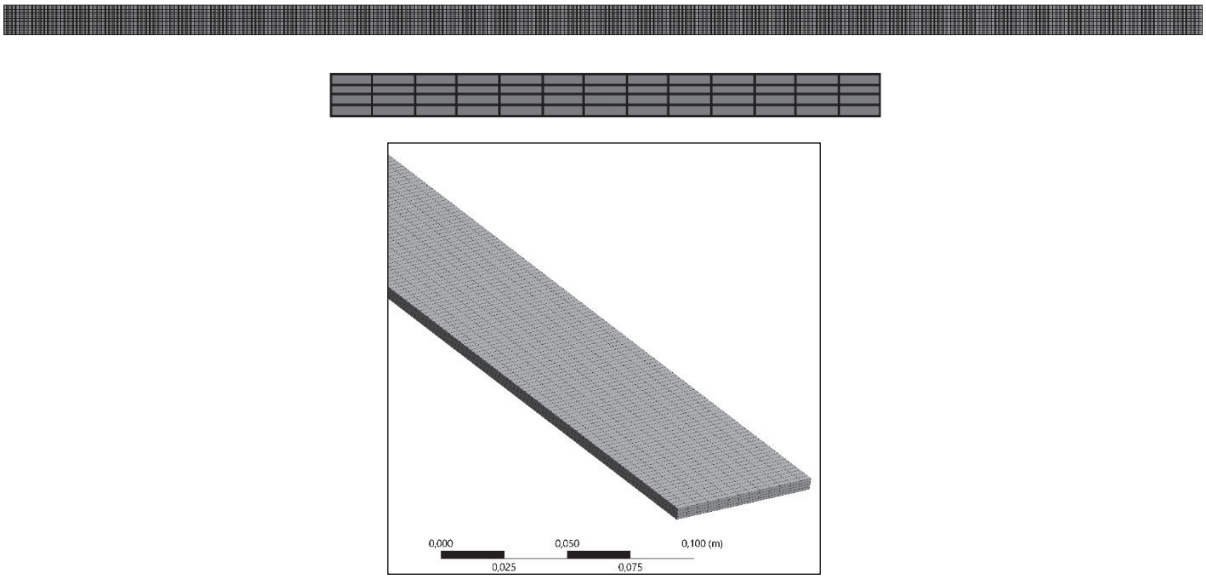

SOURCE: The author (2023).

4.2.3 Digital Processing of DAS

Signal processing techniques are applied to reconstruct the differential phase signal into dynamic strain data. In order to reduce amplitude fluctuation in the Rayleigh scattered signal due to random polarization phenomena, thermal fluctuation noise or even electrical noise, the moving average method was employed as an initial processing technique. Digital bandpass filters were applied along the temporal and spatial dimensions of the time domain signal, where lower and higher limit frequencies have been specified to reduce DC components and aliasing phenomena, respectively. The highest frequency is defined based on the Nyquist theorem, resulting in a sampling frequency of 500 MS/s in the spatial dimension. FIGURE 48 shows an example of differential phase data acquired by DAS for the 9 passes serpentine arrangement during a hammer test. Black dashed lines highlight each serpentine section along the structure. In this case the data is shown at a window of time starting before the trigger to demonstrate the contrast of the backscattered signal before and after the vibration experiment commences.

FIGURE 48 – A) DAS PHASE-DIFFERENTIAL SIGNAL IN THE TIME DOMAIN ACQUIRED DURING MODAL TESTING FOR A SINGLE ARRANGEMENT AND B) THE FREQUENCY RESPONSE SPECTRUM OF THE SIGNAL.

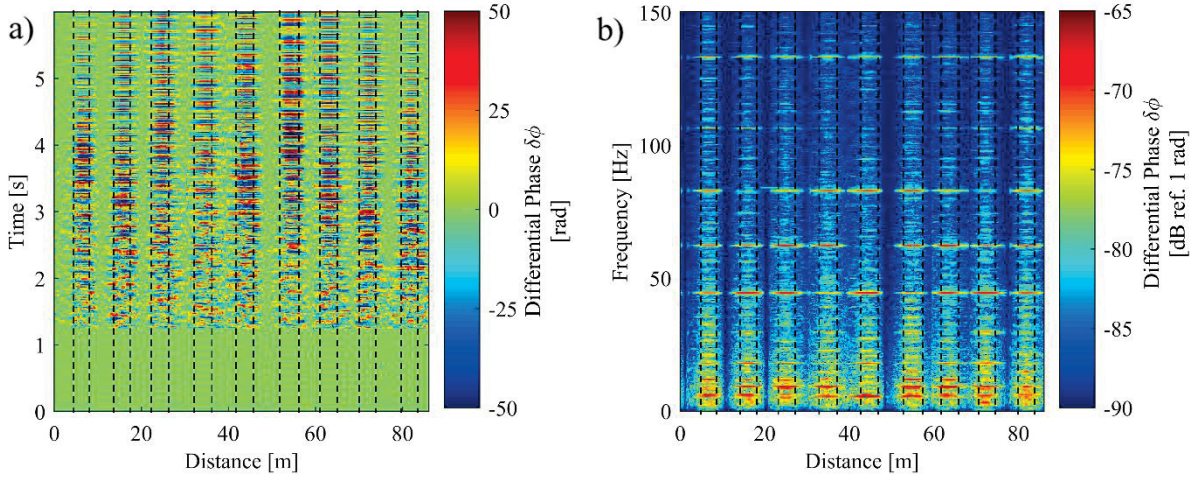

SOURCE: The author (2023).

The pulse width parameter of DAS system was set to 30 ns leading to a spatial resolution of approximately 3 meters. The gauge length was initially set to 1.5 times the pulse width (approximately 5 meters). The acquisition rate of DAS was set to 10kHz and a 6.4 second acquisition time was used.

After time domain signal processing, the power spectral density (PSD) S_{xx} of each region was calculated through the Fourier transform of the autocorrelation function $r_{xx}[k]$ of the pure time domain DAS signal, for N experiments, as

$$S_{xx}(\omega) = \frac{1}{N}\sum_{n=1}^{N}\sum_{k=-\infty}^{\infty} r_{xx}[k]e^{-i\omega k}, \qquad S_{xx} = \frac{1}{N}\sum_{n=1}^{N}\frac{|X_{trace}|^2}{N_f}. \tag{60}$$

The calculation of PSD follows the Wiener-Khinchin theorem based on the assumption that the measurements compose a random wide-sense stationary signal. The SFRF was obtained by using the H_1 estimator, by calculating the cross power spectral density of the DAS signal (output) and shaker excitation force signal (input).

4.3 ANECHOIC CHAMBER FOR ACOUSTIC EXPERIMENTS WITH OPTICAL FIBERS

In this thesis, acoustic experiments with the optical fibers are proposed with the objective to analyze the performance of the sensor as an acoustic sensor, the developed optoelastic mathematical model and compare to numerical FEM simulation. Thus, the author designed and constructed an anechoic chamber for acoustic experiments with optical fibers with funding from Petrobras.

An anechoic chamber is an enclosed space that represents a free field environment without sources of interfering noise. The internal walls are designed to absorb reflections of acoustic waves and be isolated from external noise sources. In general, the internal walls are furnished with absorbing material and the external wall is made of high-density material with vibration isolation properties. In Vierbrock e Crocker (1974), the design of an effective small anechoic chamber with cubic format is illustrated, as shown in FIGURE 49.

FIGURE 49 – TRANSPORTABLE ANECHOIC CHAMBER DESIGN.

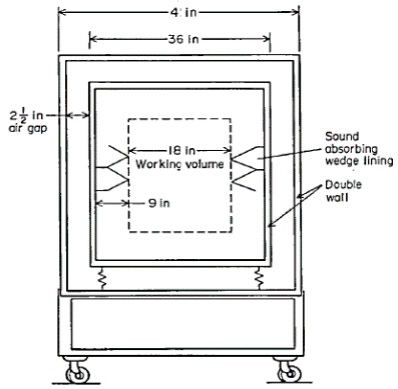

SOURCE: Vierbrock and Crocker (1974)

The designed frequency cutoff of the chamber is 270 Hz. A double wall is responsible for external noise isolation and a spring suspension system reduces transmissibility of vibrations from the floor into the chamber. Russo et al. (2018) proposes an effective anechoic chamber with rectangular parallelepiped format and dimensions of 2.8 meters x 1.7 meters x 2.05 meters. Here, the author proposed the construction of a transportable anechoic chamber with a rectangular parallelepiped format. The dimensions chosen were 2.67 meters by 1.87 meters by 1.65 meters based on the cutoff frequency for a far-field acoustic signal, given by (SUSHIL; GARG; NARAYANAN, 2020)

$$f_{cutoff} = \frac{2.25c}{(d - l_w)}, \tag{61}$$

where c is the speed of sound in the air, d is the principal experiment dimension of the anechoic chamber, in this case 2.67 meters, and l_w is the length of the anechoic wedges. Thus, a $f_{cutoff} = 306.25$ Hz is found for the constructed anechoic chamber. The Computer Aided Design (CAD) and final construction is shown in FIGURE 50.

FIGURE 50 – ANECHOIC CHAMBER DESIGN

SOURCE: The author (2023).

FIGURE 51 – ANECHOIC CHAMBER'S FINAL CONSTRUCTION.

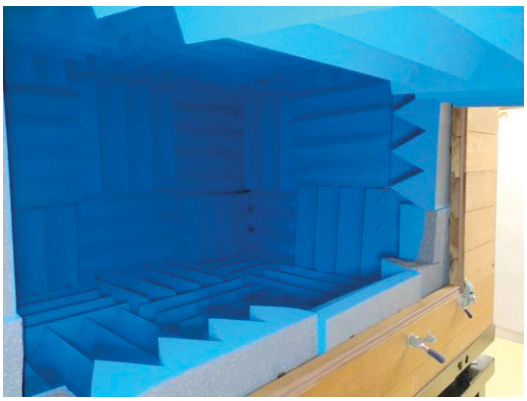

SOURCE: The author (2023).

The anechoic chamber was fitted in all internal surfaces with 15 cm height anechoic wedges with Noise Reduction Coefficients (NRC) described in TABLE 4.

TABLE 4 – ACOUSTIC PERFORMANCE OF ABSORPTION WEDGES AND NOISE REDUCTION COEFFICIENT (NRC)

Frequency (Hz)						
125	250	500	1000	2000	4000	NRC
0,87	1,35	1,55	1,57	1,48	1,68	1,49

SOURCE: The author (2023).

The design of a vibration isolation suspension with a cutoff frequency of 8.67 Hz and 95% isolation frequency of 28.11 Hz was developed by considering a damped spring-mass systems subjected to base excitation as shown in FIGURE 52.

FIGURE 52 – TRANSMISSIBILITY DAMPED SPRING-MASS SYSTEM

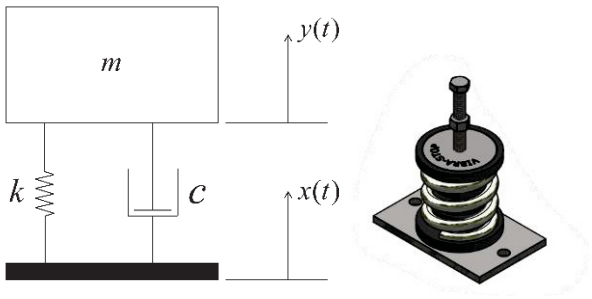

SOURCE: The author (2023).

The corresponding transmissibility of the system is found using the mass calculated using CAD software of approximately 1236kg for the wooden part of the chamber. The damping ratio and stiffness of the springs attached to the chamber are found from the commercial catalog of the dampers. The transmissibility of the dynamic system is described as

$$T(\omega)=\sqrt{\frac{1+\left[2\psi\left(\frac{\omega}{\omega_n}\right)\right]^2}{\left[1-\left(\frac{\omega}{\omega_n}\right)^2\right]^2+\left[2\psi\left(\frac{\omega}{\omega_n}\right)\right]^2}}, \tag{62}$$

where ψ described the damping coefficient of the suspension mechanism. The calculated transmissibility function of the vibration damper is shown in FIGURE 53.

FIGURE 53 – TRANSMISSIBILITY OF ANECHOIC CHAMBER AND FLOOR.

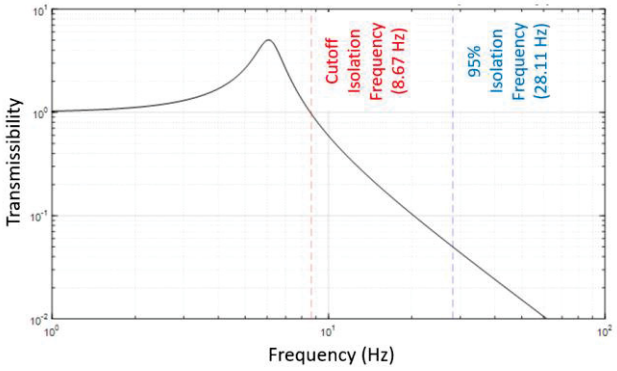

SOURCE: The author (2023).

4.3.1 Validation of Anechoic Chamber

A process of validation of the anechoic chamber was carried out to determine the free-field behavior of the space based on the *International Organization for Standardization (ISO) 26101: Acoustics – Test methods for the qualification of free-field environments*. The divergence loss method characterizes the test environment by quantifying the contributions of both direct and reflected components of acoustic energy. TABLE 5 demonstrates the maximum allowable deviation of the SPL for each frequency band.

TABLE 5 – MAXIMUM ALLOWABLE DEVIATIONS OF MEASURED SOUND PRESSURE LEVEL (SPL) FROM ANALYTICAL VALUES USING THE INVERSE SQUARE LAW.

Type of test environment	**One-third-octave mid-band frequency (Hz)**	**Allowable deviations (dB)**
Anechoic	≤ 630	±1.5
	800 to 5000	±1.0
	≥ 6300	±1.5
Hemi-anechoic	≤ 630	±2.5
	800 to 5000	±2.0
	≥ 6300	±3.0

SOURCE: BSI ISO 2026:101 (2017).

Tests were carried out using discrete one-third-octave frequency excitations: 200 Hz, 250 Hz, 315 Hz, 400 Hz, 500 Hz, 630 Hz, 800 Hz and 1000 Hz. FIGURE 54 demonstrates the illustration of the tests and experimental setup. A roving microphone of initial distance of 0.60 meters from the source measured the SPL for each experiment with incremental distances of 0.15 meters. In accordance to the ISO 26101, at least 10 measurement points are required to characterize the free-field, however, as consequence of the installation method of the microphones, only 5 measurement points were measured.

FIGURE 54 – VALIDATION OF ANECHOIC CHAMBER.

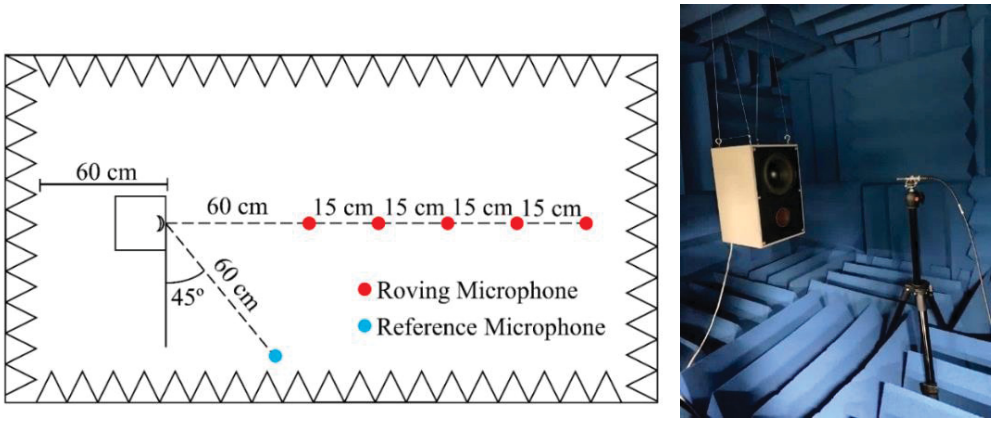

SOURCE: The author (2023).

The measured SPL at each position was compared to the ones obtained analytically using the Inverse Square Law (ISL). The reference microphone located at a fixed position at an angle of 45º and 0.60 meters from the source is used to calibrate the fluctuations of the source. The analytical ISL reference SPL is calculated using the following expression

$$L_p(r_i) = b - 20\log\left(\frac{r_i}{r_0}\right)\text{dB} \tag{63}$$

where $L_p(r_i)$ is the SPL at a distance r_i estimated by the inverse square law in dB, b is an adjustment parameter to fit the measured SPL into the tolerance range, r_i is the distance of the i-th measured point and r_0 is the reference distance value. The estimation of the deviation of the measured SPL from the ISL is determined by

$$\Delta L_{pi} = L_{pi} - L_p\left(r_i\right) + F(\delta_{uncert}) \tag{64}$$

where L_{pi} is the corrected SPL measured at a distance r_i from the source and δ_{uncert} are quantities allowed to account for any uncertainty related to the experiment. The reference microphone measured demonstrated a maximum radiated power instability from the source of [+1.15, -0.82 dB] for 200 Hz, [+0.77 dB, -0.38 dB] for 250 Hz, [+0.48, -0.33] for 315 Hz, [0.32 dB, -0.34 dB] for 400 Hz, [+1.13 dB, -0.66 dB] for 500 Hz, [+0.69 dB, -0.26 dB] for 630 Hz and [+1.18 dB, -0.62 dB] for 800 Hz, as demonstrated in FIGURE 55. Given the maximum

variation of the source stability, $\delta_{uncert} = 1.18\text{dB}$ is used for these experiments. The results of the validations experiments are demonstrated in FIGURE 56.

FIGURE 55 – SOUND SOURCE STABILITY USING REFERENCE MICROPHONE.

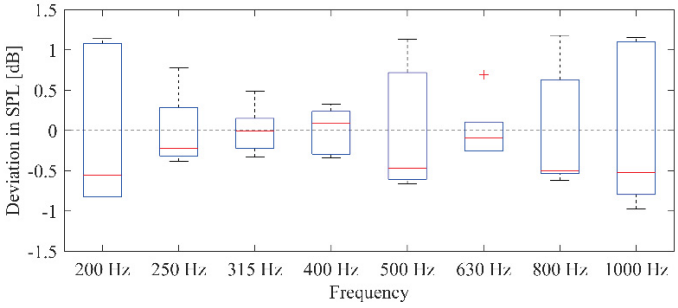

SOURCE: The author (2023).

FIGURE 56 – SPL MEASURED IN ANECHOIC CHAMBER EXPERIMENTAL VALIDATION

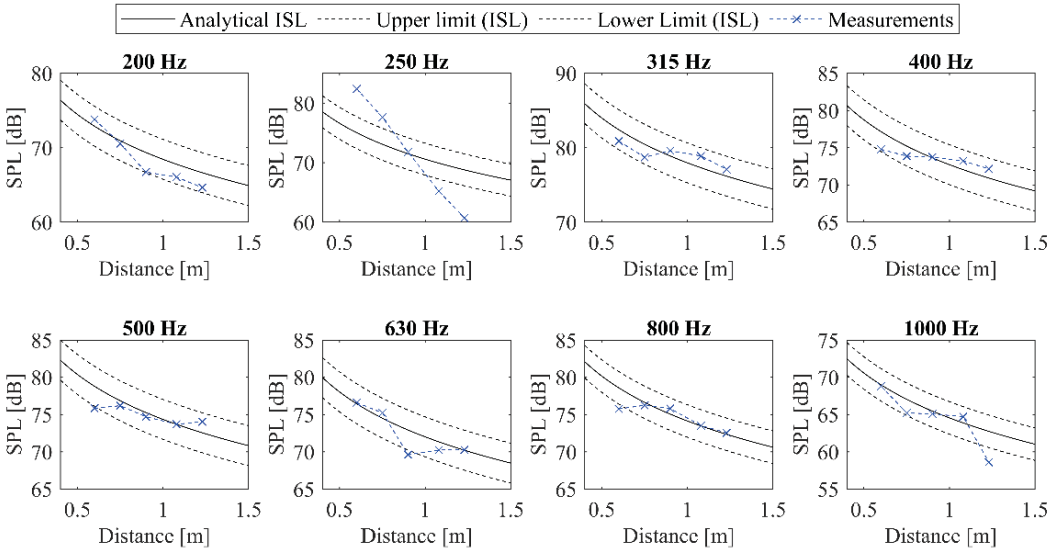

SOURCE: The author (2023).

The results calculated for the deviation from the reference SPL curve following the ISL equation are demonstrated in FIGURE 57. A high deviation from the ISL is found in frequencies below 250 Hz in accordance to the near-field calculations found using Eq. (61).

FIGURE 57 – SPL DEVIATION FROM THE ISL ANALYTICAL CURVE IN ANECHOIC CHAMBER EXPERIMENTAL RESULTS

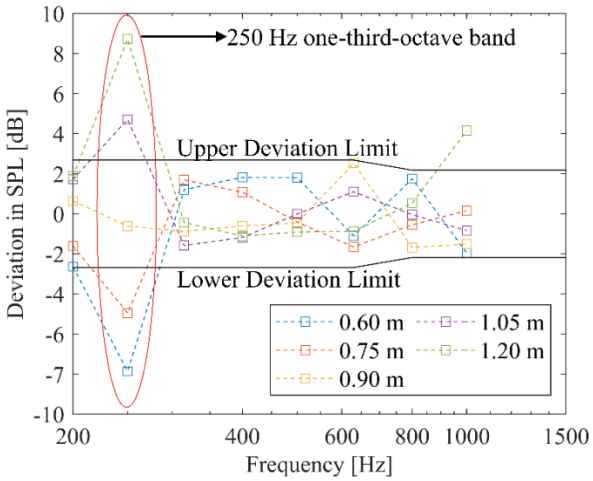

SOURCE: The author (2023).

Finally, FIGURE 58 demonstrates the noise amplitude spectrum inside the anechoic chamber as it was measured with external sounds occurring in the laboratory and surroundings and no acoustic excitation inside the anechoic chamber. The graph demonstrates a very sharp decline in measured signal after the 100 Hz region. At this point, the signal measured by the microphone might have reached the inherent microphone noise of 15.5 dB(A) ref. 20 µPa.

FIGURE 58 – SPL DEVIATION FROM THE ISL ANALYTICAL CURVE IN ANECHOIC CHAMBER EXPERIMENTAL RESULTS

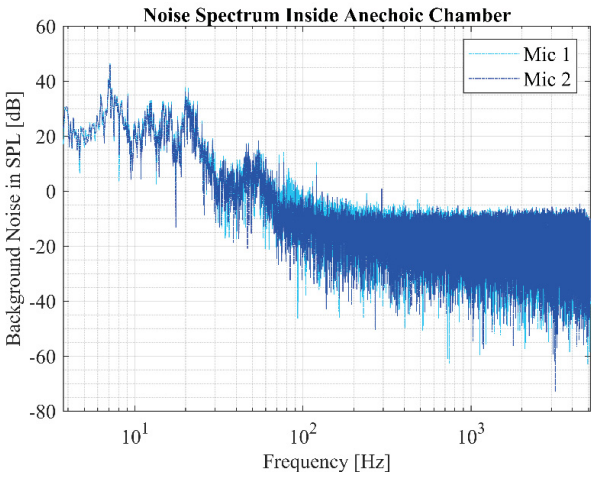

SOURCE: The author (2023).

A reverberation fade time of t_{rev} = [27 ms, 30 ms, 33 ms] was found for a 500 Hz pure tone signal (RT30). The test determines the time period necessary for the sound waves dissipate in

the acoustic isolation of the chamber walls. Comparing to the anechoic chamber from the University of Split, Croatia which satisfies both ISO 26101 and ISO 3745, the fade time at 500 Hz was approximately 42 ms (RUSSO et al., 2018). Thus, considering that a conventional speaker was used as an acoustic source since an omnidirectional sound source was not available commercially for this chamber size, the results demonstrate that the chamber experiments satisfy the free-field environment requirements for frequencies between 315 Hz and 1000 Hz.

4.4 IDENTIFICATION OF ACOUSTIC-INDUCED VIBRATION IN PLATES USING DAS

Although many studies in the field of DAS are concerned with improving acoustic performance, most studies in the literature comprise of employing fiber optical cables attached to lengthy structures such as railways, highways and/or buried cables to attain acoustic wave propagation information. This study analyses the use DAS with optical fibers as vibrations sensors for a thin plate structure, representing a small device, using an acoustic excitation. In certain applications, disadvantages of using impact hammers for vibration analysis exist associated with, for example, the required number of points of excitation or correct impact force, while using shakers can introduce mass loading. The characterization of structures using optical fibers acoustically can also allow the structure to act as an acoustic sensor and detect nearby acoustic events.

In this experiment, acoustic excitations were performed using a speaker at 1 meter distance to a 40 centimeter by 73 centimeter instrumented stainless steel plate inside an anechoic chamber, as demonstrated in FIGURE 59. The plate was hung using nylon strings and the boundary conditions are assumed to be free-free. Two reference microphones were used to determine the characteristics of the propagating wave and two accelerometers were installed at the plate back surface, whereas in the front surface of the plate Bending Loss Insensitive (BLI) optical fibers were arranged in a 15 coil serpentine using cyanoacrylate glue.

FIGURE 59 – ACOUSTIC EXPERIMENT CONFIGURATION IDENTIFICATION OF VIBRATION IN PLATE USING DAS: A) ARRANGEMENT OF OPTICAL FIBERS AND B) DIAGRAM OF EXPERIMENT

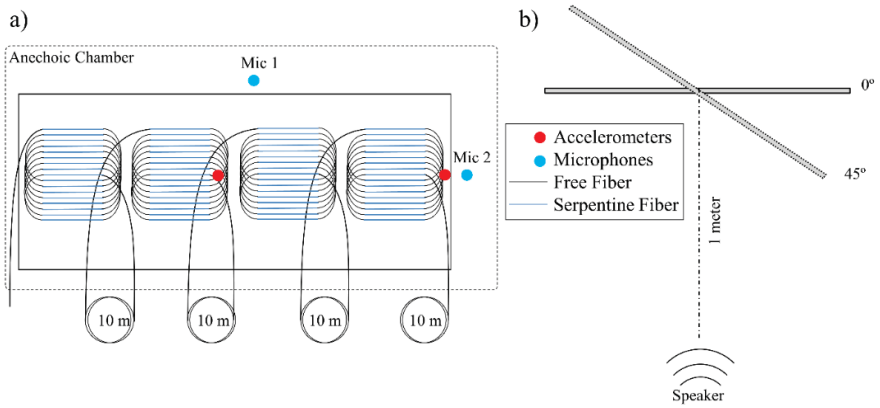

SOURCE: The author (2023).

Microphone 1, model PCB® 378B02 (FIGURE 61.c), and microphone 2, model PCB® 130F20 (FIGURE 61.d), are placed just above the centerline of the plate and at the side of the plate, respectively, as shown in FIGURE 59. An 8’ speaker diaphragm (FIGURE 61.a) is used as excitation source 1 meter away from the center of the plate. The microphoned signals and input signal to the speaker are managed by the signal processing device Photon+ by Bruel and Kjaer® (FIGURE 61.b). The experimental setup is shown in FIGURE 60.

FIGURE 60 – ACOUSTIC EXPERIMENT FOR ACOUSTICALLY INDUCED PLATE VIBRATION

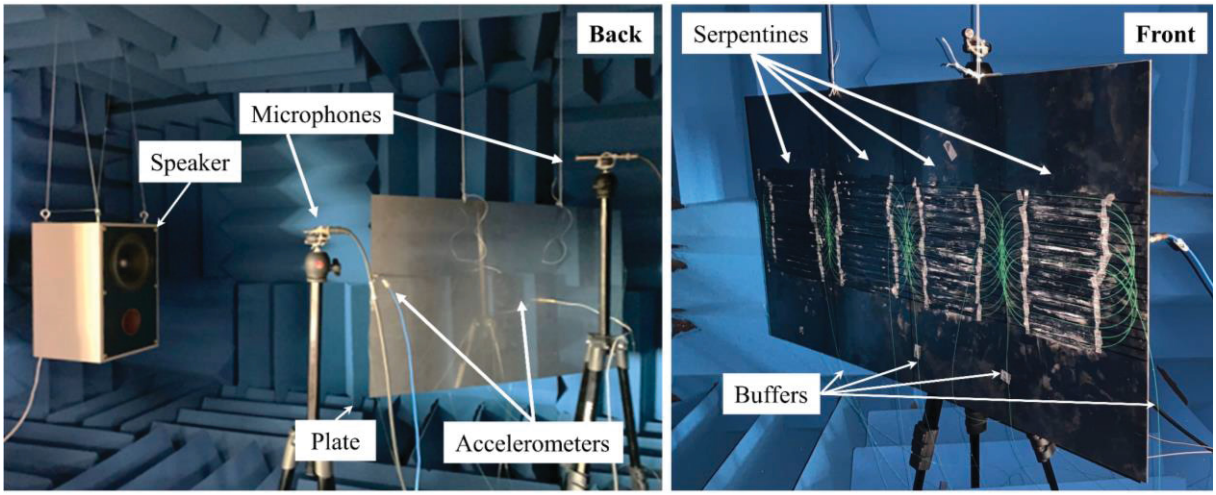

SOURCE: The author (2023).

The DAS sensor system was used with a 30 nanoseconds pulse, resulting in a spatial resolution of approximately 3 meters, and 10 kHz sampling rate. The input function to the excitation source used was a sine chirp from 5 Hz to 1000 Hz in 6.4 seconds and a sampling rate of 9600Hz was selected. The acoustic experiments were performed 5 times for each

different level of input voltage: 0.5 mV, 1 mV and 2 mV. Experiments were performed with the plate hung at 90º angle to the acoustic source and at 45º angle to the acoustic source.

FIGURE 61 – ACOUSTIC EQUIPMENT FOR EXPERIMENT: A) ACOUSTIC SOURCE; B) FUNCTION GENERATOR AND SIGNAL ANALYZER; C) MICROPHONE 1; D) MICROPHONE 2

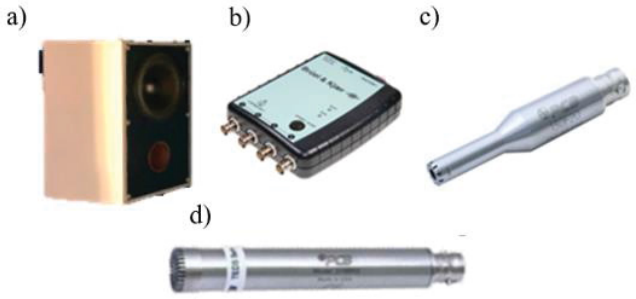

SOURCE: The author (2023).

The modal analysis and harmonic analysis of the FEM model was developed in Ansys software. The mesh comprised of 12,054 elements as demonstrated in FIGURE 62.

FIGURE 62 – MESH OF PLATE MODEL

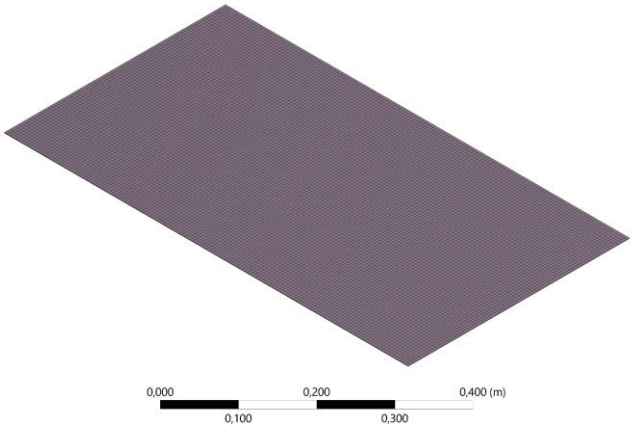

SOURCE: The author (2023).

5 RESULTS AND DISCUSSION

In this Chapter, the results and discussion of each experiment described in Chapter 4 are presented. Firstly, the free-free beam experimental results are demonstrated, beginning with the comparison between FEM updated model and accelerometer results. After that, the processing method of converting the vibration signal response is demonstrated, and the performance of four different optical fiber arrangements with 1, 3, 6 and 9 coils are compared. The PNR, gain and the reconstructed SFRF of each arrangement result is discussed. The same process is shown for the experiment of the free-free plate instrumented with a high-coil count serpentine arrangement under acoustic excitation.

5.1 FREE-FREE BEAM VIBRATION EXPERIMENT WITH OPTICAL FIBER IN SERPENTINE ARRENGEMENT

An updated FEM model was used to determine the modes and the expected numerical SFRF of the beam structure. The numerical displacement vibration modes up to 150 Hz of the structure in free-free boundary conditions are shown in FIGURE 63.

FIGURE 63 – NUMERICAL FLEXURAL MODES OF VIBRATION OF ALUMINIUM BEAM STRUCTURE

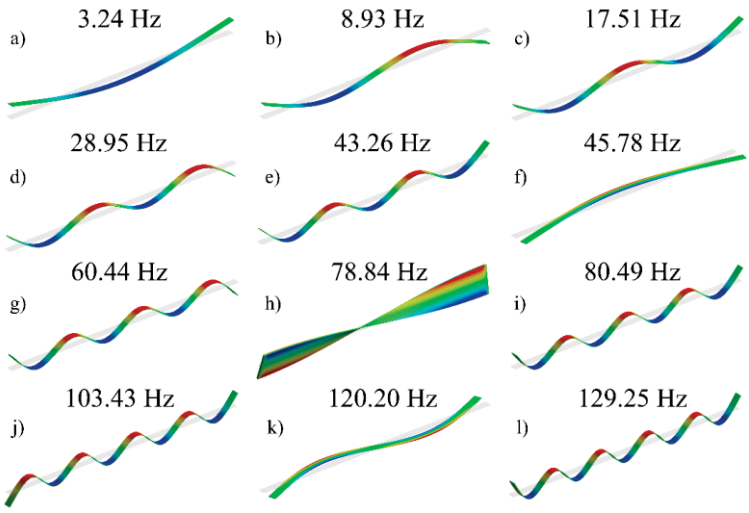

SOURCE: The author (2023)

Legend: a) - l): First twelve strain modes of vibration from numerical model.

The acceleration FRFs obtained at 10 equally spaced positions at the symmetry line of the left half of the beam are compared to the ones obtained with the updated numerical model in Fig.

8. A comparison between the longitudinal vibration data measured by DAS and transverse acceleration data from the accelerometers does not accurately represent the performance of each sensing system. Thus, the validated model was used to obtain the numerical SFRF and compare it to the results obtained using each DAS fiber arrangement. The inertance, *i.e.* acceleration FRF, is acquired using 30 FFT averages in the frequency domain and is compared to the calibrated numerical results in FIGURE 64.

FIGURE 64 – FEM MODEL CALIBRATION USING INERTANCE MEASURED BY ACCELEROMETERS FOR BEAM EXPERIMENT

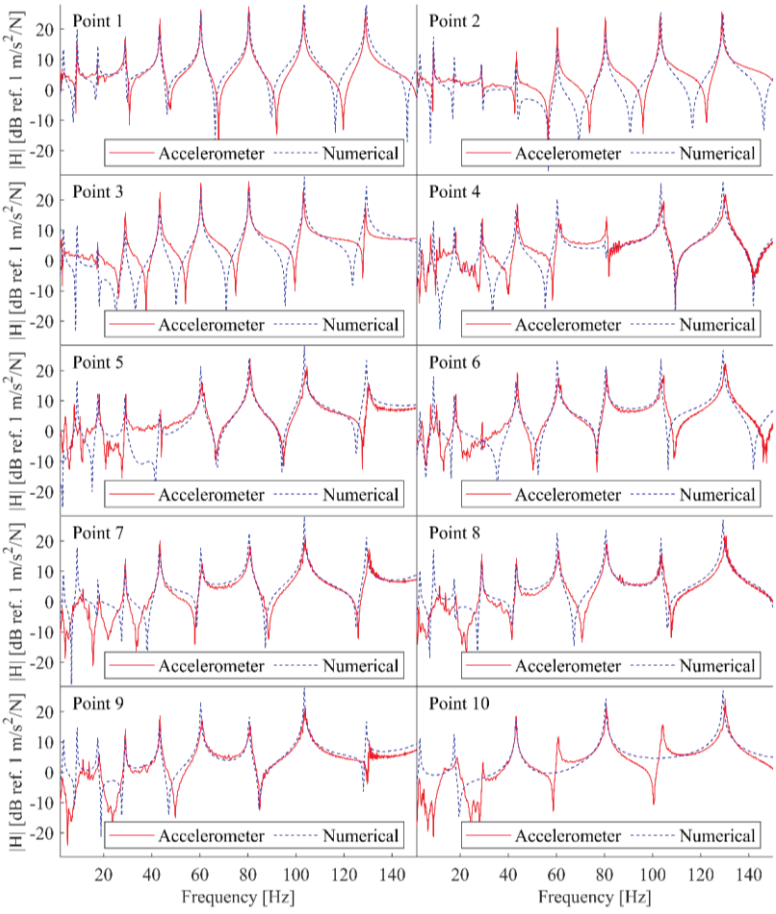

SOURCE: The author (2023).

The two sensor systems, accelerometers and DAS, acquired signals simultaneously. The DAS signal is acquired during the experiments, where a 10 meter buffer divides each of the tested arrangements. The buffers assist in visualizing and analyzing the resulting signals. FIGURE 65 shows the raw phase signal data of the experiment, demonstrating the total of 200 meters of optical fiber instrumentation in the beam divided into the 3 serpentine arrangements.

In the figure, the time of impact of the hammer experiment is demonstrated for a single experiment.

FIGURE 65 –TIME DOMAIN SIGNAL OF THE THREE ARRANGEMENTS USED OT INSTRUMENT THE BEAM MODAL EXPERIMENT: SINGLE PASS, 3 PASSES AND 9 PASSES SERPENTINES

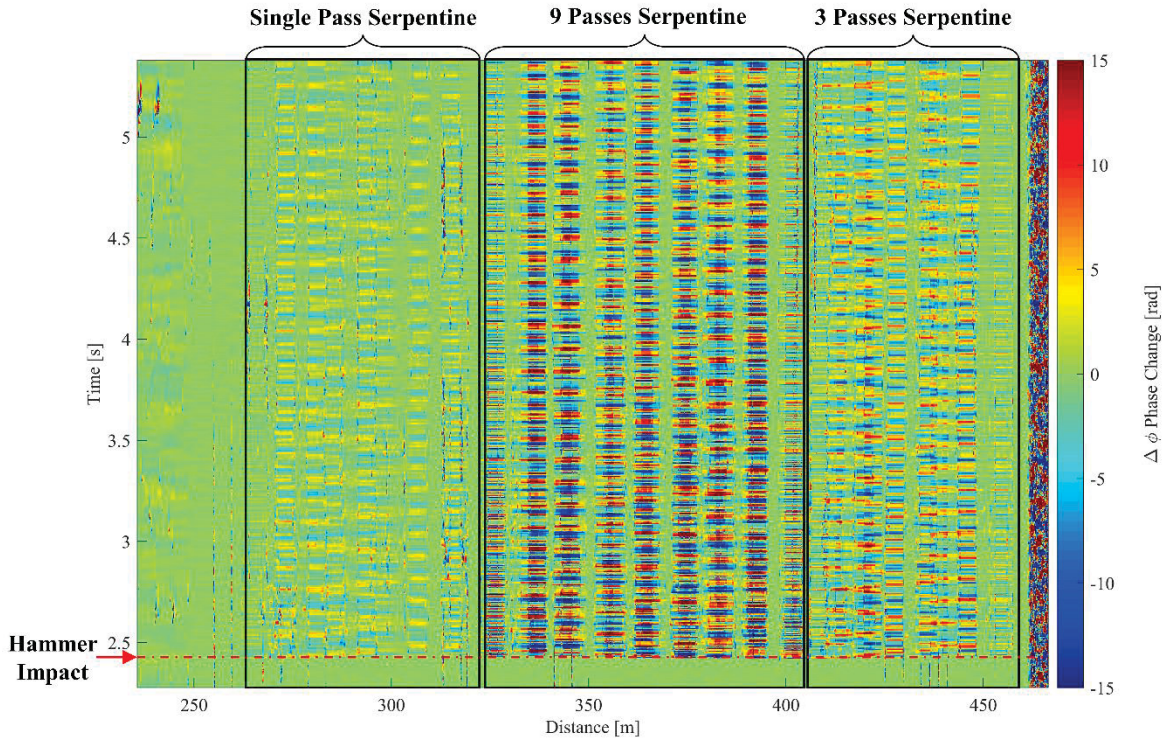

SOURCE: The author (2023).

The position of the serpentine sections installed in the beam for the 1 Pass, 3 Passes and 9 Passes arrangements are S_1 = [259.9m 270.7m 276.8m 284.2m 289.9m 295.6m 304.8m 310.1m 315.9m], S_3 = [404.7m 409.8m 415.4m 420.5m 425.8m 431.7m 437.4m 443.8m 449.7m], S_9 = [399.4m 390.2m 380.8m 372.0m 362.0m 353.0m 343.0m 333.2m 324.0m] and $S_{Straight}$ = [249.1m], respectively. The corresponding 9 Passes serpentine section divided by buffer separations of approximately 10 meters is shown in FIGURE 66. FIGURE 66.a illustrates the time domain signal and FIGURE 66.b illustrates the Short Time Fast Fourier Transform (STFFT) of the signal.

FIGURE 66 – A) TIME DOMAIN SIGNAL OF DAS SYSTEM; B) STFFT OF SIGNAL IN THE FREQUENCY DOMAIN

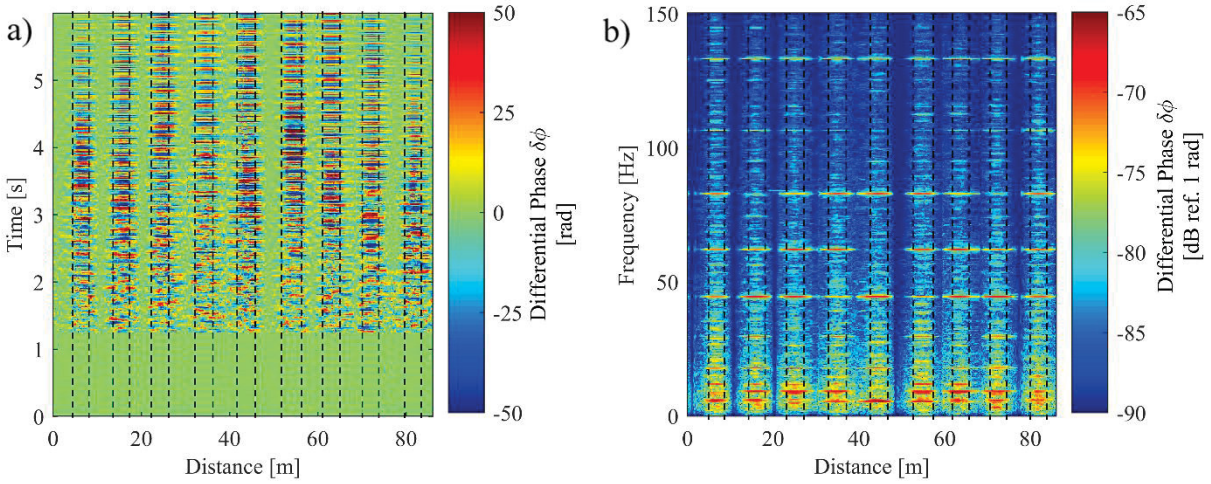

SOURCE: The author (2023).

Legend: a) DAS phase-differential signal in the time domain acquired during modal testing for a single arrangement and b) the frequency response spectrum of the signal.

The DAS signals acquired during the experiments used the same post-processing algorithm for every serpentine arrangement and for the straight-line fiber section. As a result of the high sampling rate of the DAQ (500Ms/s), phase change signals are acquired at positions around 20 centimeters apart along the optical fiber length. The signals measured in the vicinity of a 3 meters span are similar as consequence of the optical pulse width of 30 nanoseconds (~3 meters). FIGURE 67 shows the PSD response measured at each of the measurement points included in the 3 meters of fiber for the 9 beam sections instrumented by the 9-Passes serpentine arrangement and the straight optical fiber installation across the beam (section 10). The graph demonstrates that the straight optical fiber obtains noisier response compared to the 9 Pass sections due to the distribution of compressive and tensile strains along the optical fiber.

FIGURE 67 – PSD OF DAS SIGNALS ACQUIRED AT POINTS ALONG EACH SECTION OF THE BEAM

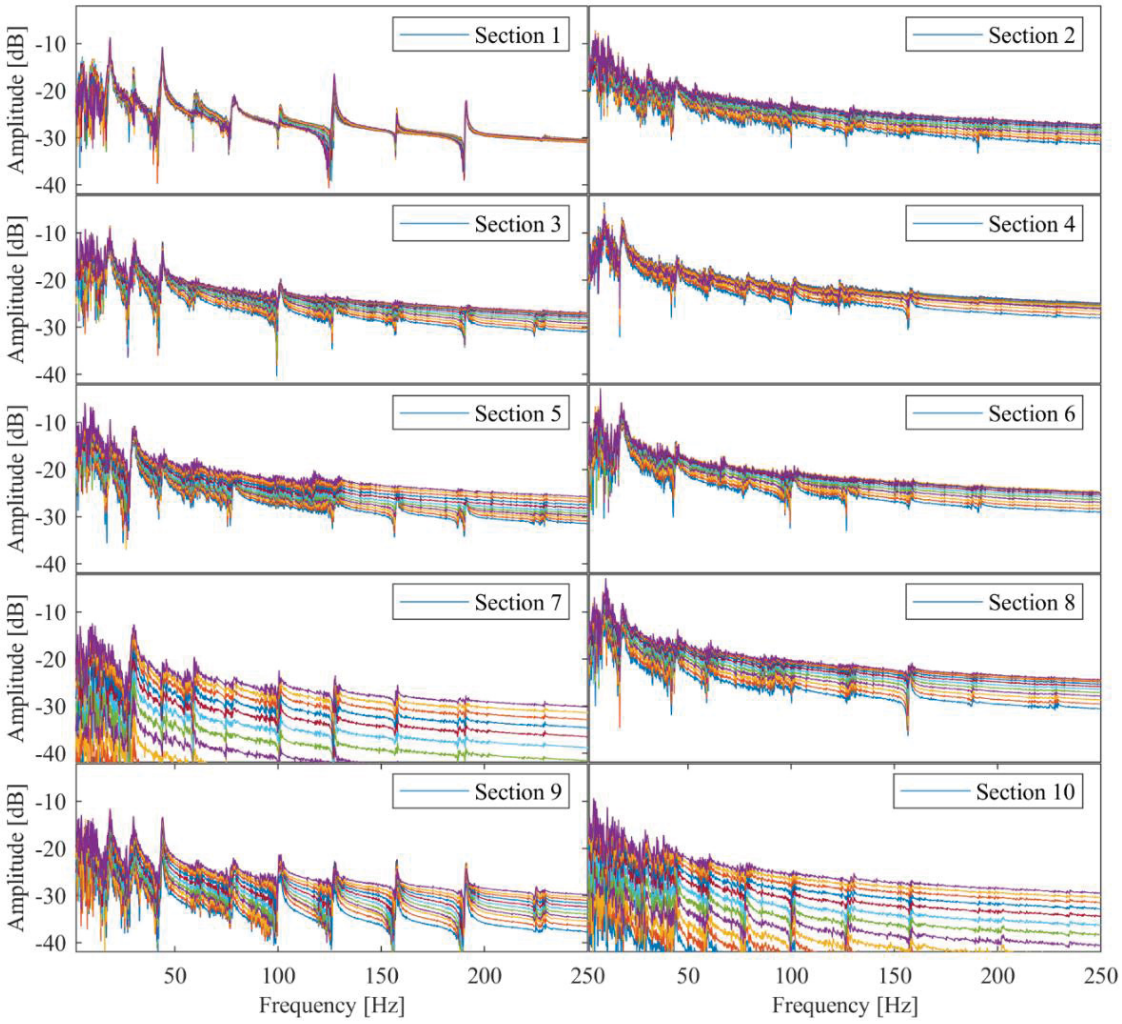

SOURCE: The author (2023).

The DAS signals are post-processed and the strain frequency response of each section is obtained using the input signal of the load cell of the shaker. The phase differential signals are averaged in the frequency domain to obtain a consolidated curve related to that spatial resolution. The Power Spectrum Density (PSD) responses of each serpentine arrangement are shown in FIGURE 68.(a) for a single hammer test of low impact force of approximately 1 Newton. The numerically identified resonant frequencies for the flexural modes are shown using vertical dashed lines. As the optical fibers are oriented longitudinally in the structure, the DAS sensor shows more sensitivity to the flexural modes of vibration. In FIGURE 68.(a), a higher number of longitudinal passes of the serpentine arrangement incurs in an increase of in-phase strained fiber within the spatial resolution demonstrating a gain in sensibility as emphasized in FIGURE 68.(b).

FIGURE 68 – AVERAGE PSD RESPONSE OF THE OPTICAL FIBER AT EACH SECTION OF THE BEAM

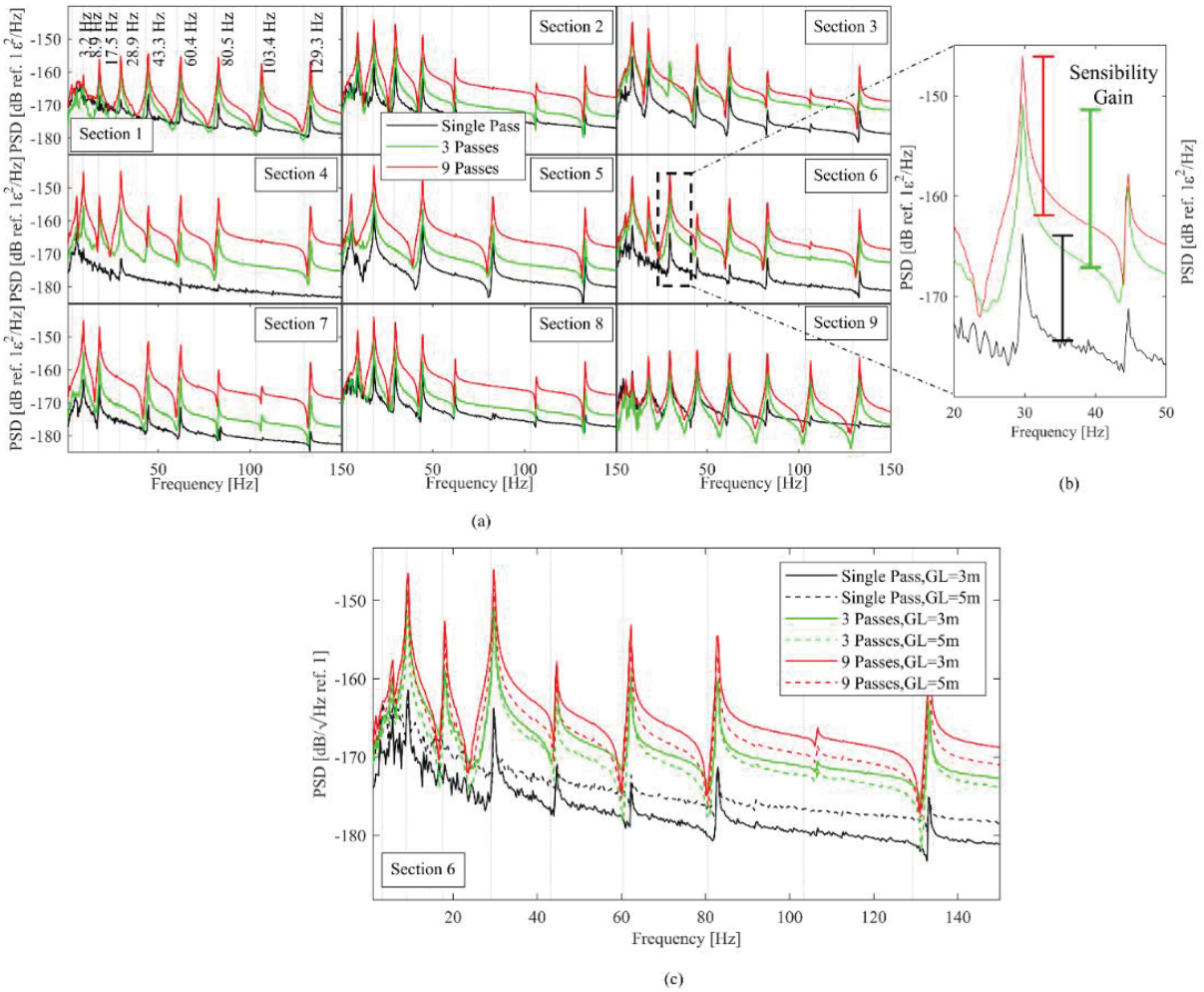

SOURCE: The author (2023).

The corresponding Peak-to-Noise Ratio (PNR) is calculated for each resonant frequency, defined by the ratio between the amplitude response at a resonant peak and noise floor at the vicinity of that frequency peak. A PNR lower than 1 indicates a non-identifiable (NI) resonance peak. In the case of this experiment, a signal power gain of approximately 12.9 dB and 17.7 dB are found for the 3-passes and 9-passes arrangement, respectively, when compared to the 1-pass optical fiber for the section 6 fourth mode response. An average 7.6 dB increase, from 6 dB to 13.6 dB, in the peak-to-noise ratio (PNR) is found when comparing the 3-pass to the 1-passes arrangement, while a 12.9 dB increase using the 9-passes arrangement is obtained. The sensibility of each arrangement can also be increased by changing the gauge length used to calculate the differential phase signal. FIGURE 68 (c) shows the results for the same test using a gauge length of 5 meters and 3 meters for each serpentine arrangement. As shown in FIGURE 68 (b), the increased sensibility due to gauge length changes does not lead to substantial improvements in the measured response of the tests. As the gauge length dictates the sensibility

of the complete measured data, both the signal of interest and noise can be amplified. The single pass fiber data obtained using 3 meter and 5 meter gauge lengths produced similar results in terms of PNR in this case. FIGURE 71 demonstrates the second, third, fourth and fifth numerical flexure modes of the beam and compares it to the normalized modes obtained using the 9 passes serpentine at the corresponding resonant frequency. The reconstructed modes are similar to those obtained numerically showing agreement between results. This is an advantage of the proposed optical fiber arrangements for vibration analysis.

FIGURE 69 – NORMALIZED STRAIN MODE SHAPES OF THE BEAM MEASURED BY DAS IN THE 9 PASSES SERPENTINE ARRANGEMENT AND NUMERICALLY

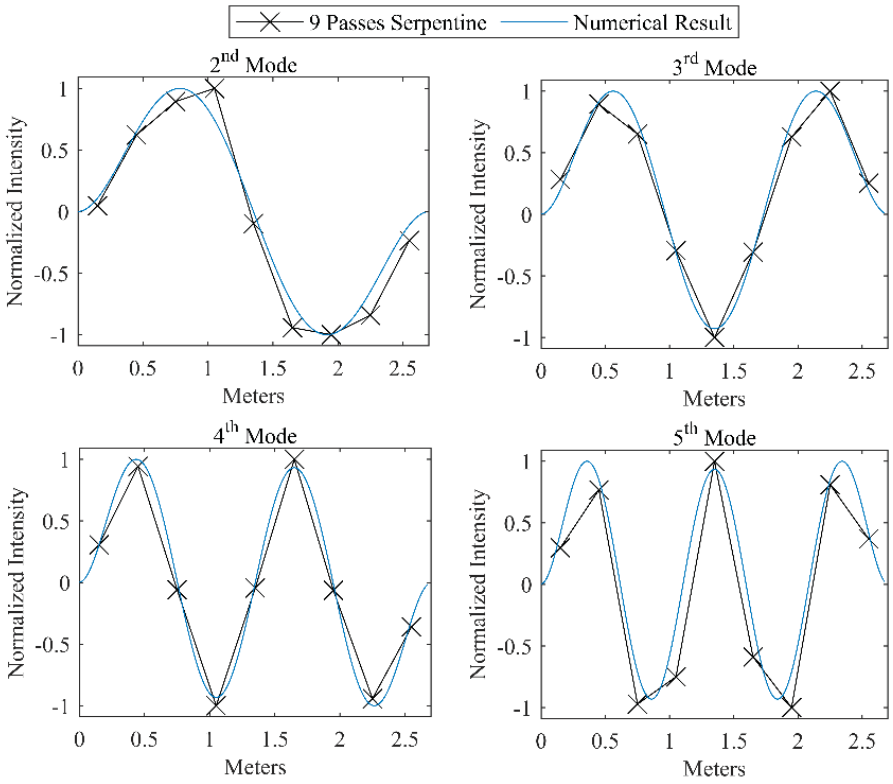

SOURCE: The author (2023).

FIGURE 70 demonstrates a comparison between PSD curves for a hammer test with a considerably higher impact force in comparison with the previous case. Here, the impact causes a level of deformation that saturates the reconstructed phase signal obtained using the 9 passes serpentine. The inability to process the phase unwrapping consistently leads to a signal with higher noise and distortion as observed in FIGURE 70, especially at lower frequencies as a result of higher strains at these frequencies.

FIGURE 70 – RESPONSE OF THE OPTICAL FIBER AT EACH SECTION OF THE BEAM

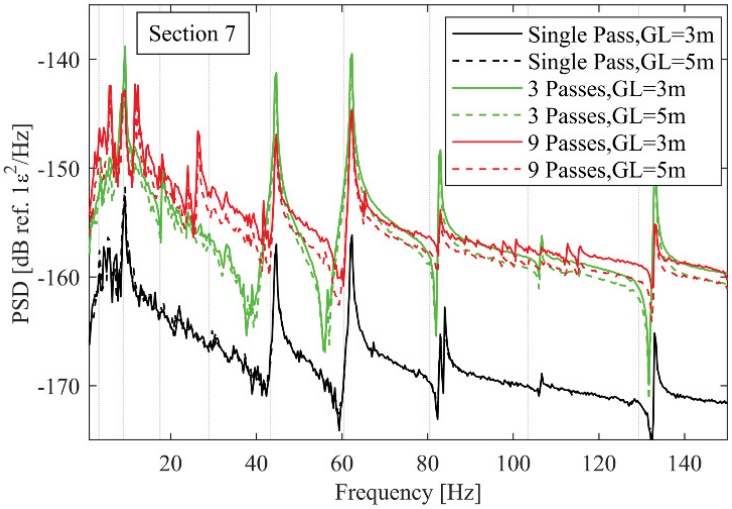

SOURCE: The author (2023).

The hammer tests were performed several times with ranging impact forces in a search for the measurement characteristics of each serpentine arrangement. FIGURE 71 demonstrates a measurement of the signal gain of each serpentine arrangement given by the value of the PSD peak amplitude at the fifth resonant frequency. In general, the serpentine with more coils demonstrates higher gain. However, for higher impact forces, the increase in gain halts due to issues with the unwrapping algorithm, reaching a saturation level of the sensor arrangement.

FIGURE 71 – PEAK SIGNAL VALUE ON THE FIFTH MODE RESONANT FREQUENCY AT MAXIMUM STRAIN POSITION FOR IMPACT HAMMER TESTS

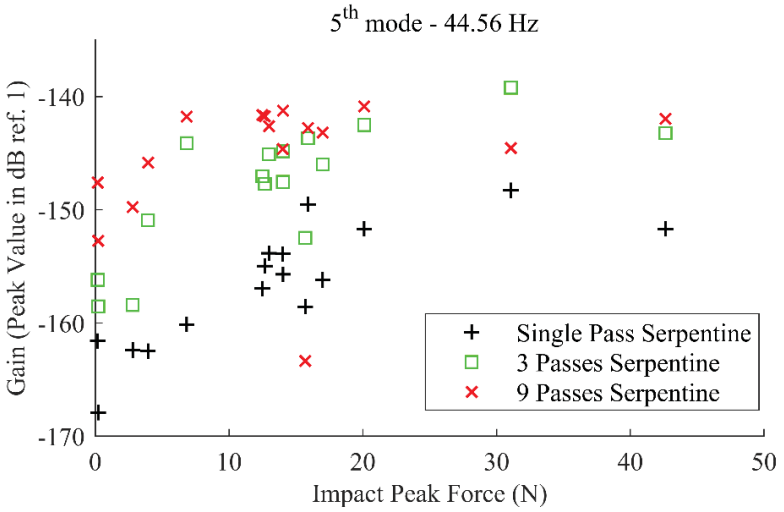

SOURCE: The author (2023).

A shaker experiment was carried out to determine the frequency response function (FRF) of the system. FIGURE 72 illustrates a comparison between the 9 passes serpentine arrangement response and a straight fiber arrangement spanning the whole beam length. The straight optical fiber section obtained a varying PSD due to the presence of a distribution of compressive and tensile strain regions at certain modal frequencies along the optical fiber resulting in a noisier signal. The serpentine optical fiber sections were mostly under in-phase deformation and obtained a frequency spectrum response with clearer peak protuberance. The noise peaks in the straight fiber section response and resonant peaks for the straight and serpentine sections responses are evidenced in the graph by purple, green and blue circles, respectively. Table 6 lists the natural frequencies identified by the 9 passes serpentine sensor system arrangement and the numerical results for the horizontal flexural modes (FH), vertical flexural modes (FV) and torsion vibration modes (T) up to 150 Hz for the shaker tests. The serpentine optical fiber arrangement obtained an adequate PNR for most structural resonant frequencies, specially at higher frequencies. A higher excitation force is present in the shaker tests causing larger strains in lower frequencies. The phase unwrapping algorithm has difficulties demodulating high strain values and noise can arise as a result. For this reason, lower PNR values are found for lower-order resonant frequencies for this experiment.

FIGURE 72 – COMPARISON BETWEEN THE AVERAGE PSD RESPONSE OBTAINED USING THE 9-PASSES SERPENTINE SECTIONS AND THE STRAIGHT-LINE FIBER

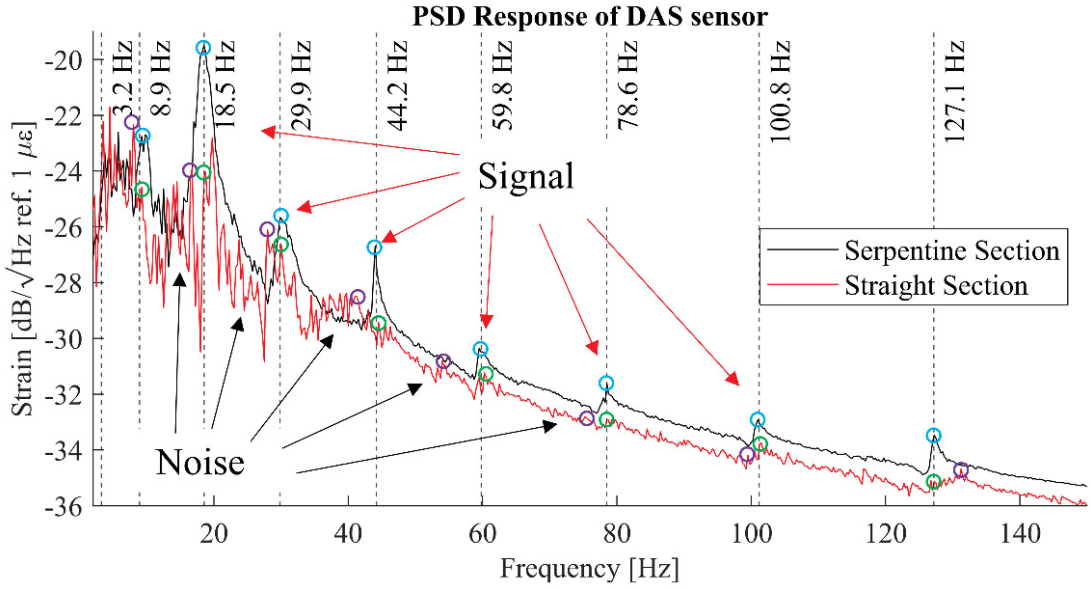

SOURCE: The author (2023).

TABLE 6 – IDENTIFICATION OF FLEXURAL NATURAL FREQUENCIES

Mode Freq.	FEA (Hz)	Accel. (Hz)	Serp. DAS (Hz)	9-Passes PNR (dB)
ω_1 (FH)	3.2	3.06	3.75	1.28
ω_2 (FH)	8.9	8.90	8.9	1.33
ω_3 (FH)	17.5	18.6	19.5	4.93
ω_4 (FH)	28.9	29.06	29.7	4.34
ω_5 (FH)	43.3	43.44	43.9	5.8
ω_6 (FV)	43.8	NI	NI	-
ω_7 (FH)	60.4	60.47	61.3	5.44
ω_8 (T)	78.2	NI	NI	-
ω_9 (FH)	80.5	80.31	82.1	4.37
ω_{10} (FH)	103.4	103.1	105.6	9.13
ω_{11} (FV)	120.2	NI	NI	-
ω_{12} (FH)	129.3	128.9	132.0	10.7

SOURCE: The author (2023).

5.1.1 Strain Frequency Response Function

The determination of the FRF of structures can be used for many purposes including fault detection and structural health monitoring. The quality of the FRF measured is associated with the ability of the sensor to identify changes in the structure. Two major sources of noise are present in DAS heterodyne detection, one related to the randomness attributed to the light interaction with the medium and the phase-unwrapping post-processing algorithm. In the following results, the capability of the sensor arrangement to measure the SFRF of the structure is demonstrated, without the requirement of advanced signal processing tools. The SFRF estimation used a rectangular time window without segmentation or overlap of the signal.

In FIGURE 75, a comparison between the calibrated SFRF obtained using DAS for each optical fiber arrangement and the FEA simulation result is demonstrated. The graph indicates that the calibration algorithm successfully corresponds to the ones obtained numerically with a small error between peak resonant amplitude.

FIGURE 73 – COMPARISON BETWEEN CALIBRATED SFRF OBTAINED OPTICAL FIBER ARRANGEMENTS WITH DAS AND FEA SIMULATION

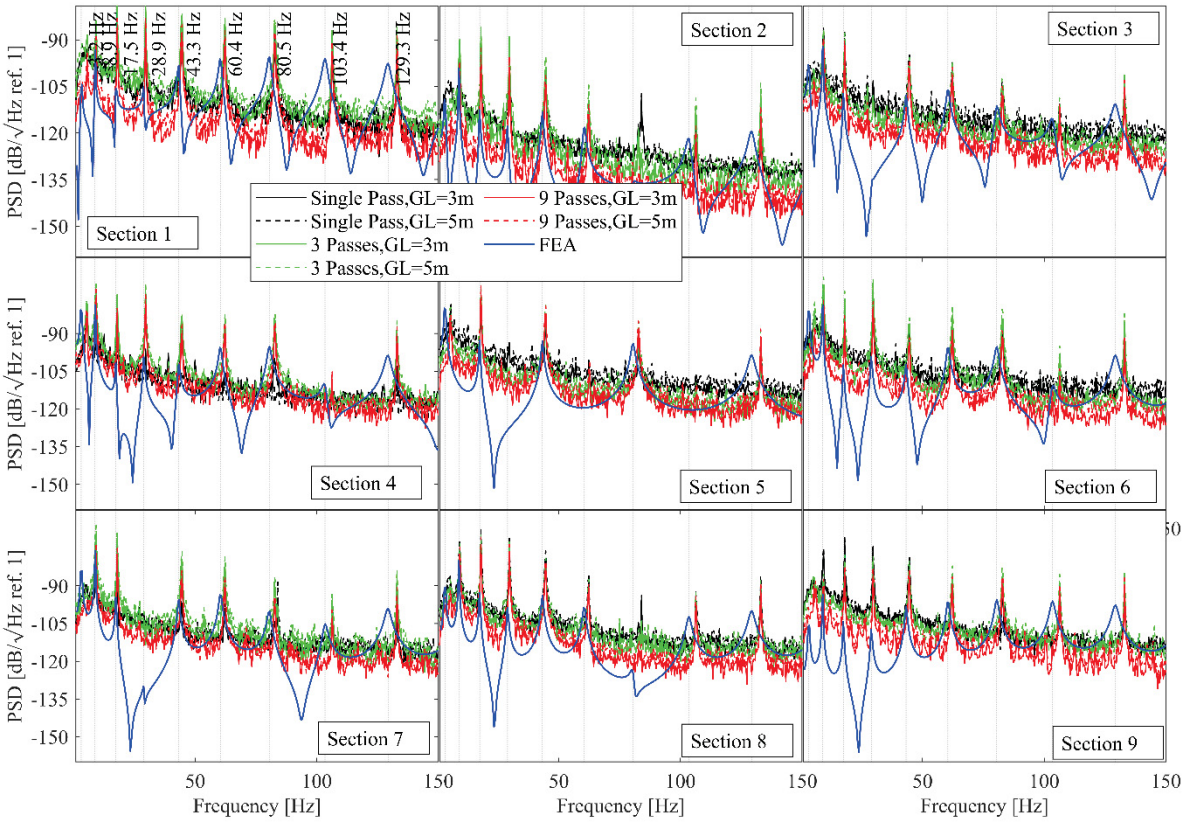

SOURCE: The author (2023).

Modal parameter identification in experimental modal analysis mathematically relates the dynamic excitation to the structure behavior. The presence of noise and non-linearities on the calculated FRFs can diminish the accuracy of the parameters obtained. A widely available algorithm of parameter identification, the Least-Squares Rational Function (LSRF) estimation, was applied to the data obtained using DAS in the proposed 9 passes serpentine arrangement configuration. The resulting parametric SFRF was compared to the numerically obtained SFRF solution using FEA, in FIGURE 74.

FIGURE 74 – PARAMETRIC SRFR CURVE BASED ON DAS RESULTS COMPARED TO NUMERICAL SFRF

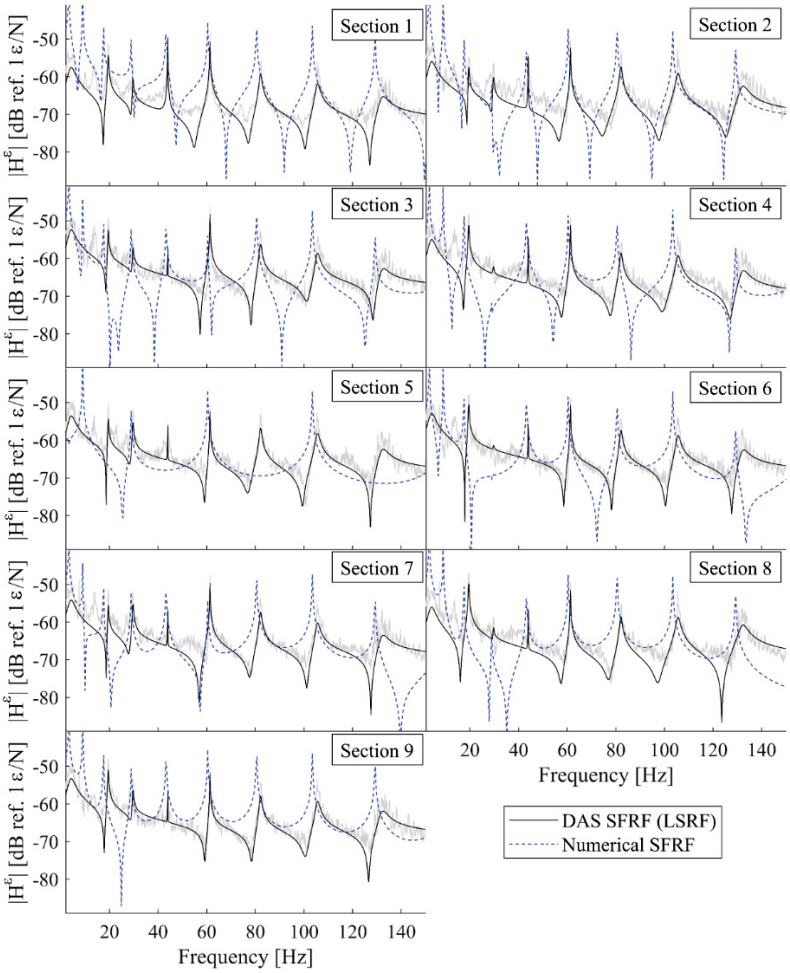

SOURCE: The author (2023).

The results show an overall agreement between the curves and peak location. Some peaks obtained using DAS presented lower amplitude due to high amplitude distortion, possibly caused by the unwrapping algorithm. Other sources of differences may include the added accelerometer masses, shaker coupling and numerical errors. In future works, the sensor installation arrangements will be tested in the identification of damage progression in structures.

5.2 ACOUSTIC INDUCED VIBRATION IN PLATE USING DAS

A FEM model of the 1 millimeter thick free-free 0.40 meters height by 0.73 meters width instrumented stainless steel plate was developed using Ansys© software. The model updating algorithm was used to calibrate the model using the response of the reference sensors, *i.e.* accelerometer and microphones. The calculated modes of vibration, considering total displacement are shown FIGURE 75.

FIGURE 75 – MODES OF VIBRATION OF STAINLESS STEEL PLATE

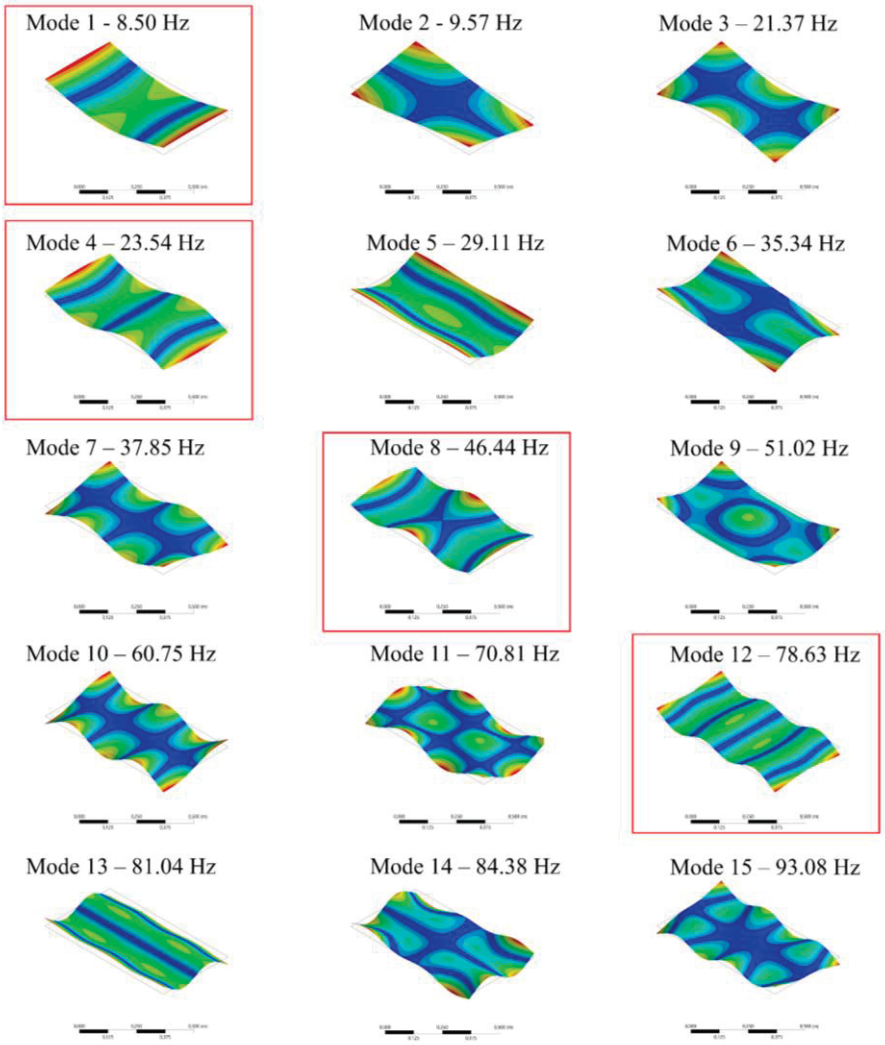

SOURCE: The author (2023).

The FEM modes were analyzed individually comparing to the SFRF peaks obtained using DAS. Some modes, such as the horizontal flexure modes and the horizontal axial modes, causes higher strain in the serpentine arrangements and a higher sensibility to those modes is expected using the arrangement. The high sensibility modes are emphasized by a red square in FIGURE 75. The measured SPL nearby the plate measured by the microphone for a given chirp acoustic excitation is shown in FIGURE 76 for the input signals with 0.5 Vpp, 1 Vpp and 2 Vpp intensities. An average gain in SPL from 0.5 Vpp to 1 Vpp of 5.51 dB is found, whereas a gain from 1 Vpp to 2 Vpp of 3.68 dB is found. An internal anti-resonance frequency of the speaker of approximately 539.7 Hz is demonstrated by the anti-peak in the graph. The high flexibility of the experimental plate resulted in a great quantity of vibration modes up to 500 Hz. Thus, the analysis was limited to 500 Hz. Even with the anechoic chamber showing free-

field behavior starting at 306.25 Hz (cutoff frequency), the analysis include frequencies below the cutoff since most of the high sensibility modes are located at low frequencies.

FIGURE 76 – SPEAKER FREQUENCY SPECTRUM SOUND POWER LEVEL NEAR PLATE FOR CHIRP EXPERIMENT

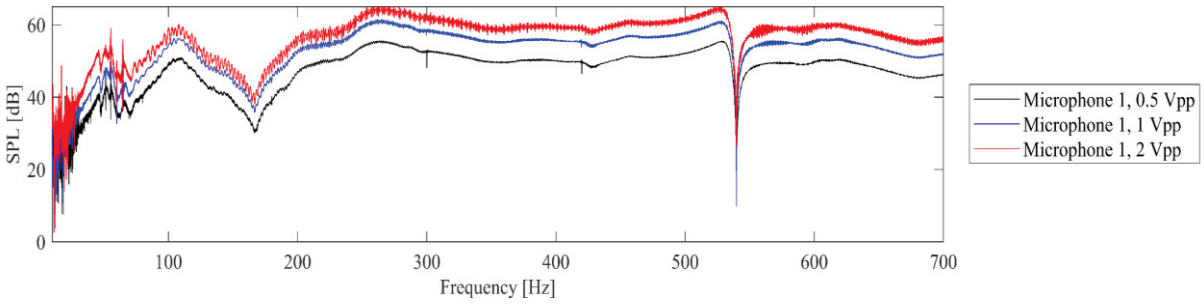

SOURCE: The author (2023).

The resulting strain in the plate is considerably smaller in comparison to the previous experiment regarding the modal experiments with the free-free aluminum beam. Thus, a new method of obtaining the SFRF from the results was required considering the noisier signal. The new method obtains the curve with highest SNR by comparing the anti-peak frequency response value for each curve related to a serpentine arrangement. In theory, the higher background noise would lead to a high value of anti-peak response at the given frequency. FIGURE 77 demonstrates the DAS signal obtained for a single chirp experiment. The 4 sections related to each serpentine arrangement are separated by black dashed lines. The presence of noise is demonstrated by red circles and red dashed lines. In this experiment, regions of random noise are found as a result of fluctuations in the response of the fiber and demodulation procedure, which become more significant in cases where the strain signals are lower. The L_r parameter is calculated for this serpentine arrangement and the converted strain signal is found. In FIGURE 78, the spatial signals obtained using DAS for each serpentine arrangement are plotted for 100 different temporal samples through the experiment. The curves demonstrate that the range of strain measured by DAS for the experiment is approximately 0.01 με or lower.

FIGURE 77 – DAS SIGNAL FOR ACOUSTIC EXPERIMENTS WITH FREE-FREE PLATE

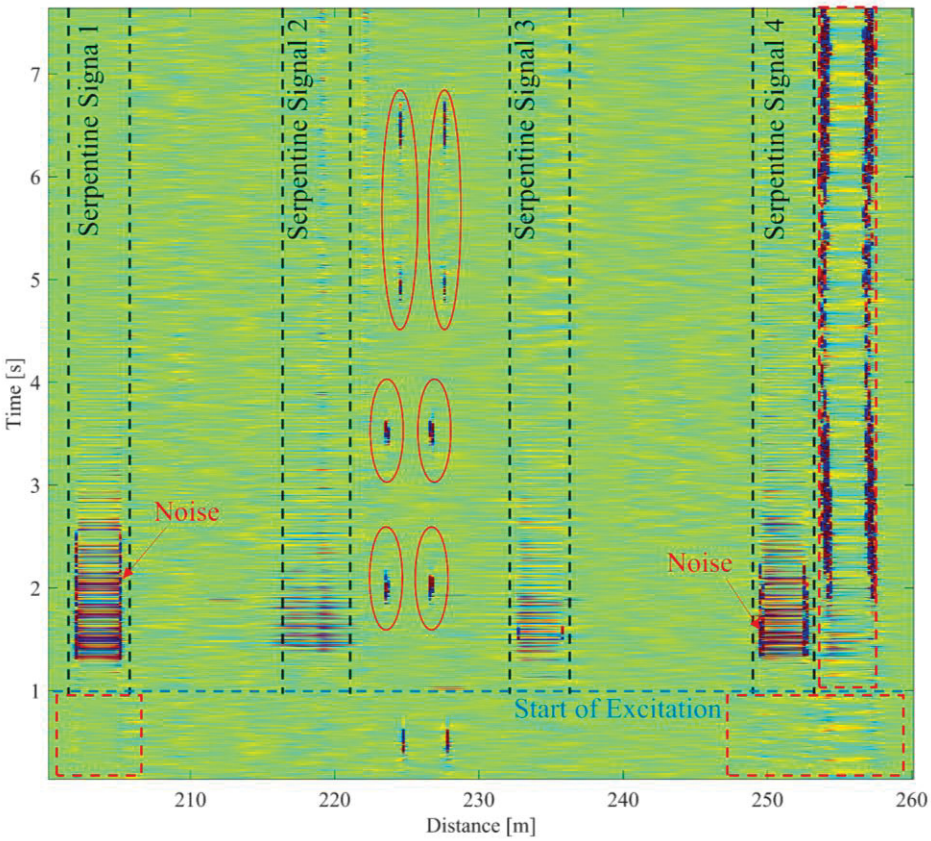

SOURCE: The author (2023).

FIGURE 78 – DAS STRAIN SIGNALS FOR EACH SERPENTINE ARRANGEMENT AT DIFFERENT POINTS IN TIME

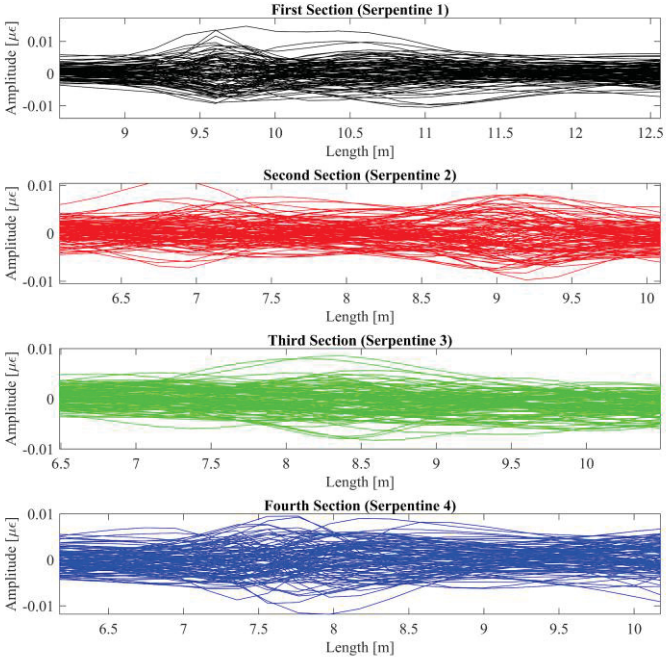

SOURCE: The author (2023).

The selected curves for each experiment and arrangement are stored and the average PSD curve can be calculated. FIGURE 79, FIGURE 80 and FIGURE 81 demonstrate the curves obtained for the 0.5 Vpp, 1 Vpp and 2 Vpp experiments, respectively, comparing the measurements obtained with the oblique angled acoustic incidence (45º) and the normal incidence (90º) of the acoustic wave. In FIGURE 79, the experiment with 90º degrees incident wave obtained curves with approximately 10 dB higher values of strain when compared to the 45º angle of incidence. This occurred as a result of the smaller projected of the oblique incident plate (45º) area receiving the acoustic waves compared to the normal incident wave.

FIGURE 79 – 0.5 VPP ACOUSTIC SIGNAL RESPONSE FOR EACH SECTION OF THE PLATE EXPERIMENT

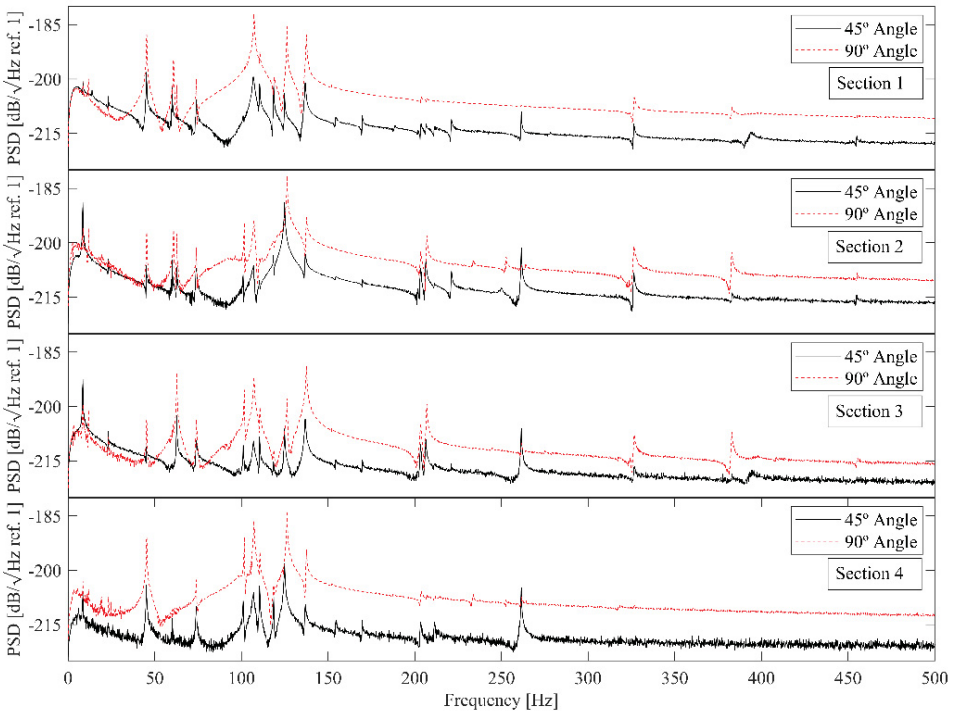

SOURCE: The author (2023).

FIGURE 80 – 1 VPP ACOUSTIC SIGNAL RESPONSE FOR EACH SECTION OF THE PLATE EXPERIMENT

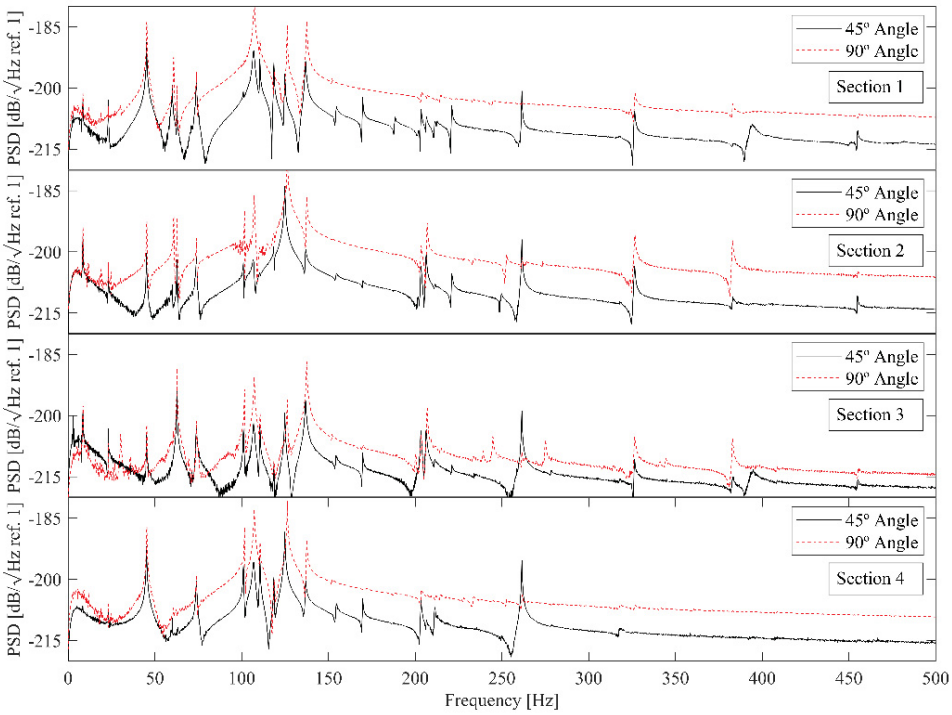

SOURCE: The author (2023).

FIGURE 81 – 2 VPP ACOUSTIC SIGNAL RESPONSE FOR EACH SECTION OF THE PLATE EXPERIMENT

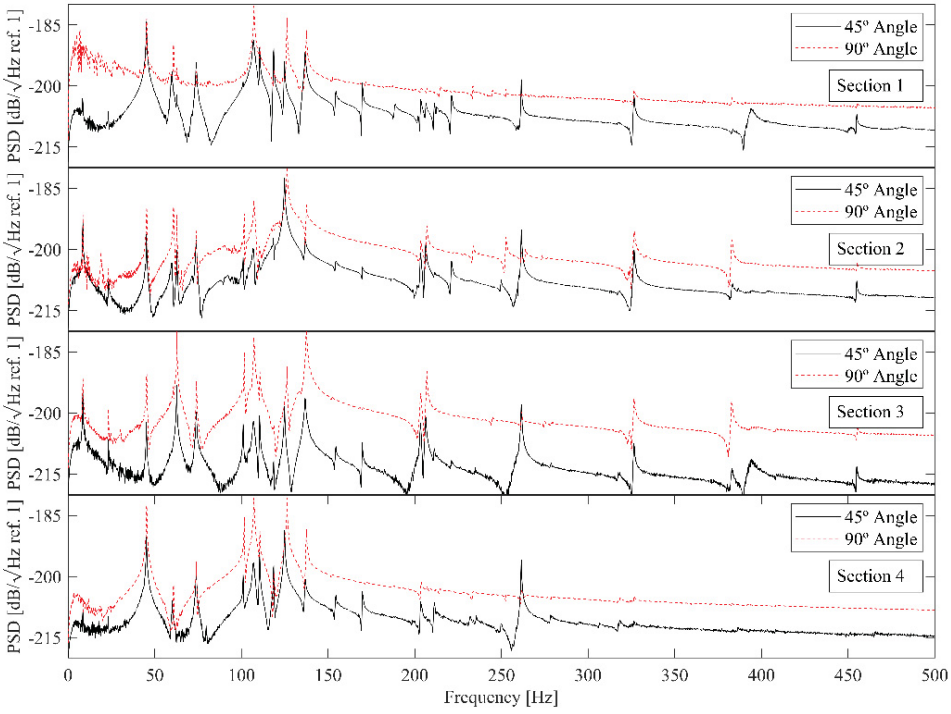

SOURCE: The author (2023).

The results demonstrate that the optical fiber system is able to measure the strain response of the instrumented plate with an average 54 dB chirp sound source up to 500 Hz. As consequence of the plate rigidity, size and the acoustic power transmitted into the plate, the measured strain is in order of 0.01 με. An updated FEM model was used to determine the modes of vibration of the plate and suggest the corresponding peak in the response obtained by DAS. Considering section 2 of the plate for a given 45º excitation, the modes and corresponding response peaks are shown in FIGURE 82. As demonstrated in the figure, the plate is highly sensitive to flexural modes and modes which deform the middle section of the plate longitudinally. However, higher frequency modes demonstrate decreasing sensibility to the optical fiber arrangement measurements as consequence of regions of compressive and tensile strain within the sensing resolution. Some modes of vibration, as shown in blue circles in FIGURE 82, also deforms the optical fiber in similar manner to high frequency modes leading to low resultant average strain over the sensed region.

FIGURE 82 – MODE DECOMPOSITION OF FREQUENCY RESPONSE OBTAINED USING DAS FOR PLATE EXPERIMENT

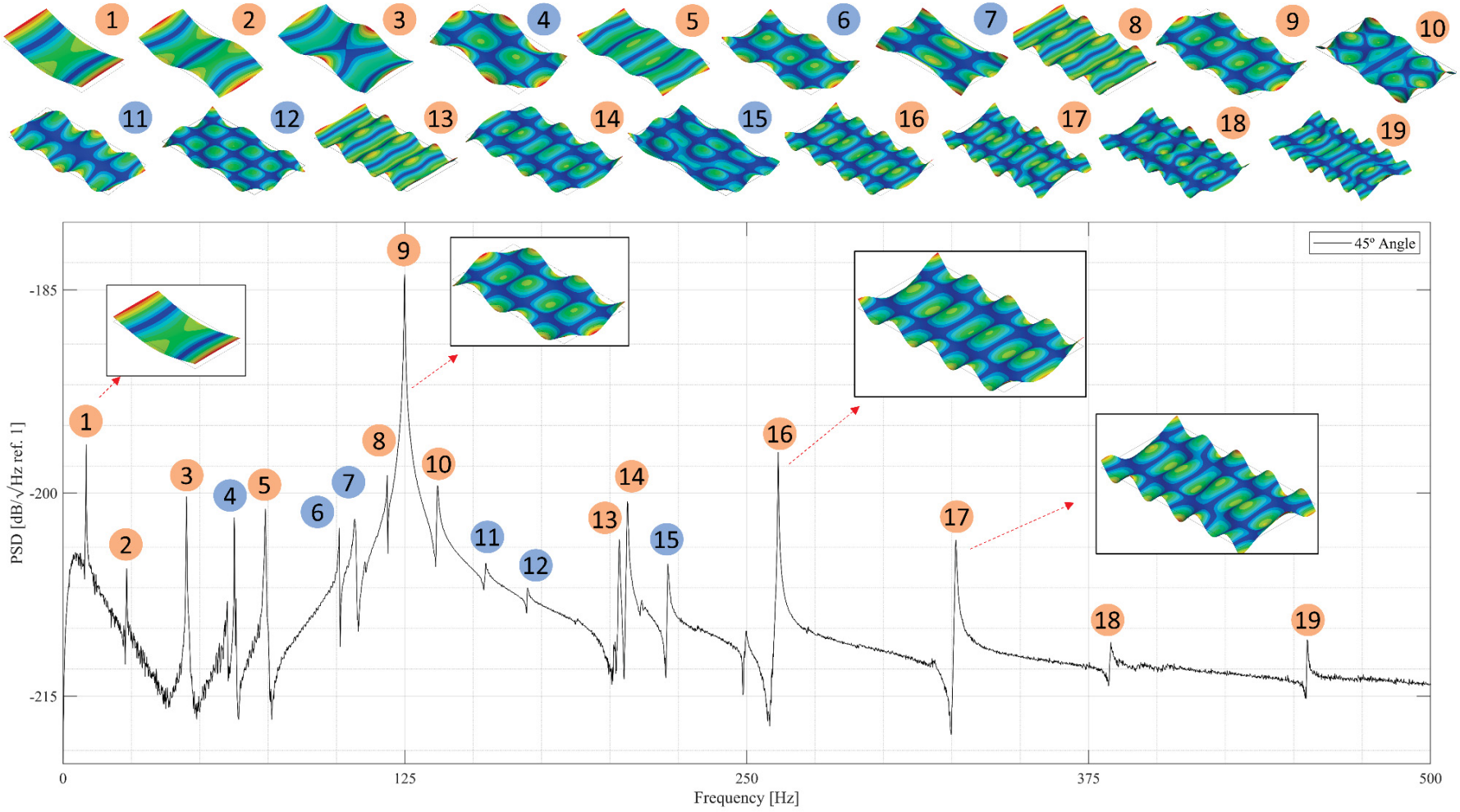

SOURCE: The author (2023).

6 CONCLUSIONS

The application of optical fibers as sensors of mechanically and acoustic induced vibration in structures was investigated in this thesis. A new method of monitoring local dynamic strain of structures using DAS is proposed using a novel optical fiber arrangement. The method uses a serpentine configuration to measure strain locally at discrete regions of the structure and with higher sensibility enabling DAS to determine, among other vibration information, the strain frequency response function (SFRF) of the structure and vibration modes. An elastic-optical mathematical model is developed to convert the phase signals into strain considering each tested arrangement. Validating experiments using impact hammer, shaker and acoustic sources are used to test the arrangements. Differently to other applications of distributed optical fiber sensors in the literature, this is the first detailed study of the DAS sensor topology being deployed in a small structure and conclude that the sensor has the potential to measure vibration data effectively if the correct arrangement is used (CHENG et al., 2017; CIMINELLO, 2019; FANG; SU; ANSARI, 2021; PELLONE et al., 2020).

In the vibration experiments using direct vibration, where a modal hammer or shaker is used to directly vibrate the structure, the experimental results show that the use of optical fiber in a serpentine arrangement grants superior results in measuring the vibration response of the beam when compared to the optical fiber in a straight line along the beam as consequence of the in-phase measurement of deformation in the optical fiber. This occurs due to the ratio between effective spatial resolution and size of the length of the structure in which the optical fiber is installed. Furthermore, the construction arrangement does not incur in optical signal losses as result of the curvature radius of the serpentine, as every section of the fiber demonstrated accurate results independently of the position along the optical fiber length. In the 2.7 aluminum beam experiment, three different serpentine arrangement of optical fibers are investigated in measuring the strain vibration response locally of a small beam structure using DAS. The PNR increased by twofold (and up to 12.9 dB increase for low excitation forces) using the 9 passes serpentine arrangement, for example, while being able to identify most resonant frequencies. Additionally, the optimal number of serpentine coils was analyzed with the comparison between 1, 3 and 9 passes of serpentine coiled fiber. In the case of 9 passes, a considerably low impact force allows the measurement of well-defined responses and mode shapes. In general, the use of segmented optical fiber arrangements separated by isolated buffers as studied in this work allows the DAS system to accurately identify vibration information of

structures, frequency responses and mode shapes. In the case of fiber coils with a high number of passes, the increased sensibility can be used to determine vibration signals even with considerably low excitation. Also, the method of converting the measured phase signal into strain was able to obtain similar curves for every arrangement tested, with an average SFRF curve at similar levels. However, comparing the SFRF curves with 1, 3 and 9 passes of fiber, a significant difference is found in the PNR level. This result validates that the method proposed obtains accurate strain measurements. The methodology presented in this experiment, using the serpentine arrangements, enables the application of DAS sensors in significantly smaller structures compared to the ones presented previously in the literature, allowing the identification of the local vibration response with increased spatial resolution for certain industrial applications reliant on accurate FRF reconstruction such as SHM of equipment, vibro-acoustic monitoring of structures, acoustic measurements, flow identification, and other applications where high sensibility is required. The developed Photo-elastic conversion algorithm and model updating algorithm were used in these experiments to calibrate the PSD curves obtained and enabled the comparison between FEM result and experimental result. This methodology can introduce new ways to calibrate and compare DAS topologies considering that the standardization of the sensor and experiments, as mentioned in the literature review, are still being developed. Also, the method can be used to develop cabling design or fiber optic devices for DAS that are able to monitor assets with increased resolution enabling new applications in the field.

In the plate experiment with acoustic source, the results demonstrate that the DAS system is able to measure with high sensitivity the acoustic transmission of sound waves into flexible structures. As mentioned in the Background section, studies have been developed to determine the acoustic sensitivity and directivity of optical fiber cables with enhanced response to mechanical waves. The plate experiment shows that the response of the optical fiber and the DAS measured phase signals are dictated by the mechanical behavior of the structure in which the fiber is coupled. In other words, the acoustic waves exciting the optical fiber can be modelled by nodal forces in the structure which, in turn, deforms the optical fibers. The experiment demonstrates that the serpentine arrangement using 15 coiled fibers achieve a sensibility of up to 0.01με using conventional fibers. As mentioned in the literature review, methods of increasing the sensibility of optical fibers and cables used for DAS are currently being explored. In this scenario, the proposed serpentine arrangements are able to significantly improve the signal gain and spatial resolution of the sensor without requiring complex optoelectronic topologies or special optical fibers. The use of redundant optical fiber to acquire

signals is a cost-effective alternative to improve the measurement parameters of DAS since the cost of optical fibers is considerably lower than the optical components required to improve SNR. Furthermore, the analyzed acoustic experiments suggests that by determining the structural response of a device, the angle of the incoming oblique incident acoustic wave can be inferred using the system. This can be the basis for future studies of acoustic devices to be employed using DAS.

6.1 FUTURE WORKS

For future work, the following studies are proposed:

- Utilize the optical fiber strain model in an optimization algorithm to determine improved arrangements for certain vibration modes;
- Use the proposed methodology to identify cracks and defects based on the SFRF response and modal parameters;
- The extension of the model to account for the interaction of propagating light wave and strain, dividing the Pockel equation into two separate effects, one related to the positioning of the backscatterers and the other related to the change of refractive index;
- The application of the proposed model and arrangement in optical fibers protected by surrounding layers of material, using the *Lr* parameter to calculate the transmitted strain into the optical fiber as friction.

REFERENCES

ANTUNES, P. et al. Mechanical Properties of Optical Fibers. **Selected Topics on Optical Fiber Technology**, 2012.

ALQAM, Hana'a M.; DHINGRA, Anoop K. Frequency Response-Based Indirect Load Identification Using Optimum Placement of Strain Gages and Accelerometers. **Journal of Vibration and Acoustics, Transactions of the ASME**, *[S. l.]*, v. 141, n. 3, 2019. DOI: 10.1115/1.4042709.

BAKER, A. et al. Permanent monitoring – looking at lifetime reservoir dynamics. **NIGAGE**, 1995.

BAKER, A. et al. Permanent monitoring. Looking at lifetime reservoir dynamics. **Oilfield Review**, v. 7, n. 4, p. 32-46, 1995.

BAKAIC, M.; HANNA, M.; HNATOVSKY, C.; et al. Fiber-optic Bragg gratings for temperature and pressure measurements in isotope production targets for nuclear medicine. **Applied Sciences (Switzerland)**, v. 10, n. 13, 2020.

BAKKU, S. K. **Fracture Characterization from Seismic Measurements in a Borehole.** PhD Thesis, 2015. Massachusetts Institute of Technology.

BAO, X.; WEBB, D. J.; JACKSON, D. A. Distributed temperature sensor based on Brillouin loss in an optical fibre for transient threshold monitoring. **Canadian Journal of Physics**, v. 74, n. 1–2, p. 1–3, 1996.

BARRIAS, A.; CASAS, J. R.; VILLALBA, S. A review of distributed optical fiber sensors for civil engineering applications. **Sensors (Switzerland)**, v. 16, n. 5, 2016.

BSI. **BS ISO 26101 : 2017 BSI Standards Publication Acoustics — Test methods for the qualification of free-field environments**. 2017.

CHEN, D.; LIU, Q.; HE, Z. High-fidelity distributed fiber-optic acoustic sensor with fading noise suppressed and sub-meter spatial resolution. **Optics Express**, v. 26, n. 13, p. 16138–16146, 2018. OSA. Disponível em: <http://www.opticsexpress.org/abstract.cfm?URI=oe-26-13-16138>. .

CHEN, D.; LIU, Q.; HE, Z. 108-km Distributed Acoustic Sensor With 220-pHz Strain Resolution and 5-m Spatial Resolution. **Journal of Lightwave Technology**, v. 37, n. 18, p. 4462–4468, 2019.

CHEN, J.; NING, J.; CHEN, W.; et al. Distributed acoustic sensing coupling noise removal based on sparse optimization. **Interpretation**, v. 7, n. 2, p. T373–T382, 2019.

CHEN, M.; MASOUDI, A.; BRAMBILLA, G. Performance analysis of distributed optical fiber acoustic sensors based on φ-OTDR. **Optics Express**, v. 27, n. 7, p. 9684, 2019.

CHENG, L.; BUSCA, G.; ROBERTO, P.; VANALI, M.; CIGADA, A. Damage detection based on strain transmissibility for beam structure by using distributed fiber optics. **Conference**

Proceedings of the Society for Experimental Mechanics Series, v. 7, p. 27–40, 2017.

CIMINELLO, M. Distributed Fiber Optic for Structural Health Monitoring System Based on Auto-Correlation of the First-Order Derivative of Strain. **IEEE Sensors Journal**, v. 19, n. 14, p. 5818–5824, 2019.

CORERA, I.; PIÑEIRO, E.; NAVALLAS, J.; SAGUES, M.; LOAYSSA, A. Long-Range Traffic Monitoring Based on Pulse-Compression Distributed Acoustic Sensing and Advanced Vehicle Tracking and Classification Algorithm. **Sensors**, v. 23, n. 6, p. 3127, 2023.

COSTA FRAGA, C. T.; LARA, A. Q.; CAPELEIRO PINTO, A. C.; MOREIRA BRANCO, C. C. Challenges and Solutions To Develop Brazilian Pre-Salt Deepwater Fields . , 15. jun. 2014.

DEAN, T.; CUNY, T.; HARTOG, A. H. The effect of gauge length on axially incident P-waves measured using fibre optic distributed vibration sensing. **Geophysical Prospecting**, v. 65, n. 1, p. 184–193, 2017.

Document No : SEAFOM Measuring Sensor Performance Document – 02 (SEAFOM MSP-02) DAS Parameter Definitions and Tests Issue Date : August 2018. ., v. 02, n. August, p. 1–52, 2018.

FAHY, F.; WALKER, J. **Advanced Applications in Acoustics, Noise and Vibration**. CRC Press, 2018.

FANG, Z.; SU, H.; ANSARI, F. Modal analysis of structures based on distributed measurement of dynamic strains with optical fibers. **Mechanical Systems and Signal Processing**, v. 159, p. 107835, 2021. Elsevier Ltd. Disponível em: <https://doi.org/10.1016/j.ymssp.2021.107835>. .

FENG, S.; XU, T.; HUANG, J.; et al. Sub-Meter Spatial Resolution Phase-Sensitive Optical Time-Domain Reflectometry System Using Double Interferometers. **Applied Sciences** , 2018.

HARTOG, A. H. **An introduction to distributed optical fibre sensors**. CRC Press, 2017.

HE, H.; YAN, L.; QIAN, H.; et al. Enhanced range of the dynamic strain measurement in phase-sensitive OTDR with tunable sensitivity. **Optics Express**, v. 28, n. 1, p. 226, 2020.

HE, X.; ZHANG, M.; GU, L.; et al. Performance improvement of dual-pulse heterodyne distributed acoustic sensor for sound detection. **Sensors (Switzerland)**, v. 20, n. 4, p. 1–13, 2020.

HE, X.; ZHANG, M.; XIE, S.; et al. Identification and observation of the phase fading effect in phase-sensitive OTDR. **OSA Continuum**, v. 1, n. 3, p. 963, 2018.

HE, Z.; LIU, Q. Optical Fiber Distributed Acoustic Sensors: A Review. **Journal of Lightwave Technology**, v. 39, n. 12, p. 3671–3686, 2021.

HERNÁNDEZ-SERRANO, A. I.; SALCEDA-DELGADO, G.; MORENO-HERNÁNDEZ, D.; MARTÍNEZ-RÍOS, A.; MONZÓN-HERNÁNDEZ, D. Robust optical fiber bending sensor to measure frequency of vibration. **Optics and Lasers in Engineering**, v. 51, n. 9, p. 1102–

1105, 2013.

HSU, W. K.; LEE, Y. L.; KUAN, T. T. Brillouin frequency shift sensing technology used in railway strain and temperature measurement. **Applied Sciences (Switzerland)**, v. 11, n. 15, 2021.

IPPEN, E. P.; STOLEN, R. H. Stimulated Brillouin scattering in optical fibers. **Applied Physics Letters**, v. 21, n. 11, p. 539–541, 1972.

JUAREZ, J. C.; MAIER, E. W.; CHOI, K. N.; TAYLOR, H. F. Distributed fiber-optic intrusion sensor system. **Journal of Lightwave Technology**, v. 23, n. 6, p. 2081–2087, 2005.

KINSLER, L. E.; FREY, A. R.; COPPENS, H. B.; SANDERS, J. V.; SAUNDERS, H. Fundamentals of Acoustics (3rd Ed.). **Journal of Vibration and Acoustics**, v. 105, n. 3, p. 269–270, 1983. Disponível em: <http://aapt.scitation.org/doi/10.1119/1.1932798>. .

KOYAMADA, Y.; EDA, Y.; HIROSE, S.; NAKAMUKA, S.; HOGARI, K. Novel fiber-optic distributed strain and temperature sensor with very high resolution. **IEICE Transactions on Communications**, v. E89-B, n. 5, p. 1722–1725, 2006.

LAI, W. M.; RUBIN, D.; KREMPL, E. **Introduction to Continuum Mechanics**. Elsevier, 2010.

LI, J.; ZHANG, M. Physics and applications of Raman distributed optical fiber sensing. **Light: Science and Applications**, v. 11, n. 1, 2022. Springer US.

LIEHR, S.; MÜNZENBERGER, S.; KREBBER, K. Wavelength-Scanning Distributed Acoustic Sensing for Structural Monitoring and Seismic Applications. **Proceedings**, v. 15, n. 1, p. 30, 2019.

LIM CHEN NING, I.; SAVA, P. High-resolution multi-component distributed acoustic sensing. **Geophysical Prospecting**, v. 66, n. 6, p. 1111–1122, 2018.

LIU, H.; PANG, F.; LV, L.; et al. True Phase Measurement of Distributed Vibration Sensors Based on Heterodyne φ-OTDR. **IEEE Photonics Journal**, v. 10, n. 1, p. 1–9, 2018. IEEE.

LU, B.; PAN, Z.; WANG, Z.; et al. High spatial resolution phase-sensitive optical time domain reflectometer with a frequency-swept pulse. **Optics Letters**, v. 42, n. 3, p. 391–394, 2017. OSA. Disponível em: <http://ol.osa.org/abstract.cfm?URI=ol-42-3-391>. .

MARTINS, H. F.; SHI, K.; THOMSEN, B. C.; et al. Real time dynamic strain monitoring of optical links using the backreflection of live PSK data. **Optics Express**, v. 24, n. 19, p. 22303–22318, 2016. OSA. Disponível em: <http://www.opticsexpress.org/abstract.cfm?URI=oe-24-19-22303>. .

MASOUDI, A.; NEWSON, T. P. Analysis of distributed optical fibre acoustic sensors through numerical modelling. **Optics Express**, v. 25, n. 25, p. 32021, 2017.

MILLER, D. A. B. Huygens's wave propagation principle corrected. **Optics Letters**, v. 16, n. 18, p. 1370, 1991.

MUGGLETON, J. M.; HUNT, R.; RUSTIGHI, E.; LEES, G.; PEARCE, A. Gas pipeline leak noise measurements using optical fibre distributed acoustic sensing. **Journal of Natural Gas Science and Engineering**, v. 78, n. January, p. 103293, 2020. Elsevier B.V. Disponível em: <https://doi.org/10.1016/j.jngse.2020.103293>. .

NARASIMHAMURTY, T. S. **Photoelastic and Electro-Optic Properties of Crystals**. Boston, MA: Springer US, 1981.

OKAMOTO, K. **Fundamentals of Optical Waveguides**. 2006.

OLIVEIRA, R. A.; NEVES, P. T.; PEREIRA, J. T.; CANNING, J.; POHL, A. A. P. Vibration mode analysis of a silica horn-fiber Bragg grating device. **Optics Communications**, v. 283, n. 7, p. 1296–1302, 2010. Elsevier B.V. Disponível em: <http://dx.doi.org/10.1016/j.optcom.2009.11.035>. .

ONO, M.; AOYAMA, S.; FUJINAMI, M.; ITO, S. Significant suppression of Rayleigh scattering loss in silica glass formed by the compression of its melted phase. **Optics Express**, v. 26, n. 7, p. 7942, 2018.

PAN, Z.; LIANG, K.; YE, Q.; et al. Phase-sensitive OTDR system based on digital coherent detection. **Asia Communications and Photonics Conference and Exhibition, ACP 2011**, v. 8311, p. 1–6, 2011.

PELLONE, L.; CIMINELLO, M.; GALASSO, B.; et al. Detecting of bonding defects using an SHM fiber-optics distributed sensors system in typical wing spar coupon. **AIP Conference Proceedings**, v. 2309, n. 1, p. 20028, 2020. American Institute of Physics. Disponível em: <https://aip.scitation.org/doi/abs/10.1063/5.0035009>. .

POCKELS, F. Ueber die durch einseitigen Druck hervorgerufene Doppelbrechung regulärer Krystalle, speciell von Steinsalz und Sylvin. **Annalen der Physik und Chemie**, v. 275, n. 3, p. 440–469, 1890. Disponível em: <https://onlinelibrary.wiley.com/doi/10.1002/andp.18902750313>. .

POHL, A. A. P.; OLIVEIRA, R. A.; DA SILVA, R. E.; et al. Advances and new applications using the acousto-optic effect in optical fibers. **Photonic Sensors**, v. 3, n. 1, p. 1–25, 2013.

RAO, S. S. Mechanical Vibrations Sixth Edition in SI Units Access for. **Pearson**, v. 6, p. 1291, 2017.

REN, M.; ZHOU, D.-P.; CHEN, L.; BAO, X. Influence of finite extinction ratio on performance of phase-sensitive optical time-domain reflectometry. **Optics Express**, v. 24, n. 12, p. 13325, 2016.

RUSSO, M.; KRALJEVIĆ, L.; STELLA, M.; SIKORA, M. Acoustic performance analysis of anechoic chambers based on ISO 3745 and ISO 26101: standards comparison and performance analysis of the anechoic chamber at the University of Split. **Proceedings of Euronoise 2018**, p. 2225–2230, 2018.

SALEH, B. E. A.; CARL, M. **Fundamentals of Photonics**. Wiley Seri ed. Wiley Interscience,

2007.

SEAFOM. Measuring Sensor Performance Document – 02 (SEAFOM MSP-02) DAS Parameter Definitions and Tests. , 2018.

SHANG, Y.; SUN, M.; WANG, C.; et al. Research Progress in Distributed Acoustic Sensing Techniques. **Sensors**, v. 22, n. 16, 2022.

SILVA, R. E.; FRANCO, M. A. R.; NEVES, P. T.; BARTELT, H.; POHL, A. A. P. Numerical and experimental analysis of the modulation of fiber Bragg gratings by low-frequency complex acoustic waves. **Optical Fiber Technology**, v. 30, p. 17–22, 2016. Elsevier Inc. Disponível em: <http://dx.doi.org/10.1016/j.yofte.2016.01.011>. .

SIMMONS, J.; POTTER, K. **Optical Materials**. San Diego: Academic Press, 1999.

SMITH, F. G. **Optics and Photonics : An Introduction Second Edition**. 2007.

SUSHIL, S. K.; GARG, M.; NARAYANAN, S. Estimation of the lower cut-off frequency of an anechoic chamber: An empirical approach. **International Journal of Aeroacoustics**, v. 19, n. 1–2, p. 57–72, 2020.

TAYLOR, H. F.; LEE, C. E. Apparatus and Method for Fiber Optic Intrusion Sensing. , 1993. United States.

TREYSSÈDE, F. Vibration analysis of horizontal self-weighted beams and cables with bending stiffness subjected to thermal loads. **Journal of Sound and Vibration**, v. 329, n. 9, p. 1536–1552, 2010.

TSUJIKAWA, K.; TAJIMA, K.; ZHOU, J. Intrinsic loss of optical fibers. **Optical Fiber Technology**, v. 11, n. 4, p. 319–331, 2005. Disponível em: <https://www.sciencedirect.com/science/article/pii/S1068520005000210>. .

VILLAR, I.; MATIAS, I. R. **Optical Fibre Sensors**. Wiley, 2020.

WANG, Z.; LU, B.; YE, Q.; CAI, H. Recent progress in distributed fiber acoustic sensing with Φ-otdr. **Sensors (Switzerland)**, v. 20, n. 22, p. 1–26, 2020a.

WANG, Z.; LU, B.; YE, Q.; CAI, H. Recent Progress in Distributed Fiber Acoustic Sensing with Φ-OTDR. **Sensors** , 2020b.

WANG, Z. N.; ZENG, J. J.; LI, J.; et al. Ultra-long phase-sensitive OTDR with hybrid distributed amplification. **Optics Letters**, v. 39, n. 20, p. 5866–5869, 2014. OSA. Disponível em: <http://ol.osa.org/abstract.cfm?URI=ol-39-20-5866>. .

WESTBROOK, P. S.; FEDER, K. S.; KREMP, T.; et al. Enhanced Optical Fiber for Distributed Acoustic Sensing beyond the Limits of Rayleigh Backscattering. **iScience**, v. 23, n. 6, p. 101137, 2020. Elsevier Inc. Disponível em: <https://doi.org/10.1016/j.isci.2020.101137>. .

WIESMEYR, C.; LITZENBERGER, M.; WASER, M.; et al. Real-time train tracking from distributed acoustic sensing data. **Applied Sciences (Switzerland)**, v. 10, n. 2, 2020.

YAM, L. H.; LEUNG, T. P.; LI, D. B.; XUE, K. Z. Theoretical and experimental study of modal strain analysis. **Journal of Sound and Vibration**, v. 191, n. 2, p. 251–260, 1996.

ZHANG, Y.; XU, H.; ZHU, X.; ZHAO, Z.; ZUO, J. Detection and Quantization Technique of Optical Distributed Acoustic Coupling Based on φ-OTDR. **Journal of Shanghai Jiaotong University (Science)**, v. 25, n. 2, p. 208–213, 2020.

7 APPENDIX A – BENDING AND RADIAL PRESSURE EFFECTS ON OPTICAL FIBERS

In the current literature, most articles studying DAS performance and its applications use the simplified equation described above to model any mechanical vibration in the optical fiber. Nevertheless, mechanical stress and strain in the optical fiber medium can be a result of a multitude of dynamic combined loads leading to a complex strain state. According to Fang et. al (2012), single-mode optical fibers are sensitive to axial strain, to lateral pressure and bending. The photo-elastic effects in the presence of radial stress or bending are described next. As the length of the fiber is considerably greater than its transverse size, a plane strain state is assumed. FIGURE 25 shows the optical fiber hydrostatic strain problem.

FIGURE 83 – HYDROSTATIC AND TRANSVER PRESSURE IN OPTICAL FIBER

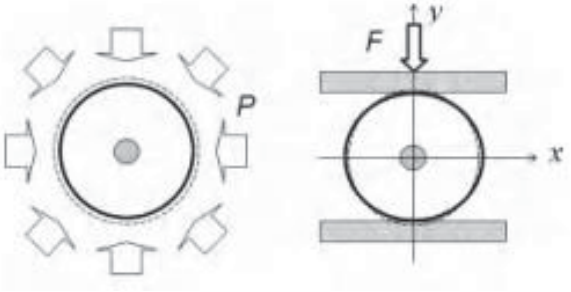

SOURCE: Fang et. al (2012)

The strain state due to a radial pressure, P_r, around the optical fiber is described as

$$\varepsilon_x = \varepsilon_x = \varepsilon_r = (1+\upsilon)(1-2\upsilon)\frac{P_r}{E} \tag{65}$$

E is the young's modulus of the material. Thus, the change in the refractive index of optical fiber due to radial pressure can be expressed as

$$\Delta n = \frac{-n_0^3 P_r}{2E}\left[(1+\upsilon)(1-2\upsilon)(p_{11}+p_{12})\right] \tag{66}$$

rearranging Eq. 14 and Eq. 17, the phase difference due to the radial stress is found to be

$$\Delta\phi = \frac{-n_0^3 P_r}{2E}\left[(1+\upsilon)(1-2\upsilon)(p_{11}+p_{12})\right]kL \tag{67}$$

the strain distribution in the case of bending in the optical fiber is shown in FIGURE 25. For a bending radius, R, the stress induced birefringence is obtained through the derivation of Hooke's law and is given by

$$B = \Delta n_y - \Delta n_x = \frac{-n^3}{16}(p_{11}+p_{12})(1+\upsilon)\left[\frac{d^2}{R^2} - \frac{\bar{e}_z d(7-6\upsilon)}{2(1-\upsilon)R}\right] \tag{68}$$

where $\bar{e}_z$ denotes the strain caused by the elongation in the longitudinal direction of the optical fiber and d is the diameter of the fiber

FIGURE 84 – A) BENT AND STRETCHED FIBER; B) FIBER'S STRAIN DISTRIBUTION.

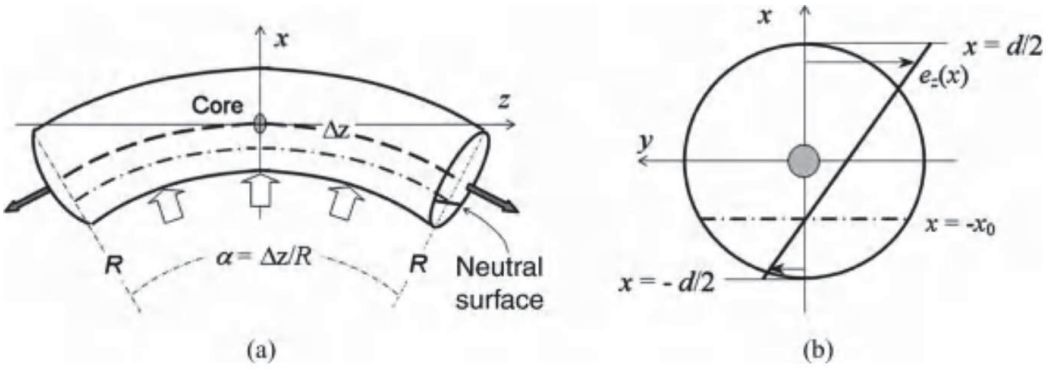

SOURCE: Fang et. al (2012)

The birefringence effect of bending does not affect the phase of the backscattered light pulse directly. When the bending curvature, $1/R$, is considerably high, it is known, empirically, that the signal of DAS is greatly affected.